journal of the international meteor organization

WGN

49:6
december 2021

IMC 2021 special issue:

Contributions cover:

Studies of the meteor phenomenon using visual, video, radio, spectroscopic, and fireball observations
Identifying and observing meteor showers
Detecting and tracking meteors from space
Collecting micrometeorites in the stratosphere
Status of the IAU Meteor Data Center
Re-entry of Hayabusa-2 observed from Australia

ISSN 1016-3115

WGN Vol. 49, No. 6, December 2021, pp. 145 – 216

Administrative

Conferences

Front cover photo

Bright fireball on 2021 November 28, at $18^{h}41^{m}19^{s}$ UT from Setagaya-ku Tokyo Japan, Tokyo8_U6 camera of Sonotaco Network (Sony ILCE-6300 with Sigma 16 mm F1.4 3840 × 2160/59.94i HDMI).
`http://sonotaco.jp/forum/viewtopic.php?t=5075`
Image courtesy: SonotaCo.

Writing for WGN

This Journal welcomes papers submitted for publication. All papers are reviewed for scientific content, and edited for English and style. Instructions for authors can be found in WGN **45:1**, 1–5, and at `http://www.imo.net/docs/writingforwgn.pdf` .

Copyright

Legal address

International Meteor Organization, Jozef Mattheessensstraat 60, 2540 Hove, Belgium.

From the Treasurer — IMO Membership/WGN Subscription Renewal for 2022

Marc Gyssens

Renewal rates

Most members/subscribers whose membership/subscription has expired should have received a reminder email by the time you receive this issue of WGN. Via this way, we invite them again to renew for 2022.

The fees are as tabulated below. We are happy that we can offer WGN at the same cost as last year. We also continue to offer an electronic-only subscription at a reduced rate.

IMO Membership/WGN Subscription 2022				
Electronic + paper with surface mail delivery:		€26		US$ 32
Electronic + paper with airmail delivery (outside Europe only):		€49		US$ 60
Electronic only:		€21		US$ 25
Supporting membership:	add	€26	add	US$ 32

It is also possible to renew for two or more years in a row.

When you renew, give a few minutes of thought to becoming a **supporting member** by paying at least 26 EUR/32 USD extra. Smaller gifts are of course also appreciated. As you may know, there is an IMO Support Fund. With this Support Fund, we offer support to meteor-related projects. Our ability to provide this service to the meteor community depends primarily on the gifts we receive from supporting members!

Another way to help meteor workers with limited funds is to offer them a gift subscription.

We already thank all our members that will renew for their continued trust in our Organization!

Payment instructions

You first must log in into your account at the IMO website if you want to renew. For this purpose, click the log-in button in the upper right-hand corner. As login, use the email address on which you received my reminder email. In case you forgot your password, you can use the "forgot password" link to reset it. Once logged in, you will see your profile picture (or the space provided for it). If you read on the green button below it that your membership is about to expire, click it, and the rest will be self-explanatory.[1]

The outcome of this process is that you will see the total amount due and your payment options. If you choose to pay using PayPal (or using a credit card via PayPal), you can complete the payment on our website.

If you experience any difficulties, do not hesitate to contact me at `treasurer@imo.net`.

One final request: every year, a lot of members renew late. As a consequence, back issues that already appeared have to be sent out to these members. Please support our volunteers in their bimonthly effort to have WGN shipped to you by renewing promptly! Thank you for your understanding and cooperation!

[1] Alternatively, you can also click on "Extend your membership" in the pull-down menu to the right of your name in the upper right-hand corner, with the same result.

Observing the Hayabusa-2 Capsule Re-entry over Australia

E. K. Sansom[1], *H. A. R. Devillepoix*[1], *M.-Y. Yamamoto*[2], *M. C. Towner*[1], *S. Abe*[3], *S. Nozawa*[4], *Y. Hiramatsu*[5], *T. Kawamura*[6], *K. Fujita*[7], *M. Yoshikawa*[7], *Y. Ishihara*[7], *N. Segawa*[8], *Y. Kakinami*[9]

A summary of the International Meteor Conference 2021 presentation is presented. A paper recently accepted to PASJ gives a more detailed description, available at `https://arxiv.org/abs/2111.02235`.

Received 2021 October 18

This work has been presented at the International Meteor Conference 2021 (held online).

Japan Aerospace Exploration Agency's Hayabusa-2 sample return capsule (SRC) came back to the Earth on the 5th December 2020 at 17:28 UTC. This was a unique opportunity to test sensors and record aspects of fireball phenomena that are hard to collect for sporadic natural events.

[1]Space Science and Technology Centre, Curtin University, Australia.
[2]School of Systems Engineering, Kochi University of Technology, Japan.
[3]Nihon University, Japan.
[4]Ibaraki University, Japan.
[5]School of Geosciences and Civil Engineering, College of Science and Engineering, Kanazawa University, Japan.
[6]Institut de Physique du Globe de Paris, France.
[7]Institute of Space and Astronautical Science, Japan Aerospace Exploration Agency, Japan.
[8]Faculty of information Science and Engineering, Kyoto Sangyo University, Japan.
[9]Space Information Center, Hokkaido Information University, Japan.

IMO bibcode WGN-496-sansom-hayabusa-2
NASA-ADS bibcode 2021JIMO...49..146S

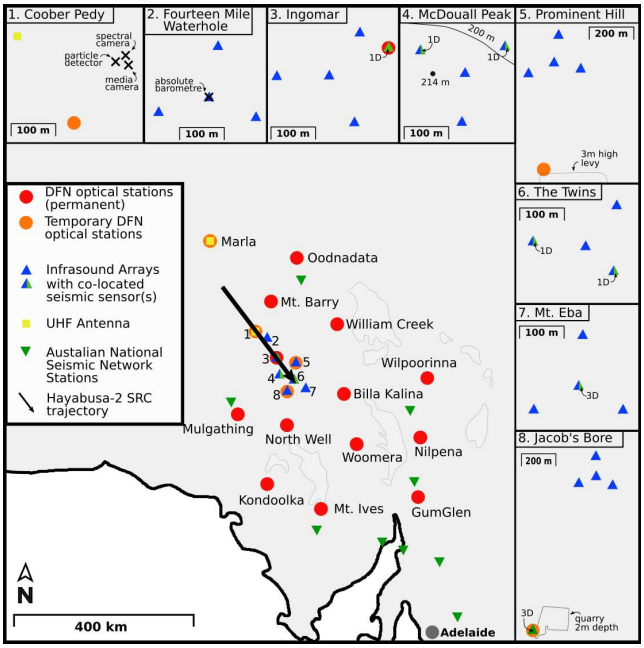

Figure 1 – DFN cameras (red) in relation to the Hayabusa-2 Sample Return Capsule trajectory. Temporary stations containing optical sensors and non-optical instrumentation were deployed as shown close to the predicted capsule trajectory, figure originally from `https://arxiv.org/abs/2111.02235`.

A scientific observations campaign was planned to observe the optical, seismo-acoustic, radio, and high energy particle phenomena associated with its re-entry. A multi-institutional collaboration between Australian and Japanese universities resulted in 49 instruments deployed (total of 73 including existing, permanent sensors). The SRC re-entered the atmosphere over South Australia, visible for 53 seconds as a fireball near the Northern Territory border, towards Woomera where it landed in the Woomera military test range. Data collection was successful and will be used to study the effects produced by interplanetary objects impacting the Earth's atmosphere for natural objects.

The capsule arrival provided a unique opportunity to study an artificial fireball, where both the characteristics and the trajectory of the body were well known. This "calibration point" provides unique information to characterise the data normally seen with fireball camera networks. Multiple non-optical sensors were also deployed; seismic, infrasonic, and UHF waves. The campaign was impacted by COVID19 travel restrictions, which meant that the ground activities were in a large part carried out by local volunteers, which we are very grateful for. Results were recovered by almost all the sensors deployed, with a few instrumentation failures. Significant detections were seen in the infrasound, seismic sensors, as well as optical and hyper spectral observations. A paper recently accepted to PASJ (Sansom et al., 2021) gives a more detailed description, available at `https://arxiv.org/abs/2111.02235`.

References

Sansom E. K., Devillepoix H. A. R., Yamamoto M.-Y., Abe S., Nozawa S., Towner M. C., Cupák M., Hiramatsu Y., Kawamura T., Fujita K., Yoshikawa M., Ishihara Y., Hamama I., Segawa N., Kakinami Y., Furumoto M., Katao H., Inoue Y., Cool A., Bonning G., Howie R. M., and Bland P. A. (2021). "The scientific observation campaign of the Hayabusa-2 capsule re-entry". *Publications of the Astronomical Society of Japan*. psab109.

Handling Editor: Javor Kac
This paper has been typeset from a LaTeX file prepared by the authors.

Tests with a basic ablation and dark flight calculator

Felix Bettonvil[1,2,3] *and Dušan Bettonvil*[1]

We report on testing a basic Python-based ablation- and dark flight calculator with a data set of a meteorite dropping fireball. We were able to find a solution that represents the data reasonably well. The calculator, named PyDAF, is available on Github and we believe it is a valuable tool also for educational purposes to learn about the effects of the different physical parameters on the flight of meteoroid through the Earth atmosphere.

Received 2021 Novmeber 13

This work has been presented at the International Meteor Conference 2021 (held online).

1 Introduction

When meteoroids penetrate Earth's atmosphere, they interact with it, decelerate, emit and ablate, and in rare cases a part survives and reaches the ground. The flight can be modelled with the drag equation and differential mass equation which uses physical properties of the meteoroid, its trajectory through the atmosphere, and characteristics of the atmosphere. A basic calculator was written in Python and presented at the International Meteor Conference 2019 (Bettonvil, 2020), now called PyDAF. The main purpose was to get an indication of the likelihood of meteorites in case of bright fireballs and to understand the effect of the various parameters on the result. In this sense the calculator also is a nice tool for educational purposes.

This paper focuses on testing the code, based on a bright fireball with a recovered meteorite, to study how well reality and model match.

[1]Leiden Observatory, Leiden University, Leiden, The Netherlands. Email: bettonvil@strw.leidenuniv.nl
[2]NOVA Optical Infrared Instrumentation Group, Dwingeloo, The Netherlands. Email: bettonvil@astron.nl
[3]KNVWS Meteor Section
[4]KNVWS Meteor Section.
Email: dusan.bettonvil@gmail.com

IMO bibcode WGN-496-bettonvil-calculator
NASA-ADS bibcode 2021JIMO...49..147B

Table 1 – Input parameters for the ablations and dark flight calculator PyDAF, with indication which parameters usually are known by measurement (M) or estimated (E).

Parameter	unit	(E)st/ (M)eas
Initial velocity V_{inf}	[km/s]	M
Begin-, end point λ(t), ϕ(t), h(t)	[deg, deg, km]	M
Ablation coefficient ζ	[s^2/km^2]	E
Heat transfer coefficient Λ	[–]	E
Drag coefficient Γ	[–]	E
Shape factor A	[–]	E
Luminous eff L_e	[–]	E
Entry mass m	[kg]	E
Density ρ	[kg/m^3]	E
Wind velocity, direction, p(h), T(h)	[m/s, deg, Pa, K]	M

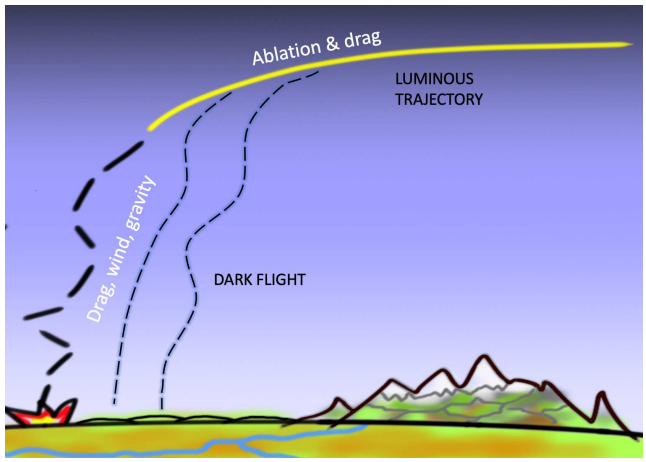

Figure 1 – Trajectory of a bright meteor with its two phases: (a) the luminous trajectory where both ablation and drag influence the meteoroid trajectory; (b) the dark flight were drag, wind and gravity dominate the flight. Also fragmentation may happen which is indicated with additional dashed lines.

2 The simulation software

The code consists of two parts, graphically illustrated in Figure 1: an ablation part and a dark flight part. For the first part the drag equation and differential mass equation are used, based on the great website by spaceacademy.net.au[a] explaining the basics of the atmospheric flight of a meteor. With these equations and several input parameters (see Table 1) the mass loss, deceleration and brightness profile can be computed. This is done in small time steps, which then gives height(t), deceleration(t), mass(t), brightness(t), and geographical location (λ(t), ϕ(t) as output. For small meteoroids the mass reaches zero at a certain altitude, but for larger ones it might happen that the meteoroid has decelerated so much that ablation stops and the meteoroid continues its flight without further mass loss[b]. At this point in time the second part of the code takes over, which is based on the dark flight computation by Ceplecha (1987). It calculates the flight through the atmosphere incorporating drag and gravity acceleration, and outputs the geographical coordinates of the impact

[a]https://www.spaceacademy.net.au/watch/debris/metflite.htm

[b]And thus, the terminal mass is known. Basically, mass loss and mass can be derived from the drag- and differential mass equations which requires knowledge of physical parameters. Terminal mass, can be derived from the deceleration and velocity at the terminal point (Ceplecha, 1987), as well mass and mass loss can derived from the brightness and which requires knowledge of the luminous efficiency (Drolshagen et al., 2021; Gritsevich & Koschny, 2011).

Figure 2 – 24 gram meteorite from the Flensburg meteorite.

point λ(m), ϕ(m) which is a function of mass (this is further explained below and in the next section). The calculation requires knowledge of the atmosphere properties (i.e. density, temperature, wind profile), which usually can be retrieved from weather balloon data (or forecast models)[c]. PyDAF downloads the data automatically from the website of University of Wyoming[d], after specification of the station and time to be used.

PyDAF is able to deal — in a basic form — with fragmentation, contrary to a single ablating body. To utilize this the user specifies in how many fragments the main body splits up and at what height. This feature is useful to analyze what size of meteorite lands where on the ground. Generally, smaller fragments will decelerate faster, land later, but closer to the terminal point of the fireball, and drift more with the wind.

PyDAF is available on Github: `https://github.com/dudaskule/AblationCalculatorPy`.

3 The Flensburg fireball

On September 12, 2019 a very bright daylight fireball appeared over northern Germany, seen by hundreds of witnesses in Germany, The Netherlands and Denmark. The fireball was captured by one Allsky7[e] camera (Herford, Jörg Strunk), several dashcams and US Government sensors (CNEOS[f]). The fireball was extremely bright, but only a single meteorite was recovered (a C1-ungrouped carbonaceous chondrite, 24 gram, density 1984 kg/m^3, Figure 2). The fireball was analysed in detail by Borovička et al. (2021). We decided to use this fireball as a testcase for PyDAF.

From the CNEOS data we know that the total energy was $2 \cdot 10^{12}$ J which can be converted into a mass estimate of 10 600 kg, assuming that all kinetic energy transformed into thermal energy. The measured optical brightness (maximum −21) suggests a slightly larger mass of 22 000 kg (Borovička et al., 2021), both results suggesting a meter-sized object. Due to the large size the deceleration was small, and, unfortunately difficult to measure. The fireball did brighten at altitudes between 45 and 37 km, and it is thought that it heavily fragmented at those altitudes and most of the original mass disappeared.

4 Analysis

In case of a standard, potential meteorite dropping, fireball event (no meteorite recovered yet) PyDAF can be used to obtain understanding if a meteorite recovery is to be expected, and if yes, where. The calculator is used as follows: all not known parameters from Table 1 (those indicated with 'E') are given an initial estimate, and then varied while rerunning the calculator until it gives velocities and decelerations as function of height that fits with the measured velocity profile. Based on these parameters the calculator then gives an estimate for the initial- and terminal mass. The calculation is then repeated again for a to-be-specified number of fragments (each with a mass equal to the initial mass divided by the number of fragments) at a certain altitude. A good choice is the altitude where an (abrupt) increase in brightness appeared. This calculation is then repeated for different number of fragments, which will result in different dark flight paths and landing sites, thus giving the dropping locations on the ground as a function of size. In case photometry is available, also the luminosity can be added to the parameter space and also the brightness fitted, giving a yet more reliable solution. An example of output, as produced by the calculator, is given in Table 2.

For this paper we look at the Borovička et al. (2021) Flensburg set of parameters — both measured, estimated and calculated — to test our simulator and find out how well we can match the trajectory and how well we can point to the dropping area of the recovered

Table 2 – Example of typical output of the simulator. The first part gives as function of time the luminous trajectory, the second part the dark flight. $\mathrm{Vel_L}$, $\mathrm{vel_h}$ and $\mathrm{vel_x}$ give the velocities along the horizontal trajectory, vertical direction and horizontal velocity perpendicular to the flight direction (following the convention in Ceplecha, 1987).

LUMINOUS TRAJECTORY

TIME (S)	HEIGHT (KM)	SPEED (KM/S)	DECEL (M/S/S)	MASS (%)	VISUAL MAG	FRAGMENTS
12.00	52.6	19.4	42	99.85	−15.2	vis 1
12.50	48.6	19.4	74	99.74	−15.8	vis 1
13.00	44.5	18.8	9419	97.48	−21.0	vis 420000
13.50	41.1	14.0	9070	82.89	−19.8	vis 420000
14.00	38.6	10.0	6840	74.96	−18.3	vis 420000
14.50	36.8	7.2	4612	71.24	−16.7	vis 420000
15.00	35.6	5.3	3045	69.51	−15.2	vis 420000

DARK FLIGHT

TIME (S)	HEIGHT (KM)	Long. (deg)	Lat. (deg)	vel (km/s)	vel_L (m/s)	vel_h (m/s)	vel_x (m/s)	zenit angle (deg)
101.00	26.5	54.76997	9.24804	0.03	28.69	−13.16	0.00	65.36
103.00	26.4	54.77047	9.24821	0.04	28.19	−32.38	−0.02	41.04
105.00	26.3	54.77095	9.24837	0.06	27.53	−51.01	−0.05	28.35
107.00	26.2	54.77142	9.24853	0.07	26.66	−68.74	−0.08	21.20
109.00	26.1	54.77186	9.24867	0.09	25.56	−85.25	−0.13	16.69
111.00	25.9	54.77227	9.24880	0.10	24.24	−100.25	−0.17	13.59
113.00	25.7	54.77264	9.24894	0.12	22.70	−113.49	−0.19	11.31
115.00	25.4	54.77300	9.24905	0.13	21.11	−124.77	−0.24	9.60
117.00	25.2	54.77333	9.24924	0.14	19.39	−134.01	−0.08	8.23
119.00	24.9	54.77359	9.24941	0.14	17.48	−141.24	0.09	7.05

[c] This was discussed at the conference.

[d] `http://weather.uwyo.edu/upperair/sounding.html`. Data used for this paper: `http://weather.uwyo.edu/cgi-bin/sounding?region=europe\&TYPE=TEXT\%3ALIST\&YEAR=2019\&MONTH=09\&FROM=1212\&TO=1212\&STNM=10035`.

[e] `https://www.allsky7.net`

[f] NASA Center for Near Earth Object Studies, `https://cneos.jpl.nasa.gov`

Table 3 – Flensburg fireball input used for the ablations and dark flight calculator.

Parameter	value	(E)st/ (M)eas	Reference
Initial velocity V_{inf}	19.43 km/s	M	Borovička et al. (2021)
Begin point λ(t)	9.0322° E	M	Borovička et al. (2021)
Begin point ϕ(t)	53.887° N	M	Borovička et al. (2021)
Begin point h(t)	71.84 km	M	Borovička et al. (2021)
End point λ(t)	9.2060° E	M	Borovička et al. (2021)
End point ϕ(t)	54.598° N	M	Borovička et al. (2021)
End point h(t)	35.3 km	M	Borovička et al. (2021)
Zenith distance	65.3°	M	Borovička et al. (2021)
Ablation coefficient ζ	0.005 s^2/km^2 [g]	E	Borovička (2006), Borovička et al. (2019, 2021)
Heat transfer coefficient Λ	0.1–2	E	Footnote [h], Borovička 2006
Drag coefficient Γ	0.5–0.6	E	Footnote [h], Borovička et al. (2021)
Shape factor A	0.9–1.3	E	Footnote [h]
Luminous eff L_e	0.02–0.20	E	Drolshagen 2021, Gritsevich 2011
Entry mass m	10–22 tons	E	Borovička et al. (2021)
Density ρ	2000 kg/m^3	M	Borovička et al. (2021)
Wind velocity, direction, p(h), T(h)	[m/s, deg, Pa, K]	M	See Table 4

Table 4 – Extract of the weather balloon sounding data from Schleswig, coincidently very close to the fireball location, and around the same time (Footnote [d]).

```
================================================================================
SOUNDING # 1     IDN= 10035    DAY=2019255    TIME=120000     VALID LEVELS= 56
--------------------------------------------------------------------------------
     Idn     Id    Station Name              St  Co   Lat     Lon      Elev
     10035         Schleswig                 DE   54:32N  009:33E  43
--------------------------------------------------------------------------------

  Level    Pressure  Temp  Dew Point  Dir    Speed   Height   Theta   Mix
  Type       [MB]     [C]     [C]     [deg]  [KTS]    [M ]     [K]   [g/kg]
 --------  --------  -----  -------  -----  -------  -------  -----  ------
    SFC     1018.0    17.6    14.7   240.0     7.8     43.0   289.3  10.398
    MAND    1000.0    15.2    13.4   235.0    17.5    195.3   288.4   9.719
    SIGT     970.0    12.8    12.8   244.8    19.8    453.1   288.5   9.632
    SIGT     958.0    11.8    11.6   248.8    20.7    557.8   288.5   9.003

    SIGT     426.0   -20.1   -31.1   290.8    46.4   7005.5   323.0   0.671
    MAND     400.0   -23.5   -37.5   295.0    48.6   7469.4   324.5   0.381
    SIGT     385.0   -25.3   -42.3   295.7    52.0   7748.1   325.7   0.240
    SIGT     347.0   -30.9   -41.9   297.5    61.2   8494.4   327.9   0.278
    SIGT     343.0   -31.7   -37.7   297.7    62.2   8576.5   327.9   0.436
    SIGT     317.0   -34.9   -41.9   299.1    69.1   9130.7   330.9   0.304
    MAND     300.0   -38.3   -44.3   300.0    73.8   9512.8   331.4   0.247
    SIGT     277.0   -42.9   -45.5   300.0    72.1  10056.4   332.4   0.235
    SIGT     265.0   -45.7   -48.5   300.0    71.2  10353.4   332.5   0.177
    MAND     250.0   -48.3   -52.3   300.0    69.9  10739.5   334.3   0.131
    SIGT     241.0   -49.1   -64.1   299.0    71.1  10980.7   336.6   -----
    SIGT     216.0   -52.3   -64.3   296.1    74.5  11694.5   342.3   -----
    MAXW     207.0   -52.3   -67.6   295.0    75.8  11969.9   346.5   -----
    MAND     200.0   -52.3   -70.3   300.0    69.9  12192.6   350.0   -----
    MAND     150.0   -61.1   -79.1   305.0    48.6  14017.1   364.8   -----
    TRO1     138.0   -62.3   -81.3   270.0    42.7  14533.7   371.5   -----
    SIGT     120.0   -58.3   -83.3   270.0    39.4  15405.4   394.0   -----
    MAND     100.0   -60.9   -84.2   270.0    35.0  16546.2   410.1   -----
    MAND      70.0   -59.7   -84.6   265.0    13.6  18770.7   456.7   -----
    MAND      50.0   -55.9   -84.8   235.0    17.5  20893.9   511.8   -----
    SIGT      47.5   -55.5   -84.8   239.0    17.1  21220.7   520.3   -----
    SIGT      38.5   -57.7   -84.9   255.5    15.5  22553.7   546.9   -----
    MAND      30.0   -55.7   -84.9   275.0    13.6  24135.8   592.8   -----
    MAND      20.0   -51.9   -84.9   120.0     1.9  26741.8   677.3   -----
    SIGT      15.7   -52.3   -83.2   164.9     6.6  28309.8   724.6   -----
    MAND      10.0   -43.9   -81.9   250.0    15.5  31284.3   855.7   -----
    SIGT       8.8   -42.1   -81.1   -----   -----  32146.3   894.5   -----
    SIGT       8.3   -42.9   -81.9   -----   -----  32541.7   906.5   -----
```

meteorite. Table 3 gives an overview of all parameters used and their ranges.

Following the recipe given in the beginning of this section we try to match the Borovička velocity profile with the simulation results. Figure 3 shows that we were successful to find a set of parameters results in a reasonable fit [h], but it should be mentioned that the deceleration is small and the measured velocity has a substantial inaccuracy near the end of the luminous trajectory.

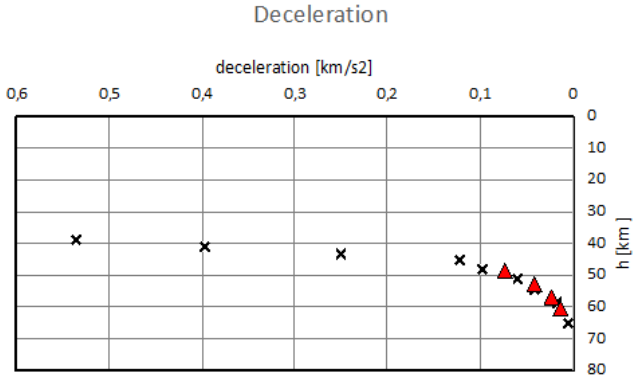

Figure 3 – Measured velocity along trajectory from (crosses, Borovička et al., 2021) and PyDAF (red triangles).

We then calculate the dropping locations for fragments from 5 g to 100 g (including a 24 g fragment, being the mass of the recovered meteorite) for fragmentation heights of 45 km and 35 km. The results are illustrated in Figure 5, plotted on Google Earth map. As expected, all meteorites drift in eastern direction due to the western wind direction, large meteorites travel further than smaller ones, and a fragmentation at a lower height allows the meteoroid to travel further and thus also causes the meteorite to drop further North. In orange we plot the dropping locations as published in Borovička et al. (2021). Our calculator is also able to find a solution that matches the drop location of the 24 g meteorite well, with the simulator suggesting a fragmentation height of ∼ 42 km, whereas Borovička et al. (2021) find 37 km.

[g] The ablation coefficient is of course not precisely known, but we us we use this value as it is often used in simulations. For simplicity, variation of the value can also be expressed in the heat transfer coefficient with has a similar (but reciprocal) effect on the ablation process. Borovička (2006) gives as range 0.001–0.008 s^2/km^2.

[h] Entry mass $m = 10000$ kg, Shape factor $A = 0.9$, Drag coefficient $\Gamma = 0.6$, Heat transfer coefficient $\Lambda = 0.5$.

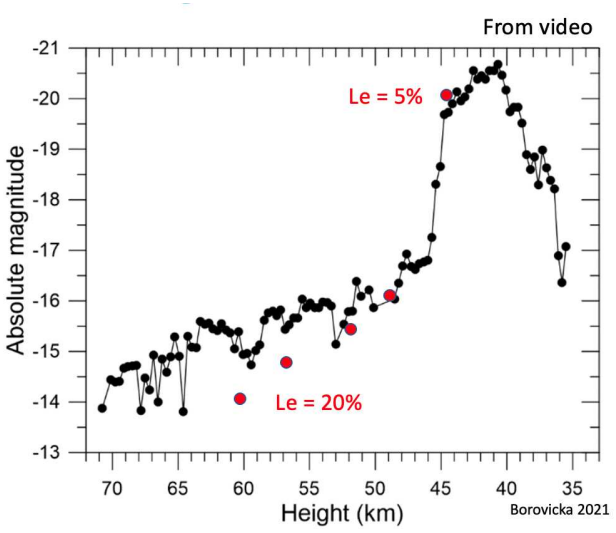

Figure 4 – Brightness profile from Borovička et al. (2021), with indicated with red dots the estimated brightness as computed in this paper.

Figure 5 – Calculated locations of meteorite fragments, being the output of the ablation and dark flight calculator, plotted on Google maps. The blue dashed line and the left illustrates the fireball trajectory, which moved from south to north, with the terminal point not visible being ~ 7 km below the picture. The left line indicate the dropping location of fragments originating from a, the right red line from a fragmentation point at 35 km height. Smaller fragments (5 g) are at the lower side, larger fragments at the top (100 g). For comparison also the output from Borovička et al. (2021) are plotted (orange lines). The blue triangle plots the finding location of the 24 g meteorite fragments.

We do also an attempt to simulate the brightness. In order to match the brightness profile as given in Borovička et al. (2021), we need a luminous efficiency of 0.20, assuming a single body until a height of 45 km, which is on the large side (Drolshagen et al., 2021). We can simulate the brightness starting after 45 km by fragmenting the entire body in sub-gram sized particles and we then need a luminous intensity of 0.05 in order to reach an apparent magnitude brighter than -20, which is the estimate in Borovička et al. 2021 (Figure 4). To model the brightness with fragmentation realistically, the simulator is too simple (offering only one fragmentation at a chosen altitude, splitting the main body in n equal parts).

Figure 6 – Expected dropping locations for a 24 gram fragment created at 45 km height, in the case we vary all unknown input parameters within a certain range (Table 3), and use estimates for the parameters which we would not know if no meteorite was found yet (i.e. density 2000–3000 kg/m^3). The yellow dots and red lines are overplotted from Figure 5.

5 Discussion

Within the available parameter space, we were able to find a reasonable solution to match the deceleration of the trajectory and drop location of the 24 g meteorite fragment. Nonetheless, we required a rather aerodynamic body with shape factor $A = 0.9$, and drag coefficient $\Gamma = 0.6$, thus $A\Gamma = 0.54$, which is a bit smaller than $A\Gamma = 0.65$ by Borovička at al. (2021), and considerably lower than $A\Gamma = 0.8$ which often is used for dark flight computations as first estimate, with $A\Gamma = 0.6$ representing a spherical shape of the meteoroid, which is a good assumption also in the case that a meteorite spins. We like however to emphasize that we did not do any optimization do find the best solution, hence we do not claim that the presented solution is the optimal one: as there are many free parameters in the calculation, there might exist a certain combination of parameters that fit, the test case (slightly) better.

It is interesting to investigate how well we would be able to predict the landing site if a meteorite would not have been recovered yet, and thus rely entirely on the fireball data only. To give insight in the spread in landing side coordinates by varying the input parameters over a certain range, we have computed various extreme cases from Table 2 (i.e. related to heat transfer coefficient, shape factor, drag coefficient, entry mass), while taking care that the deceleration still represents the measured fireball trajectory. The results we have plotted in Figure 6. Based on the average of all the computed geographical coordinates we would 'predict' the landing site of the 24 g segment then roughly a kilometer to the south-east, but still well within the overall expected dropping area.

Finally we want to compare the dynamic pressure.

As reported in Borovička et al. (2021), the dynamic pressure on the meteoroid was 0.7 MPa and 2 MPa at fragmentation heights of respectively 45 and 37 km, which can be computed with $p = \frac{1}{2}\rho_{\rm atm} v^2$. We de-

rive the same, due to the fact that at these heights the main body still did almost not decelerate and thus the only parameters defining the dynamic pressure are the known initial velocity and air density at that height, which both are well-known parameters.

6 Conclusions

Test of PyDAF with a real meteorite dropping fireball has shown that the software tool is able to create a reasonable estimate. The solution is not identical to the results as published in Borovička et al. (2021), but we also did not expect a perfect match as it is evident that the calculator has its limitations. Some parameters vary with velocity or altitude (e.g. heat transfer coefficient (Borovicka, 2006)), for which the calculator does not account for, and as already mentioned a realistic fragmentation model is not part of the tool, which makes it impossible to model correctly the light curve. Also, we did not use exactly the same input data as used in Borovička et al. (2021). For example, we have used sounding data opposite to Borovička who used ECMWF/ALADIN data.

From the computation we did, we could conclude that:

1. the meteoroid had a rather spherical shape, and was very aerodynamic,
2. fragmentation occurred at a height $\sim$ 42 km for the 24 g meteorite (slightly higher than computed in Borovička et al. (2021)),
3. the likely initial mass was 10 000 kg, which gives slightly better results than 22 000 kg, and
4. we apparently did not choose the best fireball for verification: there was only negligible deceleration, the fireball with extreme mass loss, only one small fragment was recovered with also showed a not so common low density.

Knowing that PyDAF has its limitations, we conclude that the tool nonetheless does a reasonable job in modelling the phenomenon. We should not forget that precisely modelling a meteorite's flight is not a simple task, and the precise modelling is a topic of nowadays research. PyDAF is a nice tool for entering into the field of meteoroid flights through the atmosphere, and for studying how the set of parameters influence the flight of a meteoroid, both natural and artificial fireballs and meteors (see for examples the reference in footnote [a]), with a great educational value (for example "does a meteorite hit the ground at an angle or vertical?").

References

Bettonvil D. (2020). "Python ablation and dark flight calculator". In Pajer U., Rendtel J., Gyssens M., and Verbeeck C., editors, *Proceedings of the International Meteor Conference, Bollmannsruh, Germany, 2019 October 3 – 6*. pages 164–165.

Borovicka J. (2006). "Physical and chemical properties of meteoroids as deduced from observations". In Lazzaro D., Ferraz-Mello S., and Fernández J. A., editors, *Asteroids, Comets, Meteors*, volume 229. pages 249–271.

Borovička J., Bettonvil F., Baumgarten G., Strunk J., Hankey M., Spurný P., and Heinlein D. (2021). "Trajectory and orbit of the unique carbonaceous meteorite Flensburg". *Meteoritics & Planetary Science*, **56:3**, 425–439.

Borovička J., Popova O., and Spurný P. (2019). "The Maribo CM2 meteorite fall—Survival of weak material at high entry speed". *Meteoritics & Planetary Science*, **54:5**, 1024–1041.

Ceplecha Z. (1987). "Geometric, Dynamic, Orbital and Photometric Data on Meteoroids From Photographic Fireball Networks". *Bulletin of the Astronomical Institutes of Czechoslovakia*, **38**, 222.

Drolshagen E., Ott T., Koschny D., Drolshagen G., Vaubaillon J., Colas F., Zanda B., Bouley S., Jeanne S., Malgoyre A., Birlan M., Vernazza P., Gardiol D., Nedelcu D. A., Rowe J., Forcier M., Trigo-Rodriguez J. M., Peña-Asensio E., Lamy H., Ferrière L., Barghini D., Carbognani A., Di Martino M., Rasetti S., Valsecchi G. B., Volpicelli C. A., Di Carlo M., Knapic C., Pratesi G., Riva W., Stirpe G. M., Zorba S., Hernandez O., Grandchamps A., Jehin E., Jobin M., King A., Sanchez-Lavega A., Toni A., Rimola A., and Poppe B. (2021). "Luminous efficiency based on FRIPON meteors and limitations of ablation models". *Astronomy & Astrophysics*, **650**, A159.

Gritsevich M. and Koschny D. (2011). "Constraining the luminous efficiency of meteors". *Icarus*, **212:2**, 877–884.

Handling Editors: Francisco Ocaña González and Javor Kac

Minimizing biases of luminous efficiency determinations based on FRIPON data

T. Ott[1], *E. Drolshagen*[1], *D. Koschny*[2,3], *G. Drolshagen*[1], *J. Vaubaillon*[4], *F. Colas*[4], *and B. Poppe*[1]

The French fireball network FRIPON (Fireball Recovery and InterPlanetary Observation Network) collected 3871 confirmed events between April 2016 and June 2020. Of those, a subset of data with physically realistic results and good light curve quality was chosen. For these 281 meteors, the luminous efficiencies τ were computed. Based on this subset, relations of τ and the pre-atmospheric meteoroid velocity, v_e, and mass, M_e, were examined.
Aspects which could cause inaccuracies, influence the results, or render the method less valid were considered. These include the assumed density based on stream associations, the possibility of an observational bias due to missing parts of the trajectory, the final height, the deceleration, and flow regime. 54 well-recorded events could be obtained from the discovered individual biases and constraints. These pre-debiased events have τ -values in the range between 0.012 % and 1.1 % and relations of τ to v_e and M_e of: $\tau = 7.33 \cdot v_e^{-1.10}$ and $\tau = 0.28 \cdot M_e^{-0.33}$. It appears that the derived luminous efficiency of meteoroids is dependent on the assumed material density. By using the pre-debiased subset the results provide evidence that applying a debiasing method improves the analysis of decelerated meteoroids with the underlying method being only valid for meteoroids in the continuum-flow regime. In general, these events feature low end heights, large masses, and high deceleration.

Received 2021 November 1

This work has been presented at the International Meteor Conference 2021 (held online).

1 Introduction

The mass of a meteor's pre-entry meteoroid is a significant characteristic in meteor science. An accurate measurement can be used to approximate the Near-Earth environment and meteoroid fluxes. However, it is still a challenge to obtain. This can be underlined by the large range of luminous efficiency values published in literature in the last years. A review of recent studies show a variation between 0.02 - 40% for a mass range of $10^{-6} - 10^{13}$ (Drolshagen et al., 2021a). There are various methods attempting a well constrained determination. They are based on experimental and observational techniques and can be categorized by the kind of data used for the calculations. E.g. the luminous mass is primarily based on the light curve information of a recorded meteor and the dynamic mass on velocity information. The photometric mass makes use of the dimensionless parameter called luminous efficiency τ. It quantifies how much of the kinetic energy E of the entering object is converted into observable brightness I. Ceplecha et al. (1998) define the relation as follows:

$$I = -\tau \cdot \frac{dE}{dt}. \tag{1}$$

The meteoroid mass M_e before it's entry into the atmosphere can be computed using Equation (2)

$$M_e = \frac{2}{\tau \cdot v_e^2} \int I_s \; ds \tag{2}$$

with the term $\int I_s \; ds$ giving the emitted light I in Watts, integrated over the complete flight path s (Verniani, 1965).

A pre-atmospheric mass computation method that has gained a lot of popularity in the last years was introduced in Gritsevich (2008). Instead of recorded brightness values, it uses the time-dependent meteoroid's altitude and its deceleration rate during its flight through the atmosphere. This way the so called dynamic mass can be determined without considering the luminous efficiency.
Results from this method have already lead to some meteorite sample recoveries. One prominent event is the Annama meteorite (Gritsevich et al., 2014).

The dynamic mass method can be in turn used to compute the luminous efficiency as shown in Gritsevich & Koschny (2011). Taking into account the changes in the meteoroid's velocity and mass during its descent while considering the geometrical relation of the meteor, they were able to solve the formulas for the meteoroid's dynamical behavior. These calculations were based on the equations for drag and mass loss. The results derived this way were then compared to the drag rate and light curve observed for the considered meteor. Afterwards, τ was computed based on this comparison (Gritsevich & Koschny, 2011).
It should be noted that the method considers the entire mass and does not take fragmentation into account.

With the dimensionless velocity v, τ was calculated as stated in Equation (3). Using $f(v)$ as defined in Equation (4) and the exponential integral $\overline{Ei}(x)$ (Equation (5)).

[1]University of Oldenburg, Division for Medical Radiation Physics and Space Environment, Germany.
theresa.ott@uni-oldenburg.de
[2]European Space Agency, ESTEC, Keplerlaan 1, 2201 AZ Noordwijk, The Netherlands.
[3]Chair of Astronautics, TU Munich, Germany.
[4]IMCCE, Observatoire de Paris, PSL Research University, CNRS UMR 8028, Sorbonne Université, France.

IMO bibcode WGN-496-ott-luminous
NASA-ADS bibcode 2021JIMO...49..152O

Thus introducing another dimensionless parameter called the shape change coefficient μ.
In order to determine τ and μ a least-squares fit is applied to the recorded light curve.

$$I(v) = \frac{\tau \cdot M_e \cdot v_e^3 \cdot \sin(\gamma) \cdot f(v)}{2 \cdot h_0} \tag{3}$$

$$f(v) = v^3 \cdot \left(\overline{Ei}(\beta) - \overline{Ei}(\beta \cdot v^2)\right) \cdot \left(\frac{\beta \cdot v^2}{1-\mu} + 1\right) \cdot \exp\left(\frac{\beta \cdot (\mu \cdot v^2 - 1)}{1-\mu}\right) \tag{4}$$

$$\overline{Ei}(x) = \int_{-\infty}^{x} \frac{e^z}{z} dz, \tag{5}$$

Applying this method to FRIPON data will be the base of this research.

2 Influences on computations

Several studies have previously investigated the luminous efficiency. One interesting aspect showed a relationship between the luminous efficiency and e.g. the velocity of the meteoroid.
Few publications explore other parameters, but a study by Drolshagen et al. (2021b) provides an overview of multiple dependencies, for example, the meteoroid's pre-atmospheric mass M_e, velocity, entry angle, and composition.

In this study the $\tau - M_e$ relationship will be explored, comparing it to recent studies done for example by Subasinghe & Campbell-Brown (2018) and Čapek et al. (2019).
The work of Subasinghe & Campbell-Brown (2018) is a follow up paper to Subasinghe et al. (2017) and uses the introduced numerical approach on 12 non-fragmenting meteors recorded by the Canadian automated meteor observatory (CAMO, see for example Weryk et al. (2013)). The pre-atmospheric masses range from 10^{-6} kg to 10^{-4} kg. The determined luminous efficiencies are in the range of 10^{-2} % – 10^{2} (Drolshagen et al., 2021a). From their results, they established a weak relationship between τ and M_e. However, the values are spread over a large range and the small data set of only 12 events might limit the informative value (Subasinghe & Campbell-Brown, 2018). A quite similar relation was given by Čapek et al. (2019) from data of 53 faint, slow, and low altitude meteors. The light curves of which were recorded with double station video observations and are most likely the product of small iron meteoroid entries.

The light curve data of the observations is often one of the most inaccurately recorded characteristics as the brightness determination and calibration poses a challenge especially to wide field observations. The FRIPON observations also suffer from thereby introduced uncertainties. We address this problem by combining data of multiple camera recordings and excluding individual values. Excluded values lie further than 0.5 mag from the median. If only two values with a deviation larger than 0.5 mag are encountered, only one value remains. If the light curve does not have enough data points left, the event is eliminated from the dataset.

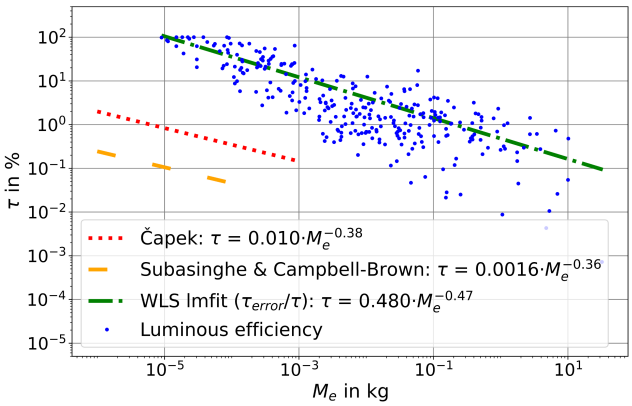

Figure 1 – Luminous efficiencies of 281 FRIPON events shown over the corresponding meteoroid's mass. Blue dots: τ values; green line: by relative error of the value weighted least-square fit (WLS); blue dashed line: Čapek et al. (2019) results; orange dashed-dotted line: Subasinghe & Campbell-Brown (2018) results.

By applying various other requirements on the event characteristics, we constrain the set further. The details can be found in Drolshagen et al. (2021a). The presented analysis is based on 281 FRIPON events with reasonably good data as well as event parameters.

However, considering determined τ values that range from 10^{-4} % to 100 %, these requirements seem to be insufficient. Even though 70% lie between 0.1 % and 10 %. As previously stated, investigating the dependencies these calculations are based on, it could be shown that smaller meteoroids radiate more efficiently than larger ones. This was as expected and recent publications also reported a relation between τ and the pre-atmospheric meteoroid's mass. They quantified this as Čapek et al. (2019): $\tau = 0.010 \cdot M_e^{-0.38}$, Subasinghe & Campbell-Brown (2018): $\tau = 0.0016 \cdot M_e^{-0.36}$. Comparable analysis of the 281 FRIPON event dataset finds a dependency of $\tau = 0.48 \cdot M_e^{-0.47}$. See Figure 1 for a visual representation. The slope is very similar, however there is a shift towards larger luminous efficiencies. This shift, especially considering some unphysically high τ values close to 100%, seem to point to biases still present in the dataset.

In order to explore the underlying causes, possible biases and influences and their affect on the deviation of the luminous efficiency are studied. These were introduced in Drolshagen et al. (2021b) and consist of: Incompleteness of data, deceleration, final heights of objects, assumed meteoroid densities and flow regimes in the atmosphere.

2.1 Density assumptions

Drolshagen et al. (2021a) found a rather high impact on the τ computation of the assumed bulk density of meteoroids. The density is used to calculate the pre-atmospheric masses. Therefore, to qualify the den-

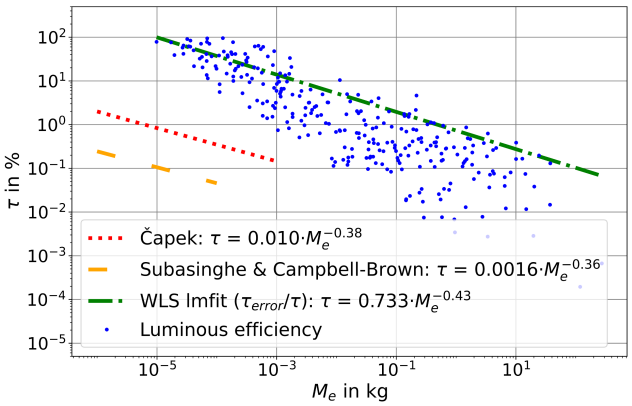

Figure 2 – Luminous efficiencies of FRIPON events over the corresponding meteoroids' masses calculated with meteoroid densities based on shower associations. Blue dots: τ values; green dash-dotted line: by relative error of the value weighted least-square fit (WLS); blue dashed line: Čapek et al. (2019) results; orange dashed-dotted line: Subasinghe & Campbell-Brown (2018) results.

sity's effects the luminous efficiency computation was repeated with varying bulk density estimates. The density can be refined if additional information on the meteoroid are known. In this study possible stream associations and parent body density estimates are used. Of the 281 FRIPON events, 99 were associated with a shower.

As shown in Figure 2, the fit for the dataset with shower associations used for the pre-atmospheric masses is changed to $\tau = 0.733 \cdot M_e^{-0.43}$.
Varying the standard density assumptions of all meteoroids without taking shower associations into account reveals that a decreasing bulk density assumptions show a decrease in τ and an increase in M_e.

2.2 Incompleteness of recordings

Moreover, this work studies a possible observational bias due to incompletely recorded meteor trajectories and thus inchoate lightcurves. One example is shown in Figure 3 where between 50 % and 100 % of the lightcurve remain for the τ computations. The obtained

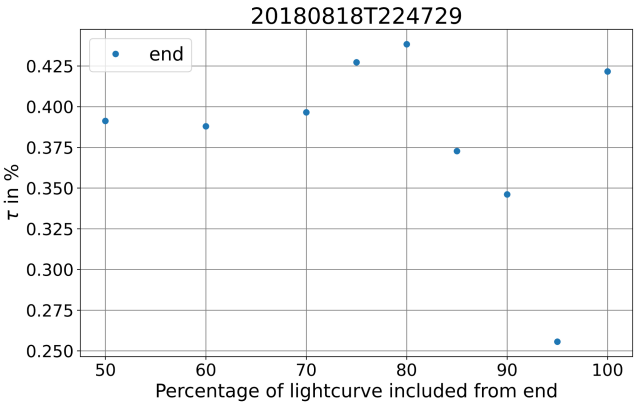

Figure 4 – Luminous efficiencies of the FRIPON event 20180818T22472 calculated for incomplete lightcurve data. The results remain relatively stable even for quite inchoate observations.

luminous efficiency values were compared to those of the complete lightcurve (see Figure 4). This test was iterated for a set of recordings with examplary parameters. Systematically, the results show a relatively stable luminous efficiency calculation regardless of completeness. Therefore, the number of datapoints used for the computations were not investigated further.

2.3 Flow regimes

One significant factor is the applied method itself. The method presented by Gritsevich (2008) might only be valid for certain types of fireballs recorded. For the applicability of the model it is assumed that ablation of the entering meteoroid is the main interaction process with the atmosphere. (Please note that fragmentation was not taken into consideration and might influence the results.)

One parameter to quantify the atmospheric conditions encountered by the meteoroid as well as its interactions is the Knudsen number. The atmosphere is made up of layers defined by temperature and density. They change by height and can be sectioned based on the mean free path length of its molecules which is con-

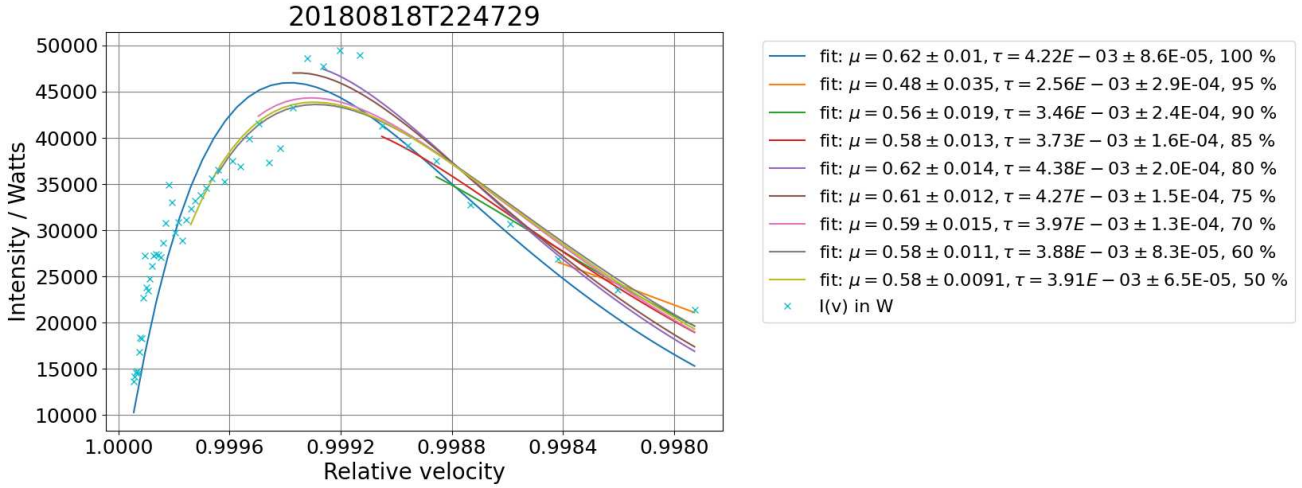

Figure 3 – Lightcurve of the FRIPON event 20180818T22472. The luminous efficiency computations were carried out on varying parts of the lightcurve remaining, as indicated by the percentage given in the legend. The percentage is given for the end part.

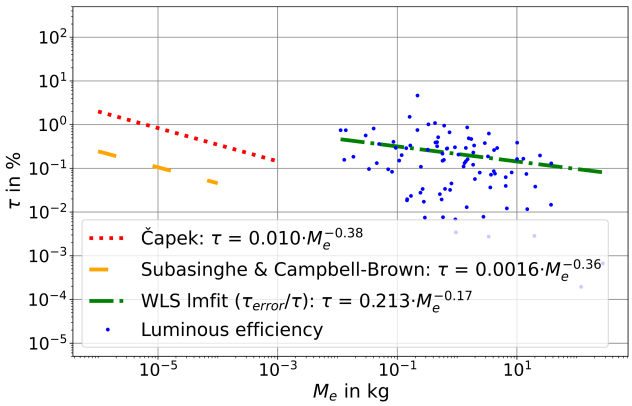

Figure 5 – Luminous efficiencies of FRIPON events which were first observed in regions of the atmosphere and at speeds at which they encounter continuous flow.

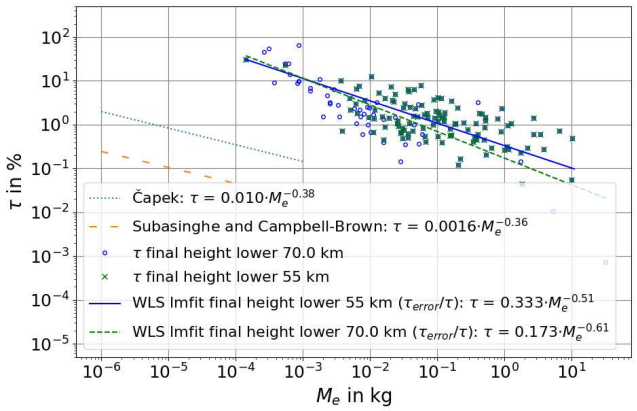

Figure 6 – Luminous efficiencies of the FRIPON events with end heights lower than 55 km (blue dots) and end heights lower 77 km (green crosses).

nected to the number of collisions encountered by an entering object. The model is valid for continuum mechanics which are encountered in the continuous flow regime (Drolshagen et al., 2021b).
This study investigates the final height of recorded objects in more detail to determine this influence. 93 of the events in our dataset were initially recorded in the continuum-flow regime. The influence on the τ computations can be seen in Figure 5.

2.4 Final height

Meteoroids that penetrate deep into the atmosphere have usually undergone larger deceleration than objects with high final heights (see Drolshagen et al. (2021b)). The deceleration has a significant effect on the method used. A more extensive analysis and explanation is given in Section 2.5. It is expected that objects with lower end height tend to have better quality data since they are easier to record. Also, they tend to have larger pre-atmospheric masses. Additionally, the lack of deceleration in the data might point towards instrumentation limitations manifested as positional imprecision. Taking these factors into account, the influence of the final height on the τ computations is investigated. Two datasets are created based on the last height observed by the system. The first is a subset of events with end heights h_{final} lower than 70 km and the second further constrains the dataset to only those with h_{final} lower 55 km. The second dataset is a subset of the first.

Figure 6 shows both datasets with the first marked by blue dots and the second by green crosses. It is evident that objects with low pre-atmospheric masses are no longer present in both datasets. Also, the unphysically high τ values are missing since they were connected to the particularly small meteoroids.

2.5 Deceleration

The applied method, presented by Gritsevich (2008), is based on trajectory data of the entering meteoroids. In particular, the height and velocity information used to calculate the deceleration of the objects. Meteoroids that show a strong deceleration should be particularly well suited for the method. In consequence, the obtained results are expected to be of good quality for objects with a high deceleration. Thus, it is expected that the objects' deceleration should have quite a significant effect on the computations and will be investigated in more detail.

From the first and last recording of the meteor, the difference in velocity is computed. Put into relation to the maximum velocity at entry, a relative velocity $(v_e - v_{final})/v_e)$ is calculated. A visual representation can be found in Figure 7. The luminous efficiencies are plotted against the object's relative velocity change with the corresponding meteoroids' final heights h_{final} color-coded.

Objects with relatively low measured relative velocity change seem to dissipate quickly. They have large final end heights, not penetrating deep into the atmosphere. Objects with lower end heights are associated with a larger relative velocity change. It seems that the luminous efficiency is spread over all represented orders of magnitude for the entire range of relative velocity changes. But, on closer inspection it is evident that the largest and smallest values of τ only occur for objects that do not penetrate deep into the atmosphere and display a rather small relative velocity change. The apparent hole in the distribution of data points in Figure 7 can be attributed to the bimodal velocity distribution already shown in Drolshagen et al. (2021a). This is

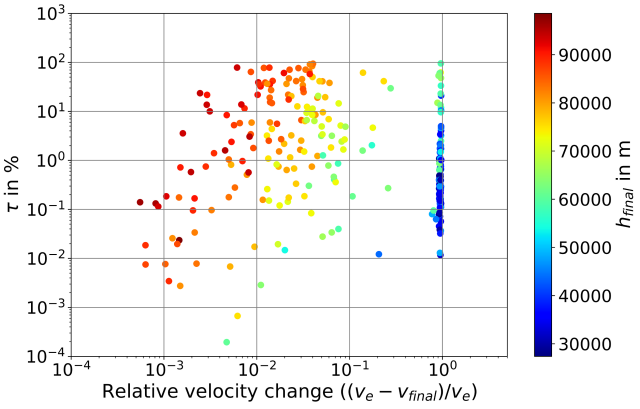

Figure 7 – Luminous efficiencies as derived in this work plotted over the object's relative velocity change for the analyzed objects with the corresponding meteoroids' final heights h_{final} color-coded.

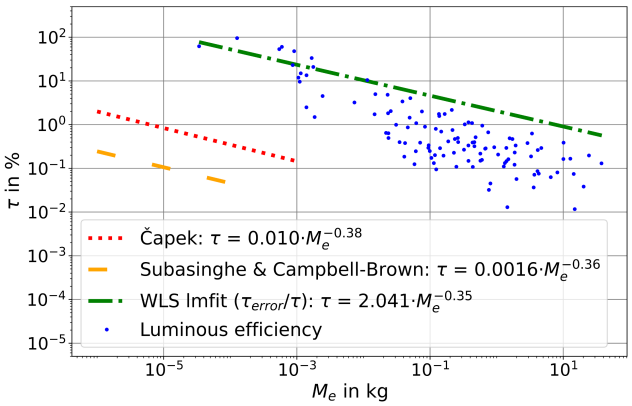

Figure 8 – Luminous efficiencies as derived in this work showing only events with a high deceleration based on the relative velocity change $(v_e - v_{final})/v_e < 0.8$.

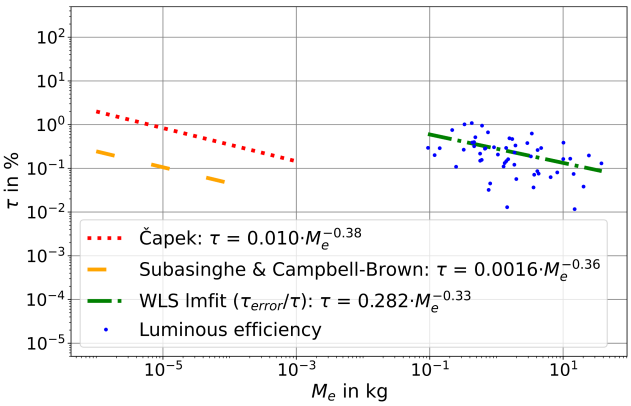

Figure 9 – Luminous efficiencies as derived in this work. the presented data is a subset of 54 FRIPON events that have been chosen based on their final height, deceleration and atmospheric environment. The events are expected to be less affected by biases and thus of the highest quality in the entire dataset.

the result of the high proportion of shower meteors and their characteristic velocities and final heights.

In order to debiase the datase in this regard, a subset was created consisting of events with high recorded deceleration according to the relative velocity change $(v_e - v_{final})/v_e$. Only objects with relative velocity change lower 0.8 are considered. To further explore the effects of the deceleration on the luminous efficiency computations, τ was plotted over the pre-atmospheric mass M_e and a least-square fit was used to quantify the relation between τ and M_e. This is shown in Figure 8. 124 events satisfy the criterion $(v_e - v_{final})/v_e > 80$ %. The WLS fit produced:

$$\tau = 2.041 \cdot M_e^{-0.35}. \tag{6}$$

The slope of the fit is consistent with the ones found by Čapek et al. (2019) and by Subasinghe & Campbell-Brown (2018). However, the results seem to be shifted towards larger luminous efficiencies compared to the ones found by these two studies.

Deceleration seems to be a strong indication of promising events for the computations. Greatly decelerated objects can be easier recorded by FRIPON. Additionally, these are usually larger objects that penetrate deep into the atmosphere, as can be clearly seen in Figure 7 in association to the longer observation durations. Thus, our method is especially applicable to these objects.

3 Final dataset

The influences on the data computation show that some biases are more pronounced than others. It was found that especially the encountered flow regime, the deceleration of the object and the end height have the large effect on the obtained results. In order to minimize these influences, a new dataset is created taking only events into account that lie within certain thresholds of these parameters that are considered to be favorable for good quality measurements.
54 events fall into the category of a final height of less than 70 km, a relative deceleration larger than 0.8 while still being in the continuous flow regime.

Figure 9 shows the luminous efficiency of these events plotted against the entry mass. The obtained weighted least-squares fit is $\tau = 0.282 \cdot M_e^{-0.33}$. This is a similar slope to the one found by Subasinghe & Campbell-Brown (2018) and Čapek et al. (2019).
Evidently, there are no unphysically high τ values remaining. This final dataset can be considered as almost free of biases. This pre-debiased dataset can be used to infer further correlation of various meteor parameters.

4 Conclusion

This study presented a comprehensive analysis of various influences on the calculation of the dynamic mass. The used method is based on the one presented by Gritsevich (2008). The results and interpretations made it possible to select a pre-debiased subset of events with good quality data. The derived luminous efficiency values for those can be expected to be of good quality. The subset is made up of only meteors that occur in the continuum-flow regime and tend to have low end heights, large masses, and a large deceleration during the observed trajectory.
Fur future studies it is suggested to further explore the pre-debiased dataset for correlations and physical links of various parameters and meteor characteristics. Also, observational dependencies might be inferred.

For further details the reader is referred to Drolshagen et al. (2021b).

(Note: For colored figures see the online version of the paper.)

References

Čapek D., Koten P., Borovička J., Vojáček V., Spurný P., and Štork R. (2019). "Small iron meteoroids. Observation and modeling of meteor light curves". *Astronomy and Astrophysics*, **625**, A106.

Ceplecha Z., Borovička J., Elford W. G., Revelle D. O., Hawkes R. L., Porubčan V., and Šimek M. (1998). "Meteor Phenomena and Bodies". *Space Science Reviews*, **84**, 327–471.

Drolshagen E., Ott T., Koschny D., Drolshagen G., Vaubaillon J., Colas F., Zanda B., Bouley S.,

Jeanne S., Malgoyre A., Birlan M., Vernazza P., Gardiol D., Nedelcu D. A., Rowe J., Forcier M., Trigo-Rodriguez J. M., Peña-Asensio E., Lamy H., Ferrière L., Barghini D., Carbognani A., Di Martino M., Rasetti S., Valsecchi G. B., Volpicelli C. A., Di Carlo M., Knapic C., Pratesi G., Riva W., Stirpe G. M., Zorba S., Hernandez O., Grandchamps A., Jehin E., Jobin M., King A., Sanchez-Lavega A., Toni A., Rimola A., and Poppe B. (2021a). "Luminous efficiency based on FRIPON meteors and limitations of ablation models". *Astronomy and Astrophysics*, **650**, A159.

Drolshagen E., Ott T., Koschny D., Drolshagen G., Vaubaillon J., Colas F., Zanda B., Bouley S., Jeanne S., Malgoyre A., Birlan M., Vernazza P., Gardiol D., Nedelcu D. A., Rowe J., Forcier M., Trigo-Rodriguez J. M., Peña-Asensio E., Lamy H., Ferrière L., Barghini D., Carbognani A., Di Martino M., Rasetti S., Valsecchi G. B., Volpicelli C. A., Di Carlo M., Knapic C., Pratesi G., Riva W., Stirpe G. M., Zorba S., Hernandez O., Grandchamps A., Jehin E., Jobin M., King A., Sanchez-Lavega A., Toni A., Rimola A., and Poppe B. (2021b). "Luminous efficiency of meteors derived from ablation model after assessment of its range of validity". *Astronomy and Astrophysics*, **652**, A84.

Gritsevich M. and Koschny D. (2011). "Constraining the luminous efficiency of meteors". *Icarus*, **212:2**, 877–884.

Gritsevich M., Lyytinen E., Moilanen J., Kohout T., Dmitriev V., Lupovka V., Midtskogen V., Kruglikov N., Ischenko A., Yakovlev G., Grokhovsky V., Haloda J., Halodova P., Peltoniemi J., Aikkila A., Taavitsainen A., Lauanne J., Pekkola M., Kokko P., Lahtinen P., and Larionov M. (2014). "First meteorite recovery based on observations by the Finnish Fireball Network". In Rault J. L. and Roggemans P., editors, *Proceedings of the International Meteor Conference, Giron, France, 18-21 September 2014*. pages 162–169.

Gritsevich M. I. and Popelenskaya N. V. (2008). "Meteor and fireball trajectories for high values of the mass loss parameter". *Physics - Doklady*, **53:2**, 88–92.

Subasinghe D. and Campbell-Brown M. (2018). "Luminous Efficiency Estimates of Meteors. II. Application to Canadian Automated Meteor Observatory Meteor Events". *The Astronomical Journal*, **155:2**, 88.

Subasinghe D., Campbell-Brown M., and Stokan E. (2017). "Luminous efficiency estimates of meteors -I. Uncertainty analysis". *Planetary and Space Science*, **143**, 71–77.

Verniani F. (1965). "On the Luminous Efficiency of Meteors". *Smithsonian Contributions to Astrophysics*, **8**, 141.

Weryk R. J., Campbell-Brown M. D., Wiegert P. A., Brown P. G., Krzeminski Z., and Musci R. (2013). "The Canadian Automated Meteor Observatory (CAMO): System overview". *Icarus*, **225:1**, 614–622.

Handling Editors: Ákos Kereszturi and Javor Kac
This paper has been typeset from a LaTeX file prepared by the authors.

Observations (from 2016 to 2020) of the Geminids from different regions of Russia by an amateur astronomer

Filipp Romanov[1]

I present the results of my observations (visual and photographic) of the Geminid meteor shower in 2016, 2018, 2019 and 2020. I observed meteors from different regions (Moscow and Primorsky Krai) of Russia, under different observation conditions: light pollution, Moon phases and weather. I used a DSLR camera with a lens to photograph meteor tracks. I compare the results of my visual observations in different years and determine the coordinates of the meteors from the photographs to graphically demonstrate the radiant.

Received 2021 November 5

This work has been presented at the International Meteor Conference 2021 (held online).

1 Introduction

The Geminids are a prolific annual meteor shower and are favorable for observations in the Northern Hemisphere of the Earth. It is known that asteroid (3200) Phaethon is the parent body of this meteor shower. Figure 1 shows the image of this asteroid taken (by my request) remotely using 0.355-m $f/6.2$ Schmidt-Cassegrain telescope of Abbey Ridge Observatory, Canada (Lane, 2018). The results of my astrometric measurements (for dates 2021 September 14 and 15: near aphelion) were published in the Minor Planet Electronic Circular MPEC 2021-S21 (Minor Planet Center, 2021).

I have observed meteor showers and submitted my observations to the VMDB: Visual Meteor Database (Roggemans, 1988) of the International Meteor Organization since 2013. I have used my camera Canon EOS 60D with 18–135 mm $f/3.5$–5.6 lens for photographing meteors during visual observations all these years (before when the display and camera lens were damaged in 2021).

I chose the Geminids to describe in this paper from all the meteor showers that I have observed, because I have observed a sufficient number (several hundred) meteors of this shower, from different regions of Russia under different sky conditions (but always in cold weather: at temperatures ranging from -10 to -20°C).

I tried to observe the Geminids for the first time from the science city of Korolyov (in Moscow Oblast) near maximum activity in December 2013 and 2014, but in this region, it is usually cloudy this month, therefore, I had to observe through gaps in the clouds for a short time, and on both occasions the observation time was no more than 10 minutes, and I saw only 2–3 meteors. In 2015 and 2017, there were no gaps in the clouds, and I could not observe the Geminids, so my only useful observation over those years was the observation in December 2016 from Moscow.

[1]Amateur astronomer, Russia. ORCID: 0000-0002-5268-7735
Email: filipp.romanov.27.04.1997@gmail.com

IMO bibcode WGN-496-romanov-geminids
NASA-ADS bibcode 2021JIMO...49..158R

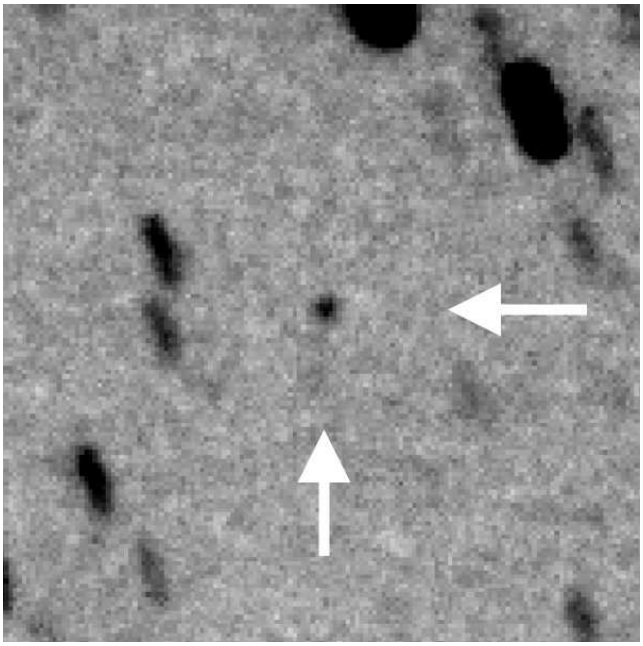

Figure 1 – Stacked image of Phaethon from 10 photos (60 s exposure time, unfiltered) taken on 2021 September 15, from $05^{h}07^{m}$ to $05^{h}59^{m}$ UTC. North is up, field of view is 2 arcminutes.

2 My results of observations of Geminids for different years

2.1 Observations in 2016 from Moscow

In 2016, on the night of December 13/14, when I still lived in the room in the communal apartment in Moscow (geographic coordinates: 55°38′21.7″ N, 37°40′23.3″ E), I observed Geminids well for the first time. I monitored the weather, and after the sky cleared almost completely (which is very rare for December weather in Moscow), I went out to the loggia for observation, dressed warmly. The transparency of the atmosphere was poor (and made worse by the light of the full Moon and light pollution), I estimated the limiting magnitude (LM) at +3.05.

I observed and photographed from $21^{h}50^{m}$ to $22^{h}50^{m}$ UTC (from $00^{h}50^{m}$ to $01^{h}50^{m}$ by local time). During the observation, I saw 9 Geminid meteors: I estimated their brightness and recorded the direction and time of appearances (which I always do when observing meteors). My visual report was published in the VMDB under the number (ID) 74051.

Photographs were taken automatically in succession at focal length 18 mm, exposures of 11 and 12 seconds,

Table 1 – Data about meteors in 2016.

No	Time	Beginning		End	
	(UTC)	α (°)	δ (°)	α (°)	δ (°)
1	21:53	91.81	1.51	89.69	−2.12
2	22:02	113.42	−18.61	113.45	−22.91
3	22:05	104.24	−10.06	103.47	−13.77
4	22:34	103.75	−22.94	103.05	−26.93
5	22:37	114.79	7.83	114.79	−3.75
6	22:47	90.72	−5.69	87.47	−11.54

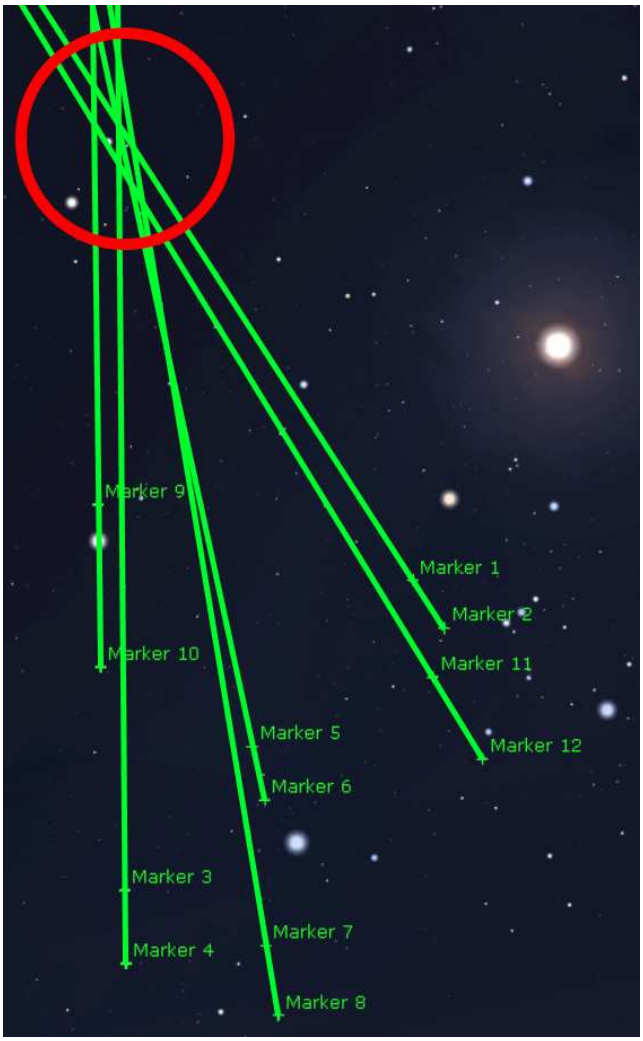

Figure 2 – Tracks of meteors in the sky chart according coordinates from photographs taken on the night of 2016 December 13/14.

ISO-250, $f/3.5$. Due to the blur of the stars in the photos during the exposure time, it is impossible to determine the positions of meteors precisely. Some meteors appeared in the interval between the opening and closing of the shutter (about 2 seconds of time), so they were not photographed. There are six meteors in the photos (of which I saw five visually).

I determined coordinates of the beginning and end of each of them (presented in Table 1), and put them in the form of markers on the gnomonic projection of sky map (in Figure 2) in Stellarium software. Then I drew lines through the points, and they approximately converge in the area of several degrees around the position: RA = 112.5°, Dec = +33.2° — near the Geminids radiant.

2.2 Observations in 2018 from Primorsky Krai

In 2018, I observed the Geminids from my small homeland: in Yuzhno-Morskoy (part of the city Nakhodka), Primorsky Krai (in the Far East). Geographic coordinates of the observation point: 42°51′30.3″ N, 132°41′17.6″ E. On the night of December 13/14 there was a haze in the sky and LM = 3 . . . 4. Between 15^h30^m and 18^h00^m UT, I saw 12 Geminid meteors. My report ID = 78117 in the VMDB.

I observed it for a second time that year on the night of December 14/15. I saw 172 meteors of the Geminids (and 2 sporadic meteors) between 14^h30^m and 19^h16^m (with a few short breaks) UTC. It was a very beautiful and impressive show in the dark sky (LM = 4.5 . . . 5.5). I often saw meteors and, in addition, comet 46P/Wirtanen (near the perihelion) was clearly visible (in the form of a nebulous star) with the naked eye.

My reports were published in the VMDB under the numbers: 78118, 78119, 78128, 78129, 78130, 78135, 78136, 78137. On those dates I also did free live streams of the Geminids on the Internet for viewers at my YouTube channel (the method was as follows: photographs taken with my DSLR camera were immediately shown on the computer and this image was shown live).

I made the composite photo from 14 photographs taken between 14^h06^m and 16^h42^m UTC using my DSLR camera (for each frame: exposure time 30 seconds, focal length 18 mm, ISO-1250, $f/3.5$). This was my first composite image of the Geminids (shown in Figure 3), the comet is also visible there. In total, several dozen meteors were recorded in the photographs taken on the night of 2018 December 14/15.

Based on visual observation data from several observers (including my observations) on the page "Geminids 2018 ZHR Graph – Peak" of the IMO website, a point with ZHR = 138.5 (error range: 128.84–148.24) has been determined for 2018 December 14, 16^h01^m UTC.

2.3 Observations in 2019 from Primorsky Krai

In 2019, the Geminids reached maximum just after full Moon. I observed (and made the live stream) this on the night of December 14/15 (also from Yuzhno-Morskoy).

Despite the bright moonlight, during the night (between 14^h20^m and 21^h30^m UTC with a few short breaks) I was able to see 64 meteors of the Geminids and 2 sporadic meteors; atmosphere transparency was good (LM = 4 . . . 4.95).

I have found that the light of the Moon greatly reduces the number of visible meteors. IDs of my reports: 79739, 79750, 79767, 79768, 79769, 79770.

Figure 4 shows my composite image of meteors from 18 photographs (for each frame: exposure time 20 s, focal length 19 mm, ISO-800, $f/3.5$) taken from 14^h13^m UT to 16^h28^m UT.

Figure 3 – Composite image of the Geminids in 2018.

Figure 4 – Composite image of the Geminids in 2019.

2.4 Observations in 2020 from Primorsky Krai

I observed (and did live stream) this meteor shower on the night of 2020 December 13/14, from Yuzhno-Morskoy. I saw 178 Geminid meteors (and one meteor from the Puppid-Velid meteor shower, and 16 sporadic meteors) between $15^{h}13^{m}$ and $21^{h}25^{m}$ (with a few short breaks) UTC. LM was 5.5 most of the time, but by morning it had become 4.5 . . . 5.3.

I used a voice recorder to record information about the meteors I saw, including the magnitude and shower membership, and later I listened back to it and wrote down the data. IDs of my reports: 81864, 81924, 81926, 81927, 81928, 81929, 81940, 81941, 81942, 81943.

Figure 5 shows my composite image from 25 photographs (for each frame: exposure time 30 s, 19 mm, ISO-3200, $f/3.5$) taken from $14^{h}29^{m}$ UT to $18^{h}05^{m}$ UT.

Table 2 – Data about meteors in 2020.

No	Time	Beginning		End	
	(UTC)	α (°)	δ (°)	α (°)	δ (°)
1	14:16	57.80	16.13	55.10	14.53
2	14:29	73.04	−3.59	68.06	−8.94
3	15:15	85.55	−6.88	84.55	−8.43
4	16:02	66.44	15.84	62.28	13.52
5	16:03	86.93	11.80	83.90	8.80
6	16:07	90.26	21.71	86.35	19.38
7	16:12	83.45	5.19	82.03	3.57
8	16:15	96.91	9.48	94.35	5.35
9	16:17	111.80	2.44	111.48	−3.38
10	16:26	110.30	10.11	109.70	5.86
11	16:28	91.43	26.33	88.99	25.40
12	16:43	115.45	−7.35	115.83	−16.59
13	16:43	102.47	21.81	100.97	20.10
14	16:45	72.53	5.75	68.00	2.06
15	16:52	97.01	12.94	94.84	9.89
16	16:52	95.46	6.37	92.91	2.10
17	16:54	107.50	16.75	106.48	14.11
18	16:57	117.36	12.79	117.80	9.87
19	17:02	88.02	−9.15	85.95	−12.61
20	17:20	119.23	17.00	120.31	13.04
21	17:20	132.11	10.93	134.69	7.65
22	17:26	125.13	12.71	126.56	9.63
23	17:27	123.77	−7.31	124.59	−11.51
24	17:31	128.78	16.02	130.57	13.81
25	17:35	104.79	17.82	103.63	15.62
26	17:37	125.17	10.04	127.06	5.49
27	17:38	113.64	−6.10	113.65	−9.00
28	17:43	103.10	7.17	101.72	3.51
29	17:58	90.54	−4.80	88.11	−8.97
30	18:04	112.21	23.07	111.50	19.68
31	18:05	115.96	26.41	116.12	25.58
32	18:05	88.33	6.87	83.93	1.97
33	18:08	133.48	21.81	136.61	19.55

Figure 5 – Composite image of the Geminids in 2020.

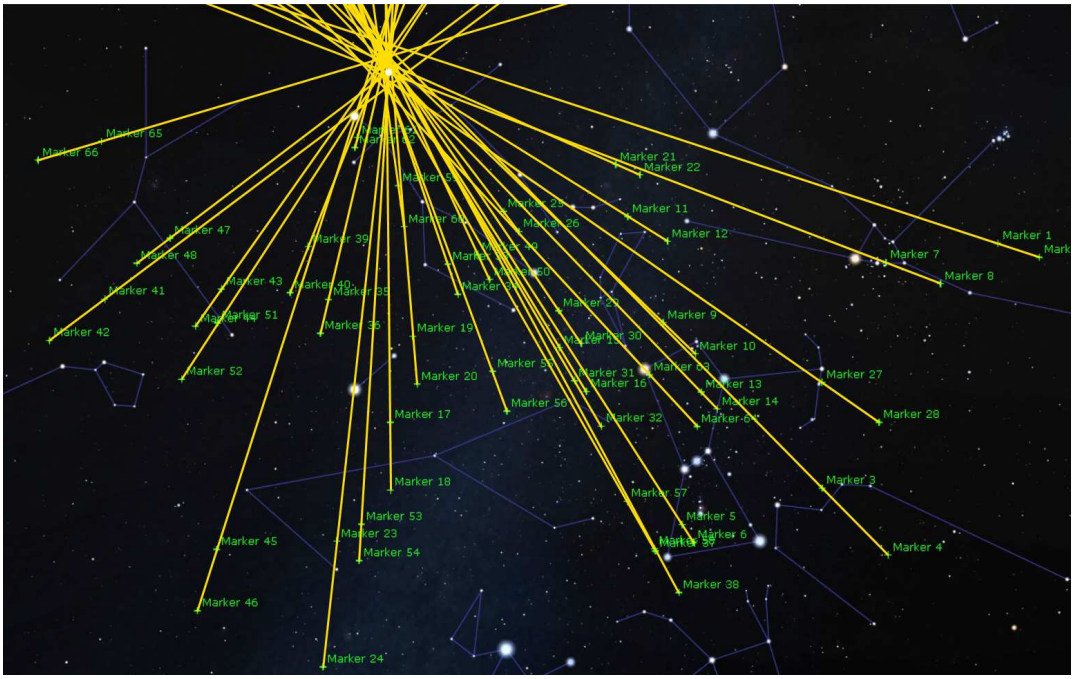

Figure 6 – Tracks of 2020 meteors in the sky chart

I determined the coordinates (these data are presented in Table 2) of the beginning and of the end of each of 33 meteors (that were in my photos from $14^{h}16^{m}$ to $18^{h}08^{m}$ UT) and marked them in the sky map (gnomonic projection) in the Stellarium software. Taking into account the distortion at the edges of the lens, after continuation of the lines, they converge near the point RA = 113.5°, Dec = +32.5° (in the Figure 6): this almost coincides with the radiant of the Geminids. A total of about 50 meteors were captured in my photographs that night.

3 Conclusions

On 2017 January 23, I lost opportunity to live safely and unhindered in a room (and I lost access to my telescopes) in the communal apartment in Moscow, and I had to leave Moscow, but I continued to observe meteor showers from different regions of Russia, in which I was for some time during these years.

As a result of my visual observations of the Geminids over several years under different weather conditions and in different regions of Russia, I have concluded that in order to detect a large number of meteors of

this shower, it is necessary to be in an area where the weather is often clear in December, and it is necessary to have the conditions: the absence of light pollution and the Moon below the horizon, and that the best time to observe is near the predicted maximum activity of this spectacular meteor shower. In my experience, due to the cold December nights during observations, it is necessary to wear warm clothes in order to prevent hypothermia of the body.

In the graphic way, I have shown that using even simple photographic equipment, it is possible to determine the approximate radiant of a meteor shower from the results of photography. To do this, one needs to determine the coordinates of the trails of meteors and plot them on the sky map in order to continue the lines.

References

Lane D. J. (2018). "A Robotic "Social Media" Controlled Observatory for Education and Research". *Robotic Telescope, Student Research and Education Proceedings*, **1:1**, 119–126. Proceedings articles stemming from the Robotic Telescopes, Student Research and Education Conference held in San Diego, California, USA from 18-22 June, 2017.

Minor Planet Center (2021). "MPEC 2021-S21 : DAILY ORBIT UPDATE (2021 September 17)".

Roggemans P. (1988). "The visual meteor database (VMDB)". *WGN, Journal of the IMO*, **16:6**, 179–186.

Handling Editor: Javor Kac

Status of the IAU Meteor Data Center

Regina Rudawska [1], Mária Hajduková [2], Tadeusz J. Jopek [3], Luboš Neslušan [4], Marián Jakubík [4], Ján Svoreň [4]

Since 2007, the Meteor Data Center (MDC) has had two components: the "Orbital database" (OD) and the "Shower database" (SD). The orbital part is in charge of the efficient collection, checking, and dissemination of geocentric parameters and orbits of individual orbits. It also acts as a central depository for meteoroid orbits obtained by different techniques: photographic, television, video, CCD and radar.
The shower database collects the geocentric and orbital parameters of the meteor showers and meteoroid streams. It is not an archive of all information related to meteor showers, its primary task is to give unique names and codes to new meteor showers (streams). The SD acts in conjunction with the Working Group on Meteor Shower Nomenclature of International Astronomical Union (IAU) Commission F1, "Meteors, Meteorites, and Interplanetary Dust".
In our paper, we give a concise description of the IAU MDC database, its origin, structure and, in particular, the current requirements for the introduction of new orbital and shower data.

Received 2021 October 26

This work has been presented at the International Meteor Conference 2021 (held online).

1 Introduction

The Meteor Data Centre (MDC)[a] was established at the General Assembly of the IAU held in 1982, in Patras, and at that time compiled only orbital data. In 2006, in Prague, Commission 22 of the IAU established a Task Group for Meteor Shower Nomenclature, (see Spurný et al., 2007). [b] In the following year, the meteor shower database was created as part of the IAU MDC, and two years later, in 2009, in Rio de Janeiro, for the first time in the history of meteor astronomy, 64 meteor showers were officially named by the GA IAU, (see Bowell et al., 2010; Watanabe et al., 2010; Jopek & Jenniskens, 2011). The official names of the subsequent 48 showers were approved at the GA IAU held in Beijing and Honolulu (see Jopek & Kaňuchová, 2014; Jopek & Kaňuchová, 2017).

Over the years, the structure of the MDC database and the rules of its management have changed, see Lindblad, 1987; Lindblad & Steel, 1994; Lindblad et al., 2003; Porubčan et al., 2011; Neslušan et al., 2014; Jenniskens et al., 2020.

In this work, the words meteoroid stream and meteor shower can be understood as synonyms. Their current definition adopted by the IAU is available in the work of Koschny & Borovička (2017).

[1]RHEA group/ESA ESTEC, The Netherlands
[2]Astronomical Institute of the Slovak Academy of Sciences, Bratislava, Slovak Republic
[3]Astronomical Observatory Institute, Faculty of Physics, A.M. University, Poznań, Poland
[4]Astronomical Institute of the Slovak Academy of Sciences, Tatranská Lomnica, Slovak Republic

IMO bibcode WGN-496-rudawska-iaumdc
NASA-ADS bibcode 2021JIMO...49..163R

[a]https://www.iaumeteordatacenter.org/
[b]In 2009 the Task Group was transformed into the Working Group on Meteor Shower Nomenclature.

Table 1 – IAU MDC orbital data status October 2021.

Catalogue/Source	Number of orbits
Photographic/various data	4 873
Video/CAMS	110 521
Video/SonotaCo	353 231
Radar/Hissar	8 916

In the current OD, each new sample of the orbits submitted is saved separately (though in a consistent form) and can also be downloaded separately. This rule has already been applied to all of the video orbits in the database. The orbital database consists of more than 450 000 orbits, see Table 1. The magnitude distributions of the meteors caused by the meteoroids with known orbital data are shown in Figure 1, separately for the meteors detected by photographic (a) and video (b) techniques (photographic meteors and video meteors, hereafter). In Figure 2, there are, furthermore, the orbital elements of the meteoroids observed by video technique. Only the Cameras for Allsky Meteor Surveillance (CAMS; Jenniskens et al., 2011; Jenniskens et al., 2016a; Jenniskens et al., 2016b; Jenniskens & Nénon, 2016) video meteors were included in the database at the time of plotting the graphs.

Table 2 – IAU MDC shower lists in October 2021.

Type of list	Number of showers
List of All Showers	917
List of Established Showers	112
Working List	781
List of Shower Groups	24
List of Removed Showers	44

Currently, the SD component contains over 900 meteor showers; their names are grouped in the form of five lists, see Table 2. The first list consists of the names of all unique showers actually registered in the database. 450 of them are represented by more than one set of parameters (so called solutions). The names of the showers already approved by the IAU are also listed separately in the List of Established Showers. The Working

List constitutes showers that have yet to be confirmed (by other authors or other data). The List of Meteor Shower Groups consists of groups/complexes that have been suggested in a scientific publication. In Figure 3 we plotted the radiants of the meteor showers from the Working and Established lists on the whole celestial sphere. As one can see, in the northern sphere of the ecliptic system, we have slightly more meteor radiants.

Removed showers remain in the MDC in a separate list. The list contains the names of showers that were previously on the Working List and were excluded from it for various, very individual reasons. The problem of removing unnecessary data from the Working List was discussed during the Meteoroids 2019 conference (Jenniskens et al., 2020). The Working List may include duplicates and data of very low statistical significance; for example, a shower (stream) identified by means of two orbits only. It was decided that any shower (stream) would be removed from the Working List if a work recommending such a decision was published. After a recommendation for removal, the MDC will move the shower to the List of Removed Showers and add a note giving the reason for the removal on the MDC Web site. Any removed shower can eventually return to the Working List after such a recommendation has been published. However, it should be noted that an incomplete record (e.g. no orbital data) is not a reason for removal, as long as the proposed shower is uniquely identified by the geocentric parameters.

2 How to submit new data

The current requirements for submission and the points of contact are on the website, listed separately for orbital and shower data.

2.1 New orbits of meteoroids

A new set of orbital data sent to the MDC has to be accompanied by a paper or papers, which should have been published in a peer reviewed journal before submission to the MDC. The paper(s) should provide a description of the observational facility used to detect the meteors and a description of the method of processing the observations, as well as the way of calculating the parameters presented. References to this paper(s) must be sent to the IAU MDC together with the data (it is assumed that the papers will be cited by users). If the authors send another set of data gained using the same observational equipment and the same method of data processing, the accompanying paper is not required.

For each meteor, the complete set of compulsory parameters must be given. The compulsory parameters are:

1. date of the meteor detection (in the form: year, month, day and fraction of day, giving the time of meteor detection in UT),
2. right ascension and declination of the geocentric radiant (in degrees),
3. geocentric and heliocentric velocities (in $\mathrm{km\,s^{-1}}$),
4. perihelion distance of meteor orbit (in AU),
5. its numerical eccentricity,
6. argument of perihelion (in degrees),
7. longitude of ascending node (in degrees), and
8. inclination (in degrees).

The angular parameters should be referred to the actual equinox of J2000.0. Ideally, at least some of these parameters should be given with their error limits.

Besides the compulsory parameters, the authors of new data on the meteors can also supply some of 22 additional parameters for every meteor. The list of 21 of those parameters currently accepted by the IAU MDC was published in a paper by Narziev et al. (2020), Table 1. The 22nd parameter, duration of meteor, was added recently, in the process of incorporating the SonotaCo data (SonotaCo, 2009; SonotaCo, 2016; SonotaCo et al., 2021).

Before the proper sending of new orbital data, the authors are requested to communicate the way of sending and format of the data with the MDC-OD team[c].

2.2 Delivery of meteor showers

Observers may send data for both unknown and well-known meteoroid streams to the SD. Data provided of a stream which already exist in the MDC will be used to confirm its real existence. Modern methods of identifying meteoroid streams do not guarantee that the results obtained were not obtained by chance.

The shower database is not an archive of all meteoroid information. It only stores those parameters that are necessary to determine whether we are dealing with a new stream or with a well-known stream. Hence the geocentric longitude of the Sun, the radiant coordinates, and geocentric velocity are required, as well as the heliocentric elements of the orbit. However, only the geocentric parameters are obligatory, while the orbital elements are very much appreciated. The basic planes of the reference system used in the MDC are the mean equator and the mean ecliptic of the epoch J2000. The moment of time of the shower activity is represented by the ecliptic longitude of the Sun. In brief, the data sent to the MDC may include:

1. Activity – the year of observed shower activity. If observed regularly - the word *annual* should be given.
2. S. Lon – the mean solar ecliptic longitude at the moment of observation of the members of the shower. (degrees, epoch J2000).
3. RA – mean geocentric right ascension of the shower radiant (degrees, epoch J2000).
4. DE – mean geocentric declination of the shower radiant (degrees, epoch J2000).
5. dRA – radiant drift in right ascension (not obligatory, degrees RA per degree of solar longitude, epoch J2000).

[c] mdc_orbits@ta3.sk

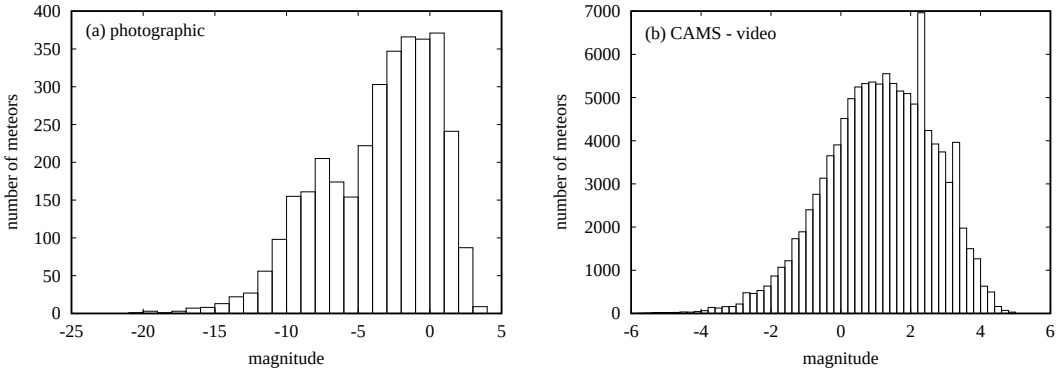

Figure 1 – The magnitude distribution of all photographic (panel a) and CAMS video (b) meteors. Eleven video meteors brighter than -6^m are out of the shown range.

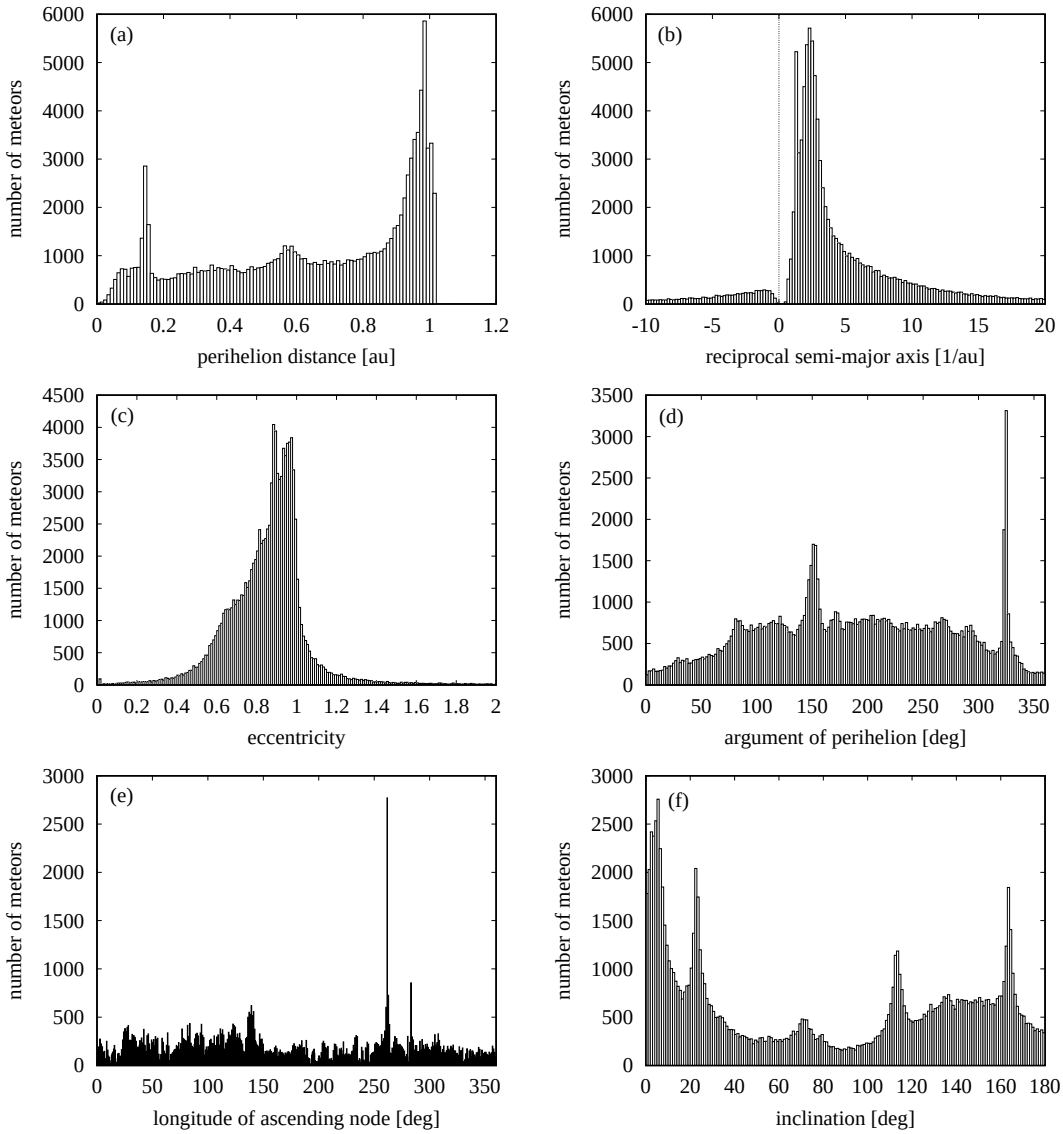

Figure 2 – The distributions of perihelion distance (panel a), reciprocal semi-major axis (b), eccentricity (c), argument of perihelion (d), longitude of ascending node (e), and inclination (f) of the video meteors in the CAMS MDC database.

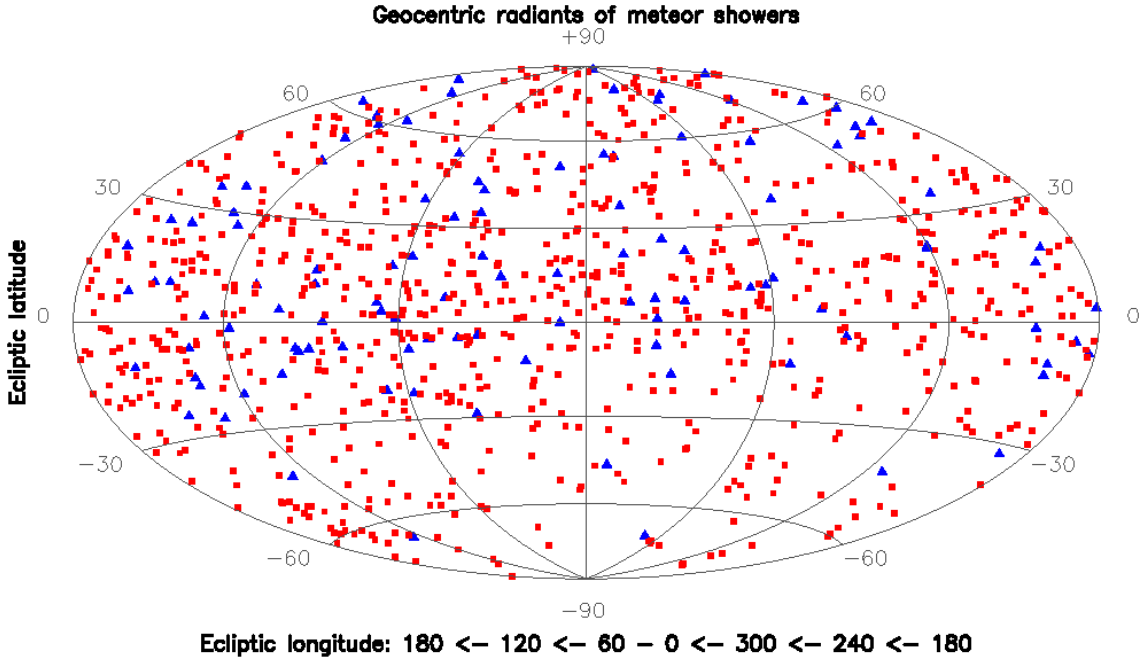

Figure 3 – Ecliptical coordinates of the mean radiants of the meteor showers in Aitoff-Hammer's projection. 781 radiants from the MDC working list are marked with red squares. 112 shower radiants from the Established list are marked with blue triangles.

6. dDE – radiant drift in declination (not obligatory, degrees DE per degree of solar longitude, epoch J2000).
7. VG – mean geocentric speed ($\mathrm{km\,s^{-1}}$).
8. a – mean semi-major axis (AU).
9. q – mean perihelion distance (AU).
10. e – mean eccentricity.
11. Peri – mean argument of perihelion (degrees, epoch J2000).
12. Node – mean longitude of ascending node (degrees, epoch J2000).
13. Incl – mean inclination of the orbital plane (degrees, epoch J2000).
14. N – number of meteors used to determine the mean radiant and orbit.
15. OT – code of the technique used for the meteor shower observation: P – photo, R – radar, T – TV, video, C – CCD, V – visual.
16. Information where the submitted meteor data will be published.
17. Also, the author may propose unique name of the submitted shower, as well as its unique 3-letter code.

All meteoroid data should be sent to the MDC as an ASCII file, according to the template available on the MDC website. Next, the MDC verifies the correctness of the proposed stream name and 3 letter code. If necessary, the MDC determines the correct name and code. From this moment, within 6 months, using the obtained shower name and code, the author should publish a paper describing his/her submission. Publications in any peer-reviewed scientific journal are accepted, but also in amateur journals such as WGN or MeteorNews.

As the mean values of the meteoroid parameters, most authors give the arithmetic means of the corresponding parameters of the stream members. Other authors provide median values of the individual parameters. However, both such approaches do not guarantee consistency between the given parameters, e.g. the mean value of the semi-major axis is usually not equal to the semi-axis calculated using arithmetic means or medians of eccentricity and perihelion distance. This means that the mean values of the orbital elements reported in the MDC do not represent the orbit of a meteoroid stream in terms of celestial mechanics.

On the MDC website, there are templates of two files: the shower mean data [d] and the Look-up table [e], which the user must complete and submit to the MDC. The first file contains mean parameters describing the submitted shower and which are included in the kernel of the shower database. The second file, the so-called 'Look-up table', contains the data of individual meteoroids, the members of a given stream. These are members of the stream, the data of which were used to determine the average values of the stream parameters. The content of the Look-up table was established at the Meteoroids 2019 conference, (see Jenniskens et al., 2020) during the business meeting of the Working Group on Meteor Shower Nomenclature (IAU Commission F1: Meteors, Meteorites, and Interplanetary Dust).

[d] https://www.ta3.sk/IAUC22DB/MDC2007/Etc/streamMDC-Template.txt
[e] https://www.ta3.sk/IAUC22DB/MDC2007/Etc/streamLT-Template.csv

Each Look-up table must contain the following information for each meteor on which the new identification is based:

1. CurNum – current number of the meteor in the Look-up table.
2. SolLon – ecliptic longitude of Sun at the meteor instant (degrees, J2000).
3. SCELoG – Sun centered ecliptic longitude of the geocentric radiant (degrees).
4. ELaG – ecliptic latitude of the geocentric radiant (degrees, J2000).
5. VG – geocentric velocity [$\mathrm{km\,s^{-1}}$].
6. IAUNo – IAU numerical code of the shower.
7. IAUCod – IAU 3 letter code of the shower, (not obligatory).
8. CatCod – code of the source catalogue of the meteor, (not obligatory).
9. MetCod – meteor code given in the source catalogue, (not obligatory).

More details on the required data format of the Look-up table records are given in the template on the MDC website.

The Look-up tables provided to the MDC will allow a more complete insight into the meteoroid streams submitted to the database. They contain information about shower duration, as well as radiant and speed dispersion. The MDC user, by comparing the contents of the tables, will therefore be able to assess whether an identified 'new' stream is already in the MDC.

3 Conclusions

As a result of the changes in the mode of operation of the MDC shower base, more than 40 streams were moved to the List of Removed Showers or added as another solution of a previously known stream. These were mostly duplicates. We are convinced that the introduced changes, a critical assessment of the database content and the way it functions, have led to an improvement in the quality of data contained in the SD, and make the lists more valuable for users.

It will be recalled that before publishing, each new meteoroid stream must receive a unique name, the IAU numeric and 3-letter code from the MDC. Moreover, each new entry to the MDC must be published in a scientific journal or meteor amateur journal like WGN (the Journal of the IMO) or MeteorNews. In order to avoid permanent deletion from the MDC, the published manuscript describing the study must be sent to the MDC within half a year of requesting the shower names and codes. Each new submission to the MDC should be accompanied by the corresponding "Lookup table" that gives the shower members' parameters.

Concerning the OD component of the MDC database, its video part will be upgraded in a near future; specifically, version 2 of the CAMS data will be replaced by version 3. Altogether, the new version of the CAMS data contains 471 577 video meteors.

The MDC database is not perfect. It still contains incorrect data: mistakes and errors, inconsistent values of the parameters, missing information about the data source etc. Furthermore, the functionality of the database could be improved. Hence, we appreciate every critical remark related to the content and the operation of the MDC.

Acknowledgments

The authors like to acknowledge: Rainer Arlt, David Asher, Rhiannon Blaauw, Steve Hutcheon, Sirko Molau, Ned Smith, Francisco Ocaña, Željko Andreić, Damir Šegon, Denis Vida, Allan Mulof, Paul Roggemans, Galina Ryabova, Masahiro Koseki, Alfredo Dal'Ava Júnior, Mikiya Sato, Diego Janches, Jiří Borovička, Zuzana Kaňuchová, Ivan Sergey and Peter Jenniskens who in recent years helped improve the IAU MDC contents.

This research has made use of NASA's Astrophysics Data System Bibliographic Services.

References

Bowell E. L. G., Meech K. J., Williams I. P., Boss A., Courtin R., Gustafson B. Å. S., Levasseur-Regourd A.-C., Mayor M., Spurný P., Watanabe J., Consolmagno G. J., Fernández J. A., Huebner W. F., Marov M. Y., Schulz R. M., Valsecchi G. B., and Witt A. N. (2010). "Division III: Planetary Systems Science". *Transactions of the International Astronomical Union, Series B*, **6:T27**, 158–167.

Jenniskens P., Gural P. S., Dynneson L., Grigsby B. J., Newman K. E., Borden M., Koop M., and Holman D. (2011). "CAMS: Cameras for Allsky Meteor Surveillance to establish minor meteor showers". *Icarus*, **216**, 40–61.

Jenniskens P., Jopek T. J., Janches D., Hajduková M., Kokhirova G. I., and Rudawska R. (2020). "On removing showers from the IAU Working List of Meteor Showers". *Planetary Space Science*, **182**, 104821.

Jenniskens P. and Nénon Q. (2016). "CAMS verification of single-linked high-threshold D-criterion detected meteor showers". *Icarus*, **266**, 371–383.

Jenniskens P., Nénon Q., Gural P. S., Albers J., Haberman B., Johnson B., Holman D., Morales R., Grigsby B. J., Samuels D., and Johannink C. (2016a). "CAMS confirmation of previously reported meteor showers". *Icarus*, **266**, 355–370.

Jenniskens P., Nénon Q., Gural P. S., Albers J., Haberman B., Johnson B., Morales R., Grigsby B. J., Samuels D., and Johannink C. (2016b). "CAMS newly detected meteor showers and the sporadic background". *Icarus*, **266**, 384–409.

Jopek T. J. and Jenniskens P. M. (2011). "The Working Group on Meteor Showers Nomenclature: A History, Current Status and a Call for Contributions". In Cooke W. J., Moser D. E., Hardin B. F.,

and Janches D., editors, *Meteoroids: The Smallest Solar System Bodies*. pages 7–13.

Jopek T. J. and Kaňuchová Z. (2014). "Current status of the IAU MDC Meteor Showers Database". In Jopek T. J., Rietmeijer F. J. M., Watanabe J., and Williams I. P., editors, *Meteoroids 2013*. pages 353–364.

Jopek T. J. and Kaňuchová Z. (2017). "IAU Meteor Data Center-the shower database: A status report". *Planetary Space Science*, **143**, 3–6.

Koschny D. and Borovička J. (2017). "Definitions of terms in meteor astronomy". *WGN, Journal of the International Meteor Organization*, **45:5**, 91–92.

Lindblad B. A. (1987). "The IAU Meteor Data Center in Lund.". *Publications of the Astronomical Institute of the Czechoslovak Academy of Sciences*, **67**, 201–204.

Lindblad B. A., Neslušan L., Porubčan V., and Svoreň J. (2003). "IAU Meteor Database of photographic orbits version 2003". *Earth Moon and Planets*, **93:4**, 249–260.

Lindblad B. A. and Steel D. I. (1994). "Meteoroid Orbits Available from the IAU Meteor Data Center". In Milani A., di Martino M., and Cellino A., editors, *Asteroids, Comets, Meteors 1993*, volume 160. page 497.

Narziev M., Chebotarev R. P., Jopek T. J., Neslušan L., Porubčan V., Svoreň J., Khujanazarov H. F., Bibarsov R. S., Irkaeva S. N., Isomutdinov S. O., Kolmakov V. N., Polushkin G. A., and Sidorin V. N. (2020). "IAU MDC meteor orbits database - A sample of radio-meteor data from the Hissar Observatory". *Planetary and Space Science*, **192**, 105008.

Neslušan L., Porubčan V., and Svoreň J. (2014). "IAU MDC Photographic Meteor Orbits Database: Version 2013". *Earth Moon and Planets*, **111:3-4**, 105–114.

Porubčan V., Svoreň J., Neslušan L., and Schunová E. (2011). "The Updated IAU MDC Catalogue of Photographic Meteor Orbits". In Cooke W. J., Moser D. E., Hardin B. F., and Janches D., editors, *Meteoroids: The Smallest Solar System Bodies*. page 338.

SonotaCo (2009). "A meteor shower catalog based on video observations in 2007-2008". *WGN, Journal of the International Meteor Organization*, **37**, 55–62.

SonotaCo (2016). "Observation error propagation on video meteor orbit determination". *WGN, Journal of the International Meteor Organization*, **44**, 42–45.

SonotaCo, Masuzawa T., Sekiguchi T., Miyoshi T., Fujiwara Y., Maeda K., and Uehara S. (2021). "Ongoing Meteor Work. SNMv3: A Meteor Data Set for Meteor Shower Analysis". *WGN, Journal of the International Meteor Organization*, **49**, 64–70.

Spurný P., Watanabe J., Mann I., Baggaley W. J., Borovička J., Brown P. G., Consolmagno G. J., Jenniskens P., Pellinen-Wannberg A. K., Porubčan V., Williams I. P., and Yano H. (2007). "Commission 22: Meteors, Meteorites and Interplanetary Dust". *Transactions of the International Astronomical Union, Series B*, **3:26B**, 140–141.

Watanabe J., Jenniskens P., Spurný P., Borovička J., Campbell-Brown M., Consolmagno G., Jopek T., Vaubaillon J., Williams I. P., and Zhu J. (2010). "Commission 22: Meters, Meteorites and Interplanetary Dust". *Transactions of the International Astronomical Union, Series B*, **6:T27**, 177–179.

Handling Editors: Jürgen Rendtel
This paper has been typeset from a LaTeX file prepared by the authors.

Meteor showers: from D-criteria to a chaos map

A. Courtot[1,2], *J. Vaubaillon*[1], *M. Fouchard*[1]

Nowadays meteor showers are often established using orbit dissimilarity criteria. However, they are not as reliable as first hoped. For example, the widely used D_{SH} criterion (Southworth and Hawkins, 1963) exhibits mathematical, physical and statistical problems. Furthermore, many physically sound criteria would benefit from more thorough robustness tests. Instead of defining a new criterion, a new tool is proposed here to add information regarding the existence of a meteor shower: a chaos map. The utility of this tool will be shown, along with some first results on the stability of meteoroids streams, linked with established meteor showers.

Received 2021 October 18

This work has been presented at the International Meteor Conference 2021 (held online).

1 Meteor shower and meteor group

The term "meteor shower" is used to talk about a set of meteors coming from a single parent body, through a meteoroid stream. Today there are almost 1000[a] meteor showers listed by the IAU, which would mean a comparably large number of parent bodies in the vicinity of the Earth in the near past (1–100 kyrs). This casts a doubt on methods used to find new meteor showers.

Here we will consider methods which try to find a new meteor shower using data based on observations from Earth. It is possible to model a meteor shower from a parent body and then try to see if the meteors have been observed, but this aspect will not be examined here.

Such methods usually consist in 3 steps:

1. calculating the radiant of the meteors studied and computing their orbits,
2. verifying how similar they are (using orbit dissimilarity criteria), and
3. trying to find the parent body. This is optional, as it may have been destroyed in the past.

It can be noted that orbit dissimilarity criteria use either orbital elements or directly radiant and geocentric velocity, as it will be discussed in Section 2. Other methods make this comparison without a criteria, but they will not be the focus of this study.

The methods described have a big drawback: several meteoroids may end up on similar orbits by chance. Therefore these 3 first steps are not enough to prove that the meteors studied are in fact part of the same meteor shower. In order to distinguish between those different objects, we will call "meteor group" a set of meteors, which share the same radiant and similar orbits. It then becomes necessary to prove that a meteor group comes from a single parent body in order to prove that the meteors studied are in fact part of a meteor shower.

Some authors (e.g. Koten et al. (2014), Šegon et al. (2017)) go further in the search for meteor showers by applying some analysis on meteor groups. First, a statistical comparison between random meteors grouped together and actual meteor groups (as defined above) provides insight into the validity of the meteor group studied. Secondly, an orbital analysis is often possible by following meteoroids ejected from the suspected parent body until they meet with the Earth orbit, at which point the resulting shower can be compared with the meteors actually observed. Finally, when such quantities are available, the age and composition of the meteors studied can strengthen the validity of the supposed meteor shower.

Those analysis are not always presented in the articles that seek to demonstrate the validity of a newly-discovered meteor shower, although the statistical analysis at least would strengthen the claim, in our opinion.

2 Orbit dissimilarity criteria

As seen in the previous section, the constitution of meteor groups is at the heart of the search for meteor showers, and so is the orbit dissimilarity criteria (D-criteria).

One of the most widely-known criteria, the first criterion introduced, has been written by Southworth & Hawkins (1963) and compares the orbital elements of two different meteoroids (indices 1 and 2). For small inclination, we have:

$$\begin{aligned} D_{SH}^2 = {} & (e_2 - e_1)^2 + (q_2 - q_1)^2 + \left(2 \sin \frac{i_2 - i_1}{2}\right)^2 \\ & + \sin i_1 \sin i_2 \left(2 \sin \frac{\Omega_1 - \Omega_2}{2}\right)^2 \\ & + \left(2 \frac{e_2 - e_1}{2} \sin \frac{\Omega_2 + \omega_2 - \Omega_1 - \omega_1}{2}\right)^2, \end{aligned} \tag{1}$$

with e the eccentricity, q the perihelion distance, i the inclination, Ω the longitude of ascending node and ω the longitude of perihelion.

Several critics have been made against this criterion. Only a few will be presented here. Steel et al. (1991), for example, note that this criterion compares the longitudes of ascending node of the meteoroids. However,

[1]IMCCE, Observatoire de Paris, PSL Research University, CNRS, Sorbonne Universités, UPMC Univ. Paris 06, Univ. Lille., France.
[2]Email: ariane.courtot@obspm.fr

IMO bibcode WGN-496-courtot-chaos
NASA-ADS bibcode 2021JIMO...49..169C

[a]917 on October 11th, 2021, according to IAU MDC

meteor showers can last long enough to make this quantity vary greatly between the first meteor and the last of the shower (e.g. Taurids). This criterion is thus ill-suited to find long-lasting meteor showers.

Valsecchi et al. (1999) show that the orbit similarity problem, in the case of meteors, has only 4 dimensions (the necessary crossing of the meteoroid orbits with the Earth adds one constraint), but the D_{SH} has 5 dimensions.

Southworth & Hawkins (1963) themselves analyze their criterion on a statistical level and find that about half of the meteor groups formed with their criterion could also have been formed randomly. In other words, only half of those meteor groups have a statistical significance.

Finally, one last critic justifies on its own the end of the use of the D_{SH}: Drummond (1981) shows the first term has no dimension (eccentricity) whereas the second one has a length square dimension (perihelion distance) (see Equation (1)). No possible unit can be applied to this criterion, making it a nonsense.

However, 11 different criteria at least can be found in the literature. It seems thus better to use one of those, instead of the D_{SH}, in order to define meteor groups.

Drummond (1981) and Jopek (1993) both propose criteria derivating from the D_{SH}, while also trying to correct some of its mistakes (the unit problem, for example). After that, the authors, with the exception of Steel et al. (1991), propose criteria based on new ideas. Valsecchi et al. (1999) criteria are based on observed elements, like the geocentric speed of the meteors. Neslusan (2002) and Jopek et al. (2008) use a different set of orbital variables, such as orbital momentum per mass or orbital energy. Jenniskens (2008) goes back to the use of orbital elements, but the reasoning behind his criteria is completely different from the D_{SH}. Other criteria have been proposed, such as the criterion from Rudawska et al. (2015), but this short list gives an idea of alternate criteria to use in the search for meteor showers.

However, those articles usually do not present a statistical or a dynamical analysis (sometimes one, never both), which undermines their relevance. An extensive study on each of those criteria would be necessary in order to quantify the significance of meteor groups formed with such criteria.

3 A new tool: chaos map

In order to answer the question "how likely is it that this specific meteor group is actually a meteor shower, i.e. is composed of meteors coming from the same parent body?", a new tool is proposed to the meteor community. The goal of a chaos map is to evaluate quickly the stability of a meteoroid stream, which will give an insight into its evolution. An example of what a chaos map can look like can be found in Frouard et al. (2011), although the authors study some Jupiter satellites, and with a different indicator. The final result will allow the user to find the chaoticity of the stream, using only the orbital elements of the meteors studied.

This kind of map can be used in multiple scenarios. Let's imagine for example that we come across several meteors sharing a very well-defined radiant. We compute their orbits and find that the meteoroids they come from have very similar orbits (according to relevant D-criteria). In other words, we have found a very well-defined meteoroid stream. We are now trying to see whether it comes from a unique parent body. The chaos map then tells us that this stream is in a very chaotic region. If this stream is coming from the same object, it has to be very young. It would have been scattered otherwise. So the meteor group we observe has to be very young too. This can be checked thanks to older observations, dynamical analysis or analysis of the duration of the meteor group. If this group is as young as expected, we have another argument to prove that this group is a meteor shower. If it is not, it means that this group should not be considered a meteor shower.

Of course, we may find ourselves in grey areas where the answers to such questions can only be given in terms of probability. But this will allow us to determine the likeliness of a meteor shower existence.

Furthermore, the meteoroid orbits are chaotic by nature, so the questions will not be about whether or not they are stable, but how chaotic they are, when this chaos appears and why.

The Fast Lyapunov Indicator (FLI) described in Froeschlé et al. (1997) is our first choice to measure the chaos. Although it does not give an absolute value of chaos, the relative measure is enough in the context of a map. This indicator is also very useful to follow the variation of the chaos over time, which is of particular interest to understand the evolution of meteoroid streams.

To our knowledge, the FLI has never been used with non-gravitational forces (NGF), which play an important part in the evolution of meteoroids. This will be our biggest challenge in the making of the chaos map.

Our code is based on the Radau algorithm from Everhart (1985) and uses a modified FLI taking into account the NGF. Figure 1 uses the first result of this code, where we have computed the evolution of 1000 particles over 500 years. The initial conditions of those particles are consistent with the Geminid meteor shower. In less than 100 years, the FLI reaches its value, which stays constant over the rest of the 500 years of integration. So the chaos of the Geminids takes longer than 500 years to appear, which was expected (they seem stable over this period of time, see Ryabova et al. (2019)). Some bumps in the curves show small rise in chaoticity, due to close encounters with the Earth. This happens for about 30% of all the particles computed.

This result shows that our code is working well, at least without NGF (the particles chosen were big enough to lessen the influence of NGF).

4 Conclusion and future works

Calling "meteor group" several meteors coming from the same radiant and showing similar orbits, highlights the difference between such a group and a meteor

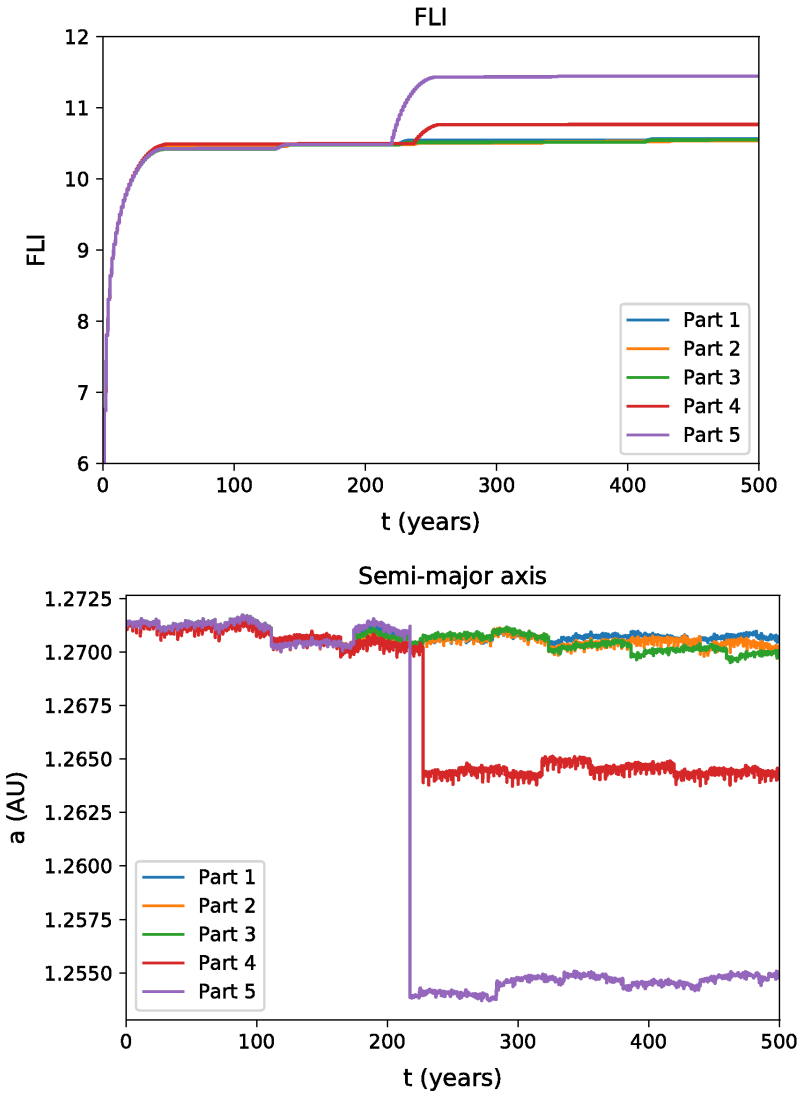

Figure 1 – FLI and semi-major axis a computed over 500 years for 5 of the 1000 particles modeled from the Geminid shower. The FLI is relative: we are interested in its evolution. The bumps in chaoticity for parts 4 and 5 can be linked with close encounters with the Earth, visible in the evolution of the semi-major axis.

shower, as the meteors may not all come from the same parent body. In order to prove the existence of a specific meteor shower, we need to investigate the relevance of the meteor group studied. This cannot be done without statistical and dynamical analysis of the tools used to form the meteor group: the D-criteria. Clearly the widely-known D_{SH} cannot be used anymore, but many others are available in the literature and should be studied in details.

Other tools can be added in the search for meteor showers, such as a chaos map, which will give new information about meteoroid streams and their evolution. Whereas the map itself is not done yet, the general structure of the code used is functional and is enough to investigate the chaoticity of the dm-sized Geminids over 500 years.

In the future, we will need to determine which orbital elements could be useful for the map. Some solutions are already envisioned for the NGF problem; they will be implemented in the near future.

Acknowledgments

Ariane Courtot acknowledges support from the École Doctorale d' Astronomie et d' Astrophysique d'Île-de-France (ED127).

References

Drummond J. D. (1981). "A test of comet and meteor shower associations". *Icarus*, **45:3**, 545–553.

Everhart E. (1985). "An efficient integrator that uses Gauss-Radau spacings". In Carusi A. and Valsecchi G. B., editors, *IAU Colloq. 83: Dynamics of Comets: Their Origin and Evolution*, volume 115. page 185.

Froeschlé C., Lega E., and Gonczi R. (1997). "Fast Lyapunov Indicators. Application to Asteroidal Motion". *Celestial Mechanics and Dynamical Astronomy*, **67:1**, 41–62.

Frouard J., Vienne A., and Fouchard M. (2011). "The long-term dynamics of the Jovian irregular satellites". *Astronomy and Astrophysics*, **532**, A44.

Jenniskens P. (2008). "Meteoroid streams that trace to candidate dormant comets". *Icarus*, **194:1**, 13–22.

Jopek T. J. (1993). "Remarks on the Meteor Orbital Similarity D-Criterion". *Icarus*, **106:2**, 603–607.

Jopek T. J., Rudawska R., and Bartczak P. (2008). "Meteoroid Stream Searching: The Use of the Vectorial Elements". *Earth Moon and Planets*, **102:1-4**, 73–78.

Koten P., Vaubaillon J., Čapek D., Vojáček V., Spurný P., Štork R., and Colas F. (2014). "Search for faint meteors on the orbits of Příbram and Neuschwanstein meteorites". *Icarus*, **239**, 244–252.

Neslusan L. (2002). "A Sketch of an Orbital-Momentum-Based Criterion of Diversity of Two Keplerian Orbits". In Pretka-Ziomek H., Wnuk E., Seidelmann P. K., and Richardson D., editors, *Dynamics of Natural and Artificial Celestial Bodies*, volume 81. pages 365–366.

Rudawska R., Matlovič P., Tóth J., and Kornoš L. (2015). "Independent identification of meteor showers in EDMOND database". *Planetary and Space Science*, **118**, 38–47.

Ryabova G. O., Avdyushev V. A., and Williams I. P. (2019). "Asteroid (3200) Phaethon and the Geminid meteoroid stream complex". *MNRAS*, **485:3**, 3378–3385.

Šegon D., Vaubaillon J., Gural P. S., Vida D., Andreić Ž., Korlević K., and Skokić I. (2017). "Dynamical modeling validation of parent bodies associated with newly discovered CMN meteor showers". *Astronomy and Astrophysics*, **598**, A15.

Southworth R. B. and Hawkins G. S. (1963). "Statistics of meteor streams". *Smithsonian Contributions to Astrophysics*, **7**, 261–285.

Steel D. I., Asher D. J., and Clube S. V. M. (1991). "The structure and evolution of the Taurid complex". *Monthly Notices of the Royal Astronomical Society*, **251**, 632–648.

Valsecchi G. B., Jopek T. J., and Froeschle C. (1999). "Meteoroid stream identification: a new approach - I. Theory". *Monthly Notices of the Royal Astronomical Society*, **304:4**, 743–750.

Handling Editor: Javor Kac

This paper has been typeset from a LaTeX file prepared by the authors.

Meteor observation with the DIMS project: sensor calibration and first results

D. Barghini[1,2], S. Valenti[1], S. Abe[3], M. Arahori[4], M.E. Bertaina[1], M. Casolino[5,6], A. Cellino[2], C. Covault[7], T. Ebisuzaki[5], M. Endo[3], M. Fujioka[8], Y. Fujiwara[9], D. Gardiol[2], M. Hajdukova[10], M. Hasegawa[3], R. Ide[4], Y. Iwami[8], F. Kajino[4], M. Kasztelan[11], K. Kikuchi[3], S.-W. Kim[12], M. Kojro[13], J.N. Matthews[14], K. Nadamoto[4], I.H. Park[15], L.W. Piotrowski[16], M. Przybylak[11], H. Sagawa[17], K. Shinozaki[11], D. Shinto[8], J.S. Sidhu[7], G. Starkman[7], S. Tada[4], Y. Takizawa[5], Y. Tameda[8], M. Vrabel[11] (DIMS Collaboration)

In addition to meteors coming from the Solar System, fast- and straight-moving luminous events of exotic origin could theoretically be observed in the Earth's atmosphere at night. For example, *nuclearites* are strange quark matter nuggets that are hypothesized as possible candidates of macroscopic dark matter. If they exist, they should collide with the atmosphere and generate luminous events similar to meteors. However, they could be recognizable mainly by their lower altitude from the ground ($\sim$ 10 km) and their very high expected speed ($\sim$ 250 km/s). Also for meteoroids of interstellar origin, the boundary value of 72 km/s may be exceeded but only by several kilometers per second. The DIMS (Dark matter and Interstellar Meteoroid Study) experiment was born in 2017 aiming to search for fast-moving objects by observing the sky with wide-field and high-sensitivity CMOS cameras. The DIMS collaboration carried out several observational campaigns, mainly from Japan and at the Telescope Array site in Utah, to test and develop the system and observed few thousands of meteors. We derived the calibration of the DIMS sensors by astrometry and photometry techniques applied to observed stars in the field of view (57° × 34°) and assessed the achieved positional precision and sensitivity levels. DIMS cameras observe in a wide bandpass (300–1000 nm) and we estimated a limiting magnitude for meteors of about +6. By triangulation between two DIMS cameras, we derived the dynamics of observed events from our observational campaigns. At present time, none of the analyzed events shows indisputable features indicating non-meteor origin. In this paper, we will present the current status of this work.

Received 2021 November 4

This work has been presented at the International Meteor Conference 2021 (held online).

1 Introduction

The observation of luminous and fast-moving events in the night sky is typically ascribed to the impact of meteoroids on the Earth's atmosphere, *i.e.*, the meteor phenomenon. Nevertheless, meteor-like events could originate from other exotic sources and might be mistaken for meteors. For example, in the wide landscape of dark matter (DM) candidates, it is hypothesized that macroscopic strange quark matter (SQM) nuggets may collide with the atmosphere and generate luminous events similar to meteors. These hypothetical objects were firstly named *nuclearites* (De Rujula & Glashow, 1984) and are now included in a broader class of macroscopic DM candidates named *macros* (Jacobs et al., 2015). If they exist, their light emission within the atmosphere should be distinguishable from meteors thanks to their peculiar characteristics such as very low altitude and very high speed. In addition, also interstellar meteoroids may exceed the speed limit of Solar System's meteors. The DIMS (Dark matter and Interstellar Meteoroid Study) project was born in 2017 to develop an experiment that could detect such fast-moving events, by observing the night sky with wide-field and high-sensitivity CMOS cameras.

A first description of the analysis presented here can be found in Barghini et al. (2021). In this paper, we give a deeper focus on the sensor calibration and the meteor analysis techniques implemented and tested against data from one observational night on 1st September 2019 with two DIMS cameras installed at the Telescope Array site (Utah, USA). We discuss in Section 2 the observational features of nuclearite events, and in Section 3 we give a short overview about the DIMS project. Section 4 describes the data analysis procedures, and in particular the astrometric and pho-

[1]University of Turin, Physics Department, Italy. dario.barghini@edu.unito.it
[2]Astrophysical Observatory of Turin – National Institute for Astrophysics (INAF), Italy.
[3]Nihon University, Dept of Aerospace Engineering, Japan.
[4]Konan University, Department of Physics, Japan.
[5]RIKEN (Inst. of Physical and Chemical Research), Japan.
[6]National Institute for Nuclear Physics (INFN) – Rome Tor Vergata, Italy.
[7]Case Western Reserve University, Dept of Physics, USA.
[8]Osaka Electro-Communication University (OECU), Department of Engineering and Science, Japan.
[9]Nippon Meteor Society (NMS), Japan.
[10]Astronomical Institute of Slovak Academy of Sciences, Slovakia.
[11]National Centre for Nuclear Research (NCBJ), Poland.
[12]Korea Astronomy and Space Science Institute (KASI), Republic of Korea.
[13]University of Lodz, Faculty of Physics and Applied Informatics, Poland.
[14]University of Utah, Dept of Physics and Astronomy, USA.
[15]Sungkyunkwan University, Department of Physics, Republic of Korea.
[16]University of Warsaw, Faculty of Physics, Poland.
[17]University of Tokyo, Inst. for Cosmic Ray Research, Japan.

IMO bibcode WGN-496-barghini-dims
NASA-ADS bibcode 2021JIMO...49..173B

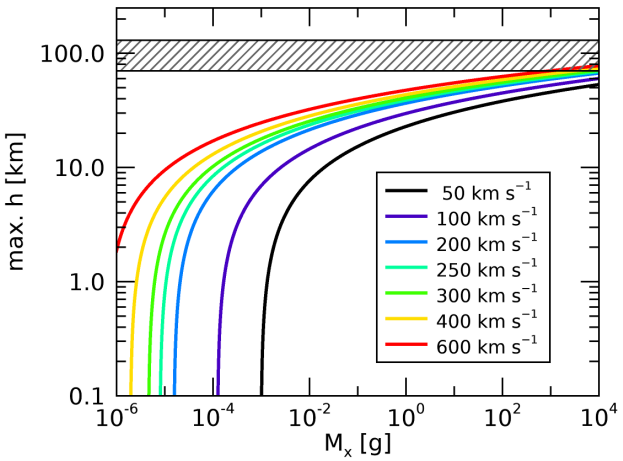

Figure 1 – Maximum height of light emission for a nuclearite traversing the Earth's atmosphere, as a function of the nuclearite mass and for different velocities within 50 and 600 km/s according to Eq 2. The grey dashed region marks the altitude range in which meteors typically occur (from 70 to 130 km).

tometric calibration of DIMS cameras and the meteor analysis pipeline. In Section 5 we present and discuss the results of this analysis, and Section 6 gives our state-of-the-art conclusions.

2 Observational features of nuclearites

The idea of nuclearites as macroscopic DM candidate arose from the consideration that SQM, in the form of macroscopic aggregates of up, down and strange quarks, might be more stable than ordinary matter (Witten, 1984). Soon thereafter, De Rujula & Glashow (1984) developed the theoretical description of the impact of these SQM macroscopic nuggets within the Earth's atmosphere, since they are expected to generate such impacts if they exist. In their hypothesis, the nuclearite is surrounded by an electron cloud, preserving the overall neutrality, and possesses a nuclear density of $\rho_N = 3.6 \cdot 10^{14}$ g/cm^3. When traversing the atmosphere, it loses energy via quasi-elastic collisions with the air molecules and generates an expanding thermal cylindrical shock wave, with the subsequent emission of black-body radiation. This light emission mechanism is considerably different from what happens to a meteoroid, which sublimates when entering the atmosphere and emits light due to the de-excitation of ionized elements, in addition to black-body radiation. Therefore, the apparent visual magnitude m of a nuclearite event can be given as:

$$m = 0.80 - 1.67 \log_{10}\left(\frac{M_x}{1\ \mathrm{g}}\right) + 5 \log_{10}\left(\frac{h}{10\ \mathrm{km}}\right) + - 7.5 \log_{10}\left(\frac{v}{250\ \mathrm{km\ s^{-1}}}\right) , \quad (1)$$

where M_x, v and h are the nuclearite mass, velocity and altitude from the ground. The impact speed of nuclearites should be of about 250 km/s, that is the typical rotation speed of the Galaxy and does not consider the Earth motion. However, it has been suggested that nuclearites may travel as fast as 550 km/s, *i.e*, the escape limit from the Galaxy at the Sun's position, while a lower speed within the allowed range for Solar System meteors (11–72 km/s) is not to be excluded a priori. Therefore, the limiting magnitude of the deployed instrument identifies some limits on mass and speed values for such objects to be observed. For example, nuclearites moving at $v > 400$ km/s would be detectable by DIMS cameras even with a mass of 0.1 mg, close to the local dark matter flux limit (see Section 5).

The light emission from a nuclearite is expected to be almost constant within its whole flight in the atmosphere, so that the apparent magnitude should change only as a function of the distance from the observer. This is one of the main features that should enable to discern between nuclearites and meteors, the latter having a much larger intrinsic variability in terms of lightcurve morphology due to their complex physical evolution while crossing the atmosphere. Moreover, the maximal height at which a nuclearite is supposed to generate light, according to this formulation, can be computed as:

$$\frac{h_{max}}{1\ \mathrm{km}} = 3.3 \left[\ln\left(\frac{M_x}{1\ \mathrm{g}}\right) + 3 \ln\left(\frac{v}{250\ \mathrm{km\ s^{-1}}}\right)\right] + 38.8\ . \quad (2)$$

From this result, we can see that the height of light emission for a nuclearite event should be much lower than the typical range for meteors (70–130 km). For $M_x < 1$ g it is confined below 40 km and reaches 70 km only for very massive nuclearites ($M_x > 1$ kg). This is shown in Figure 1, that plots h_{max} according to Equation 2 as a function of the nuclearite's mass and for different impact speed values. In any case, the most remarkable feature of events generated by nuclearites, in opposition to meteors, is that they may move upwards within the Earth's atmosphere. As a matter of fact, a massive nuclearite should be able to pierce through the Earth's diameter and emerge from the ground. This fascinating scenario would be an indisputable proof of the non-meteor origin of the observed event. On the contrary, very light nuclearites ($M_x < 0.3$ ng) would be able to reach the Earth's crust and accumulate therein.

In recent years, a different model was proposed to describe the phenomenology caused by a macro traversing the atmosphere (Sidhu et al., 2019). In this case, the passage of the macro within a dense medium is thought to create a hot plasma channel, which expands by heat diffusion. The hypothesis of nuclear density is also relaxed, by considering an arbitrary density ρ. According to this model, the expected visual magnitude is given as:

$$m = 39.7 - 5 \log_{10}\left(\frac{M_x}{1\ \mathrm{g}}\right) + 5 \log_{10}\left(\frac{h}{10\ \mathrm{km}}\right) + + 5 \log_{10}\left(\frac{\rho_N}{\rho}\right) + \frac{1}{\ln 10}\left(\frac{h}{1\ \mathrm{km}}\right) . \quad (3)$$

The comparison between Equations 1 and 3 poses some serious questions about the possibility of observing this class of events within the Earth's atmosphere.

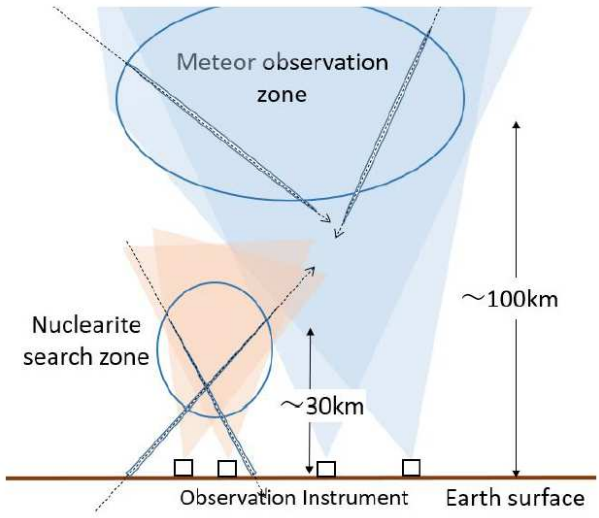

Figure 2 – The observational concept of DIMS. Since nuclearites are expected to emit light at a lower altitude range ($\lesssim$ 40 km), the stations for stereoscopic observation are positioned closer from each other (10–30 km), with respect to the usual meteor observational strategy.

It can be seen that a 1-gram macro, with nuclear density and at 10 km altitude, would shine at an apparent magnitude of +0.8 according to Equation 1, and at a completely undetectable magnitude of +44 according to Equation 3. This latter scenario would mean that such events should produce a signal way too dim to be detected by any kind of ground-based detector, but in the case of very massive objects or much below the nuclear density.

3 The DIMS project

The DIMS project was born in 2017 with the main focus of investigating macros and interstellar meteoroids flux at the Earth. A description of the project and first preliminary results are given in Kajino et al. (2017, 2019) and Abe et al. (2021). To observe such faint and fast-moving events, the DIMS project is developing and deploying multiple high-sensitivity and wide field of view (FoV) camera modules. Each module mainly consists of a Canon ME20F-SH monochrome camera, a computer to control the camera and a solar power supply and environmental control system (Shinto et al., 2021). The camera is equipped with Canon EF 35mm, f/1.4L lenses and a 1920 × 1080 pixels high-sensitivity CMOS sensor and can be operated at a 30 or 60 Hz frame rate. This system is installed in a stainless steel box with an acrylic dome an can be operated remotely.

Figure 2 outlines the observational concept of the DIMS experiment. With the main focus on macroscopic DM studies, the nodes for the stereoscopic observation are positioned closer from each other (10–30 km), with respect to the typical strategy for meteor triangulation. Otherwise, the FoVs of the nodes would overlap only partially below 40 km, that is the altitude range at which a nuclearite is supposed to emit light (see Section 2). On the other hand, this choice affects the triangulation precision for meteors observed by DIMS cameras, which suffers from low parallax angles given their typically higher altitudes ($\sim$ 100 km).

4 Data analysis

DIMS carried out several observation campaigns since 2017, mainly in Japan and USA. In this work, we will focus on the analysis of the data taken during the night of 1st September 2019 at the Telescope Array site in Utah (USA) because of the optimal atmospheric conditions of that night. The two cameras, named N1 and N2, were installed respectively at the Hinckley and Black Rock Mesa sites at a distance of about 17 km and pointing towards Polaris. They observed continuously the sky for 6.5 hours at 30 Hz sampling frequency and triggered about 400 events in coincidence between the two. The trigger and acquisition software used was UFOCapture[a]. Data are stored as 8-bit *avi* files, with a frame dimension of 1920 px × 1080 px, together with observational metadata in *xml* format.

Triggered videos usually last few seconds, *i.e.*, some hundreds of frames. For this reason, the calibration of the whole video is performed over the median frame, also to increase the signal-to-noise ratio of the image. The data analysis tools used in this work for DIMS are based upon the ones developed for the reduction of the PRISMA Italian fireball network database (Barghini et al., 2019a; Barghini et al., 2019b; Carbognani et al., 2020). All the algorithms were developed in IDL[b].

We use the Hypparcos-Tycho catalogue (Perryman et al., 1997; Høg et al., 1997) as the reference for both astrometric and photometric calibration over observed stars in the FoV of DIMS cameras. Even if, at present time, there are published star catalogues that provide much better precision for both position and flux (*e.g.*, Gaia EDR3, Gaia Collaboration et al., 2021), we choose the Hypparcos catalogue because its H_p bandpass is much similar to the DIMS one (see Section 4.2). In any case, the positional precision of Tycho, of about 7 mas (milliarcseconds) for $V_T < +9$, is more than appropriate given our pixel resolution (see Section 4.1).

4.1 Astrometric calibration

The search and centering of bright sources over the median frame is performed by marginal distribution fitting implemented in the IDL Astronomy User's Library (Landsman, 1993). We look for stars with a signal four times above the background fluctuations in the central pixel of the point spread function (PSF), to remove most of false positives in the process. A first comparison with the reference catalogue is therefore performed by considering a simple spherical and undistorted projection in (α, δ) equatorial coordinates, since the cameras are conveniently pointed towards Polaris. In particular, catalogue positions (α_c, δ_c) of stars are projected onto the focal plane in (x_c, y_c) and compared with the list of found sources (x, y). The catalogue matches are built

[a] `https://sonotaco.com/soft`

[b] IDL – Interactive Data Language, Harris Geospatial Solutions `https://www.l3harrisgeospatial.com/Software-Technology/IDL`

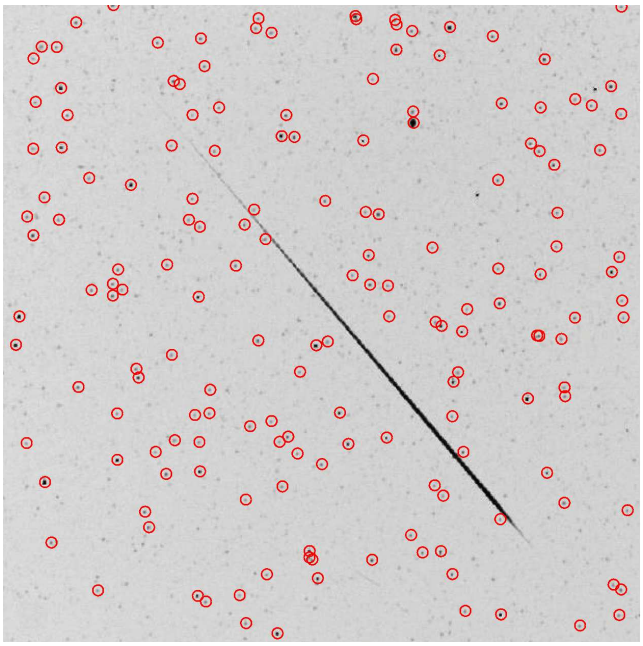

Figure 3 – Image of a portion (18° × 18°) of the FoV on the video of a sample event captured from N1 camera at the Hinckley TA site on the 2019 September 1 at $08^h16^m17^s$ UT. The meteor track is reconstructed from the video stream and it is plotted, in inverted colour scale, together with positions of identified stars up to +8 mag (red circles).

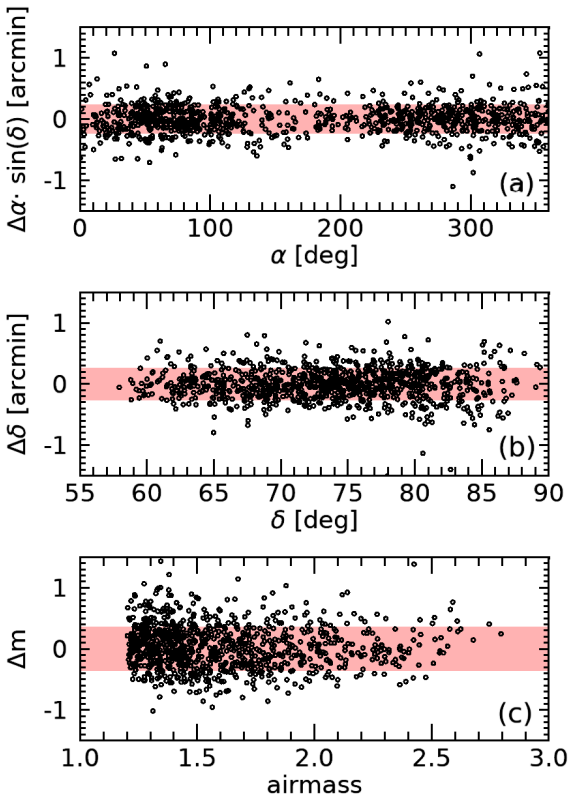

Figure 4 – Calibration results on the sample event video from Figure 3: (a) right ascension residuals between calibrated and catalogued stars positions; (b) same as panel a, but for declination; (c) magnitude residuals as a function of the airmass. Light red transparent bands in all panels plot the 1σ confidence interval deduced from residuals distributions.

from these two lists by considering the nearest neighbor couples within a correlation radius of 10 px. Once a first source-catalogue correlation has been made, we fit a refined astrometric solution with a standard CD matrix approach, accounting for plate rotation and scaling, plus an 8^{th} degree TNX[c] complete polynomial distortion. This process is iteratively repeated, by each step searching for fainter sources, increasing the magnitude limit on the catalogue and refining the plate solution, until a stable result is achieved in terms of number of identified stars and values of projection parameters.

Figures 3 and 4 show the results of this processing on a sample event captured by N1 camera at $08^h16^m17^s$ UT. A portion of the FoV is reported in Figure 3 (18° × 18°) around the triggered meteor track, together with the identified stars positions onto the frame, which are circled in red. The total FoV of our cameras results to be approximately 57° × 34°, in agreement with manufacturer specifications, with a pixel linear aperture of approximately 1.8′/px. By imposing a limiting magnitude of +8 on the catalogue, we are able to automatically identify about 900 stars per image with this algorithm. From Figure 3 it is evident that stars fainter then +8 mag are recognizable above sky background. However, it must be considered that this image was acquired and is plotted in a non-linear gamma scale correction (Canon Normal 1 gamma) which enhances the whiter (fainter) tones[d]. In any case, the sample of stars identified with such limiting magnitude is already more than sufficient to provide an accurate and precise calibration for our purposes. Figure 4a and b plot the right ascension and declination residuals of identified stars positions for the fitted plate solution in the same event of Figure 3. No systematic deviations are evident, and residuals are normally distributed around zero with a standard deviation of about 0.25′ (*i.e.*, 0.15 px), highlighting that we are already achieving a subpixel positional precision.

4.2 Photometric calibration

The dataset of stars built for the astrometric calibration on each triggered video is also used to deduce the photometric calibration of DIMS cameras. The flux F of each star is computed by means of circular aperture photometry, performed with a radius of 3 px and a sky annulus of [5,10] px inner/outer radii. By considering the exposure time of $\Delta t = 1/30$ s, we compute the experimental magnitudes $m_s = -2.5 \cdot \log_{10}(F/\Delta t)$ and compare them with catalogue values m_c. This allows us to deduce an estimation of the zero-point magnitude C and, also considering the airmass X for each observed star (Rozenberg, 1963), the atmospheric extinction coefficient k by fitting a linear trend over magnitude residuals:

$$\Delta m = m_c - m_s = C - kX \ . \qquad (4)$$

Figure 4c plots the magnitude residuals Δm as a function of the airmass, once the zero-point magnitude was

[c] `https://fits.gsfc.nasa.gov/registry/tnx.html`

[d] This effect is taken into account and corrected in the photometric analysis.

subtracted ($C \simeq 16$ for this example), showing a standard deviation of about 0.35 mag. As shown from this plot, we cannot recognize any significant dimming for increasing airmass, so that we neglect the effect of differential atmospheric extinction in this calibration.

Our system has a wide bandpass, given by the spectral response of the CMOS sensor. In particular, the quantum efficiency curve of our instrument (not shown) roughly covers the range from 300 to 1100 nm, is centred at 500 nm with a full-width at half-maximum of about 400 nm. Due to this specifications, we choose the Hipparcos magnitude H_p as the reference for our calibration. Another possible approach would consist in deducing an equivalent magnitude system for stars observed by DIMS cameras, by means of numerical integration of *UBVRI* bandpass weighted by the instrumental quantum efficiency and the star's color indices. However, for stars fainter then +4 in V, data about U, R and I magnitudes are lacking in literature and the numerical integration would be incomplete and giving less accurate results. Future improvements may include more detailed considerations about a better suited photometric system to be applied to DIMS data analysis.

DIMS cameras were also calibrated with a large integrating sphere at the National Institute of Polar Research (Ogawa et al., 2020). These measurements allow us to correct for the efficiency lowering from the centre to the edges of the focal surface, due to the whole optic system of the instrument. According to the approach proposed in Barghini et al. (2019a), the relative efficiency η can be empirically modelled as a function of the radial distance r from the FoV centre as:

$$\eta(r) = 1 - A_0 r - A_1 \left[\mathrm{e}^{-\frac{A_0}{A_1} r} - 1 \right] . \qquad (5)$$

We estimated $A_0 = (750 \pm 4) \cdot 10^{-6}$ px^{-1} and $A_1 = (97 \pm 3) \cdot 10^{-3}$ from these measurements. The results of this calibration and the fitted curve are plotted in Figure 5. The relative efficiency drops with an asymptotic linear loss of $\sim 7.5\%$ each 100 px, and reaches as low as 30% to the very edge of the focal surface. This result is used to correct for this efficiency bias on flux measurement of stars used for the photometric calibration.

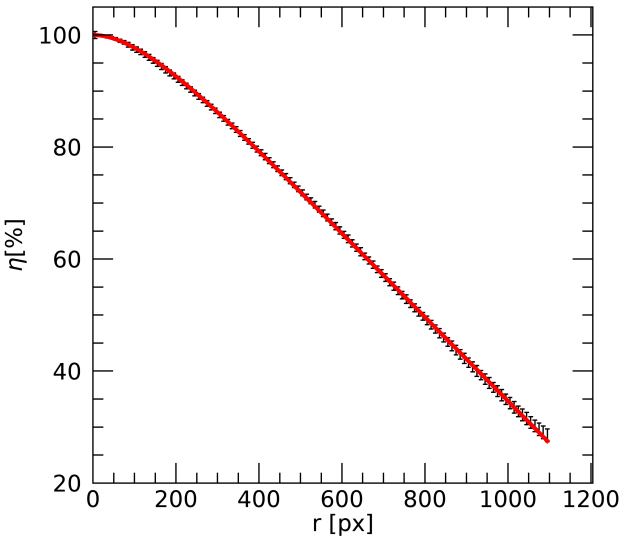

Figure 5 – Plot of the radial relative efficiency curve of the DIMS camera obtained thanks to the calibration with the integrating sphere, modelled as described by Equation 5 (red curve).

4.3 Meteor analysis

For each event that triggered on both N1 and N2 cameras, the video analysis for the track reconstruction and triangulation is performed. A pre-centering algorithm is used to determine a first estimation of the meteor position onto the focal plane by a clustering algorithm that looks for over-threshold pixels and selecting only clusters with (t, x, y) correlation coefficients $|\rho| > 0.7$. This algorithm is complementary to the UFOCapture acquisition trigger and was tested against the whole dataset for both N1 and N2 cameras. The meteor position, frame by frame, is then computed by an unbiased filtered barycentre method (Barghini et al., 2019b) and the meteor magnitude is computed by aperture photometry, circular or elliptical for very elongated PSF (*i.e.*, high speed values). Then, triangulation between N1 and N2 cameras provides the three-dimensional trajectory of the event in the atmosphere, in the straight-line hypothesis. The standard plane intersection method by (Ceplecha, 1987) is used to derive a starting point to the more refined triangulation algorithm proposed by (Borovička, 1990). The implementation of the dynamical model fitting and pre-atmospheric orbit computation will be part of future work.

Figure 6 shows the main preliminary results of this analysis applied to the sample event discussed in previous sections. The luminous flight of the meteor started at an altitude of 95 km with an entry velocity of about 16 km/s reached its maximum intensity of $M = +0.5$ (absolute magnitude, scaled at 100 km altitude at the observer's zenith) and then suddenly decelerated, just to extinguish at 80 km of altitude after 2.8 s of flight. Figure 6a shows that there is a small delay $\delta t \simeq 0.07$ s between the times recorded by N1 and N2 cameras, that will be corrected for future observations by GPS synchronization of DIMS stations.

5 Results and discussion

Figure 7 summarizes the main results of the statistical analysis of the DIMS events dataset presented in this work. Panels a, b and c plots the distributions of the main physical parameters deduced from the triangulation of the events between N1 and N2 cameras, as previously described in Section 4.3. Disclosing in advance the final result, none of the analyzed events showed indisputable signatures for a non-meteor origin. In particular, Figure 7a shows that the beginning heights are distributed between 70 and 130 km, as expected for meteors. The entry velocity histogram (Figure 7b) displays the typical bi-variated distribution for low (asteroidal) and high (cometary) velocity. Only 8 events show a median speed above the 72 km/s but, af-

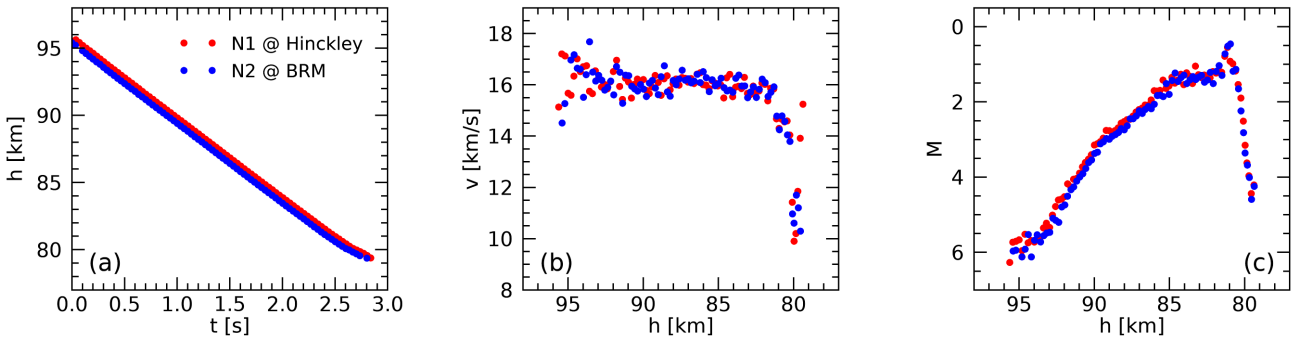

Figure 6 – Main results of the meteor analysis applied on the sample event pictured in Figure 3. (a) Triangulated meteor altitude as a function of the elapsed time from the start of the bright flight; (b) reconstructed speed module; (c) absolute magnitude of the meteor, scaled at 100 km at the observer's zenith.

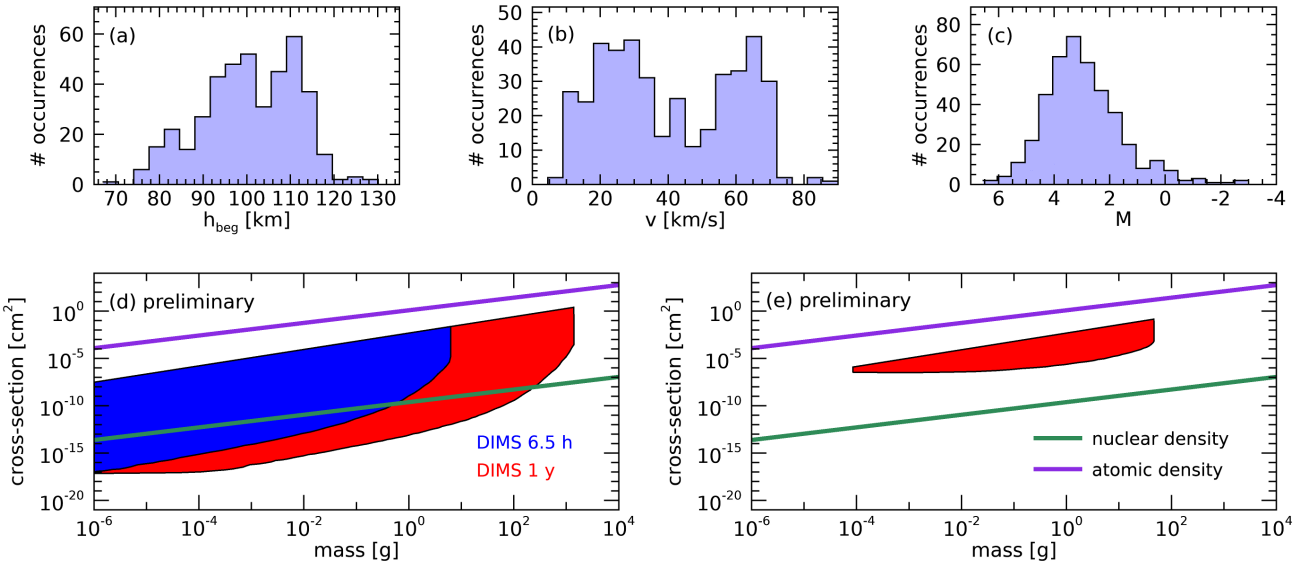

Figure 7 – Distributions of beginning height (a), speed (b) and absolute magnitude (c) for meteors observed by DIMS cameras N1 and N2 in the dataset presented in this work. Expected constraints on macro's mass and cross-section (preliminary results) are derived according to De Rujula & Glashow (1984) formulation (d) and Sidhu et al. (2019) (e), for the 6.5 hours exposure of the current dataset (blue region) and the 1-year projection (red region). The green and purple lines in panels d,e plot the cross-section respectively for macros with nuclear and atomic density.

ter a careful revision of their analysis, they were found to be badly reconstructed from triangulation and therefore discarded.

The absolute magnitude distribution of Figure 7c suggests that the DIMS system is not completely efficient in detecting events fainter than absolute magnitude +4. The limiting magnitude for meteors observed by the DIMS system results to be about $M = +6$ from this analysis. Future work will include a careful investigation about the trigger efficiency for meteors as a function of their magnitude and speed, to correct the magnitude distribution for this bias and evaluate, for instance, the population index of our sample.

On the subject of macroscopic DM investigation, we can evaluate the expected constraints to macros flux that could be established thanks to the DIMS experiment, following the approach proposed by Sidhu & Starkman (2019). In summary, since we did not observe any anomalous event in our data, this would allow to rule out a certain region in the macro parameters space of mass and cross-section. The definition of this region depends upon which model we consider for the macro phenomenology (Section 2), in addition to the identified limiting magnitude for such events observed by the instrument. Figure 7d shows this result according to the formulation of De Rujula & Glashow (1984), for the 6.5 hours of exposure of the 1st September 2019 (blue region) and the expected limits for 1 year of observations (red region, assuming a 10% duty cycle). In this latter scenario, DIMS has the potential to probe macros with mass up to 10^3 g in the 1-year projection. This conclusion is radically different if we consider the model by Sidhu et al. (2019) instead. From Figure 7e, it is evident that DIMS would not be able to provide any constraints with the dataset presented in this paper, and would reach masses just up to 10^2 g in the 1-year projection, with a much narrower range in the cross-section domain. In any case, these results are preliminary and

refers to the best case, in which we assume a 100% efficiency at the limiting magnitude +6, being aware that this is not realistic above +4 mag.

6 Conclusions

DIMS is a novel experiment dedicated to the study of macroscopic DM and interstellar meteors. It started in 2017 and deployed high-sensitivity and wide-field CMOS cameras observing the night sky to look for such faint and fast-moving particles. The observation campaigns led so far by DIMS were mainly dedicated to feasibility studies for the detection of these exotic particles. Nuclearites are a particular candidate for macroscopic DM and, if they exist, are supposed to impact the Earth and generate luminous, meteor-like events in the atmosphere. However, their signature would be recognizable apart from regular meteors, since they are expected to emit light in a much lower altitude range ($\lesssim$ 40 km) and to move at a much higher speed ($\sim$ 250 km/s).

In this paper, we described our work on the calibration of DIMS sensors by means of standard astronomical techniques applied to observed stars in the FoV during one campaign on 1st September 2019 at the Telescope Array site (Utah, USA) with two DIMS cameras. We designed a tailored data analysis pipeline that is able to automatically identify stars up to +8 mag and use this dataset as reference for both astrometric and photometric reduction of the video stream that captured the event. In this way, we achieved sub-pixel positioning precision level for the determination of the event trajectory. Furthermore, the DIMS sensor has a wide bandpass and we therefore considered a wide-band photometric system, like the one from the Hipparcos catalogue. The calibration of DIMS cameras with an integrating sphere allowed us to account also for the efficiency radial modulation within the focal plane of the CMOS sensor.

The meteors observed during that night ($\sim$ 400) were analyzed by means of this pipeline and we presented here some preliminary statistical results and conclusions on the potentiality of the DIMS system for both meteor studies and macroscopic DM investigations. None of the events showed unquestionable evidence for a non-meteor origin. Future developments would address, inter alia, the completion of the analysis pipeline, including the evaluation of a dynamical model and pre-atmospheric orbit determination, and a dedicated study of the trigger capabilities in detecting such faint and fast-moving events.

Acknowledgements

This work is partially supported by JSPS KAKENHI Grant Number JP19H01910, by the joint research program of the Institute for Cosmic Ray Research (ICRR), the University of Tokyo, and by National Science Centre, Poland grant 2020/37/B/ST9/01821. We thank to members of the Telescope Array experiment for their help to achieve the observations in Utah, and also Dr. K. Tsuno (RIKEN) and members of the National Institute of Polar Research for their help to calibrate the camera using a large integrating sphere. The authors from the University of Turin acknowledge support from Compagnia di San Paolo within the project ex-post-2018.

References

Abe S., Arahori M., Barghini D., et al. (2021). "DIMS Experiment for Dark Matter and Interstellar Meteoroid Study". In *37th International Cosmic Ray Conference (ICRC2019)*, volume 37 of *International Cosmic Ray Conference*.

Barghini D., Gardiol D., and Carbognani A. (2019a). "Improving astrometry and photometry reduction for PRISMA all-sky cameras". In Rudawska R., Rendtel J., Powell C., Lunsford R., Verbeeck C., and Knöfel A., editors, *Proceedings of the 37th International Meteor Conference Pezinok-Modra, Slovakia, 30 August - 2 September 2018.* pages 41–45.

Barghini D., Gardiol D., Carbognani A., and Mancuso S. (2019b). "Astrometric calibration for all-sky cameras revisited". *Astron. Astrophys.*, **626**, A105.

Barghini D., Valenti D., Abe S., et al. (2021). "Characterization of the DIMS system based on astronomical meteor techniques for macroscopic dark matter search". In *37th International Cosmic Ray Conference (ICRC2021)*, volume 37 of *International Cosmic Ray Conference*.

Borovička J. (1990). "The Comparison of Two Methods of Determining Meteor Trajectories from Photographs". *Bull. Astron. Inst. Czechoslov.*, **41**, 391–396.

Carbognani A., Barghini D., Gardiol D., et al. (2020). "A case study of the May 30, 2017, Italian fireball". *Eur. Phys. J. Plus*, **135:2**, 255.

Ceplecha Z. (1987). "Geometric, dynamic, orbital and photometric data on meteoroids from photographic fireball networks". *Bull. Astron. Inst. Czechoslov.*, **38**, 222–234.

De Rujula A. and Glashow S. L. (1984). "Nuclearites-a novel form of cosmic radiation". *Nature*, **312:5996**, 734–737.

Gaia Collaboration, Brown A. G. A., Vallenari A., Prusti T., et al. (2021). "Gaia Early Data Release 3. Summary of the contents and survey properties". *Astron. Astrophys.*, **649**, A1.

Høg E., Bässgen G., Bastian U., et al. (1997). "The TYCHO Catalogue". *Astron. Astrophys.*, **323**, L57–L60.

Jacobs D. M., Starkman G. D., and Lynn B. W. (2015). "Macro dark matter". *Mon. Not. R. Astron. Soc.*, **450:4**, 3418–3430.

Kajino F., Ide I., Ide R., et al. (2019). "Study for Moving Nuclearites and Interstellar Meteoroids using High Sensitivity CMOS Camera". In *36th International Cosmic Ray Conference (ICRC2019)*, volume 36 of *International Cosmic Ray Conference*. page 525.

Kajino F., Takami S., Nagasawa M., et al. (2017). "Study of Fast Moving Nuclearites and Meteoroids using High Sensitivity CMOS Camera with EUSO-TA". In *35th International Cosmic Ray Conference (ICRC2017)*, volume 35 of *International Cosmic Ray Conference*. page 924.

Landsman W. B. (1993). "The IDL Astronomy User's Library". In Hanisch R. J., Brissenden R. J. V., and Barnes J., editors, *Astronomical Data Analysis Software and Systems II*, volume 52 of *Astronomical Society of the Pacific Conference Series*. page 246.

Ogawa Y., Kadokura A., and Ejiri M. K. (2020). "Optical calibration system of NIPR for aurora and airglow observations". *Polar Sci.*, **26**, 100570.

Perryman M. A. C., Lindegren L., Kovalevsky J., et al. (1997). "The HIPPARCOS Catalogue". *Astron. Astrophys.*, **323**, L49–L52.

Rozenberg G. V. (1963). "Reviews of Topical Problems: Twilight Phenomena, Their Nature, and Use for Atmospheric Research". *Soviet Physics Uspekhi*, **6:2**, 198–249.

Shinto D., Iwami Y., Fujioka M., et al. (2021). "Solar Power Supply and Environmental Control System for DIMS Experiment". In *37th International Cosmic Ray Conference (ICRC2019)*, volume 37 of *International Cosmic Ray Conference*.

Sidhu J. S. et al. (2019). "Macro detection using fluorescence detectors". *J. Cosmol. Astropart. Phys.*, **2019:2**, 037.

Sidhu J. S. and Starkman G. (2019). "Macroscopic dark matter constraints from bolide camera networks". *Phys. Rev. D*, **100:12**, 123008.

Witten E. (1984). "Cosmic separation of phases". *Phys. Rev. D*, **30:2**, 272–285.

Handling Editors: Ákos Kereszturi and Javor Kac
This paper has been typeset from a LaTeX file prepared by the authors.

Meteorix — A new processing chain for real-time detection and tracking of meteors from space

M. Millet[1,2], *N. Rambaux*[3], *A. Petreto*[1,2], *F. Lemaitre*[1], *L. Lacassagne*[1]

In the framework of the Universitary CubeSat project Meteorix of Sorbonne University, this article describes a processing chain for meteor detection from space. Unlike ground detection using stationary cameras with a still background, detection aboard a nano-satellite needs to deal with a camera in motion and a moving background. The main parts of this chain are an estimation of the apparent movement and the computation of angular statistics. The first results show a detection probability close to 96% on the whole set of Chiba videos from the PERC (Planetary Exploration Research Center) Meteor Project.

Received 2021 October 26

This work has been presented at the International Meteor Conference 2021 (held online).

1 Introduction

Meteorix (Rambaux et al., 2019) is the first Universitary CubeSat mission from Sorbonne University and its University Space Center. This mission has three main objectives. The main one is the detection and the characterisation of meteors and space debris in order to estimate the flux of these bodies entering in the atmosphere. The second is an educational goal to involve students in a space mission during all its phases. The third is a technological goal to demonstrate the feasibility of a real-time computer vision application on board a nano-satellite with strong constraints in terms of power consumption and execution time.

Space detection allows to go beyond meteorological constraints that ground detection has and offers a wide sky coverage. In 2016, Chiba University led an ISS mission named *ISS Meteor* in which a high resolution camera was filming toward Earth (Arai et al., 2014). They showed the feasibility of space observation of meteors but the recognition step was performed by human operators on Earth (Arai et al., 2018).

This proceeding covers the technological goal of the mission and it describes a new processing chain for meteor detection suited for space detection. Another proceeding (Rambaux et al., 2021) describes the optical part of the payload and its advancement.

2 State of the Art

Up to now, several detection techniques have been developed for ground detection by using a stationary camera, computer and processing chain.

In 2005, a review of processing chains (Molau & Gural, 2005) describes the different common steps of them and the image processing techniques used. Processing chains seem generally include at least three steps:

(i) A pre-processing step that mainly consists in keeping only the moving objects using a background subtraction technique (frame differencing, mean or median filter).

(ii) A classification step to know if there is a meteor in the frame. After a threshold, regions of interest are created from the brightest remaining pixels. Techniques exploiting spatial and/or temporal correlation are used to determine if a region is a meteor. The most popular techniques are the Hough transform, the template matching and the temporal tracking.

(iii) An extraction step to save each frame of a meteor as a sequence.

Some others steps can be included for analysis (orbit calculation, photometry...) but this goes beyond the scope of the meteor detection.

Four chains are described, including MetRec (Molau, 1999) and MeteorScan (Gural, 1997) which are very popular and still used nowadays, sometimes as a component of a new processing chain.

In 2009, (Gural & Šegon, 2009) propose a new processing chain in which the pre-processing step consists of merging 256 frames into a color bitmap image taking advantage of the fact that meteors are brighter than background to reconstruct the meteor trail. The blue channel is used to store values of the brightest pixels of images. The red and green channels are used to store the number of the image containing this bright pixel. That allows to keep the temporal dimension of the event. Then the classification is done by MeteorScan. An improved frames compression technique is used in the RPi Meteor Station (Vida et al., 2016) which is a processing chain designed for low cost embedded systems like Raspberry Pi.

The Fireball Recovery and InterPlanetary Observation Network (FRIPON) (Colas et al., 2020) comes with its own processing chain (Audureau et al., 2014), based on a classic background detection where successive frames are subtracted to keep only the moving pixels and on a tracking step.

Since few years, processing chains using neural networks have emerged. In (Galindo & Lorena, 2018), authors compare several convolutional neural networks (CNN) pre-trained with a huge dataset (ImageNet or

[1]LIP6, Sorbonne Université, CNRS
[2]Lerity - Alcen
[3]IMCCE/Paris Observatory, Univ. PSL, Sorbonne Université, CNRS, Paris, France.

IMO bibcode WGN-496-millet-meteorix
NASA-ADS bibcode 2021JIMO...49..181M

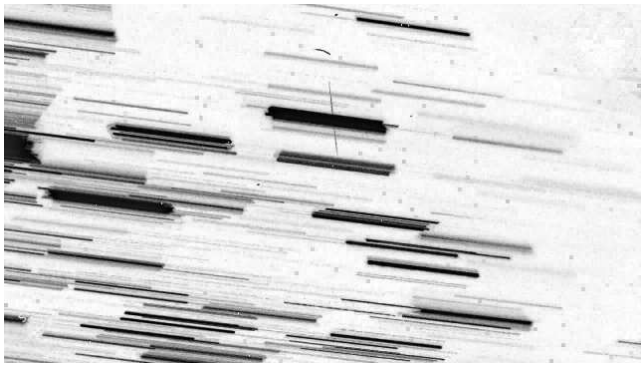

Figure 1 – Example of 256 frames compressed in one from RPi Meteor Station. Where are the 2 meteors? Each line can be the trace of a city (public lighting), a bright cloud or of a meteor.

Fashion-MNIST) in order to train with a small dataset of meteor images. The best configuration is composed of 18 layers and gives a detection probability of 96%. However, these experiments were done with a GPU Nvidia Quadro P4000 which cannot be embedded within a nano-satellite: its average TDP[a] is 105 Watt.

In 2020, another CNN was proposed (Cecil & Campbell-Brown, 2020) for the Canadian network CAMO in order to automate the classification step currently partially performed by a human operator. The network has been trained with the entire images to be used as a complete detector (therefor a one step processing chain). However, the number of false positives was too high. The solution was to add a pre-detection step as input of the network using the same image processing techniques (addition of several frames, Hough transforms). This processing chain has a detection probability of 99.8% and can reach a frame rate of 21 fps with a CPU Intel i7 6850k. Unfortunately, this CPU cannot be embedded within a nano-satellite, its average TDP is 140 Watt.

In the end, the image processing techniques discussed above are suitable when the camera is stationary where the only movements come from celestial objects and clouds. This is not the case for our nano-satellite. Indeed, its movement (7.2 km/s) must be taken into account in addition to that of Earth (460 m/s) making these techniques unsuitable because all points move between two frames. This is especially the case for the frame differencing algorithm or fusions of multiple frames (as shown in Figure 1).

Moreover, neural networks are mainly used as a component of the processing chain and require a preprocessing step using the same image processing techniques as the others. The hardware used for inference is also more powerful than that of a nano-satellite and they are not compatible with the energy constraints of a such embedded system.

For these reasons, we propose a new processing chain adapted for space detection that can be optimized to run in low-power system and using an optical flow estimation.

[a]Thermal Design Power

3 Processing Chain

The proposed chain is divided into seven steps.

The first step is an optical flow estimation. It is an estimation of the apparent movement between two images for each pixel (in pixels by frame). The Horn & Schunck algorithm (Horn & Schunck, 1981) in a pyramidal version (Meinhardt-Llopis et al., 2013) is well suited for the embedded constraints. Indeed, the algorithm is iterative in order to improve the accuracy. The pyramidal side allows estimation of wider movements.

The second step is a threshold on the speed – set to 2.5 px/frame – giving a binary mask of the fastest pixels. This threshold has been set after a manual analysis of video sequences of meteors (PERC, 2016) of ISS Meteor mission. In this mission they showed the feasibility of a space observation of meteors but the recognition step was done by human on Earth. Meteors movements are faster than Earth movement so this step allows to keep only the fastest pixels. Some others fast events can also remain after this step and will be eliminate later. Finally, two morphological operators (opening and closing) are applied on the binary mask in order to remove lonely pixels and to regroup nearby clusters of pixels.

The third step is a Connected Component Labeling (CCL) (Lacassagne & Zavidovique, 2009) that regroups connected pixels together into a region and provides then a unique label.

The fourth step is a Connected Component Analysis (CCA) (Cabaret & Lacassagne, 2014) that computes some features for each region such as its surface, or its average speed $\bar{v}$, the average angle $\bar{\alpha}$ and its standard deviation σ_α. The last two features are computed using formulas adapted for circular data (Fisher, 1993):

$$C = \sum_{i=1}^{n} cos(\alpha_i) \tag{1}$$

$$S = \sum_{i=1}^{n} sin(\alpha_i) \tag{2}$$

$$R_1 = \sqrt{C^2 + S^2} \tag{3}$$

$$\bar{\alpha} = atan_2\left(\frac{C}{n}, \frac{S}{n}\right) \tag{4}$$

$$\sigma_\alpha = \sqrt{-2 \times \ln \frac{R_1}{n}} \tag{5}$$

with n the number of pixels of the connected component, and i the i-th pixel of the connected component (and α_i its angle).

The fifth step is a classification by the angular standard deviation. The connected components represent the fastest objects of the scene like meteors, space debris and lightnings and it is necessary to differentiate them to keep only the first ones. The angular standard deviation is a good metric to do that. In fact, a meteor has a rectilinear path that means all its pixels have the same direction, inducing a low angular standard deviation. By contrast, the apparent movement of a lightening is a circular wave, its pixels go in all directions, inducing a high angular standard deviation. This step gives a list of supposed meteors.

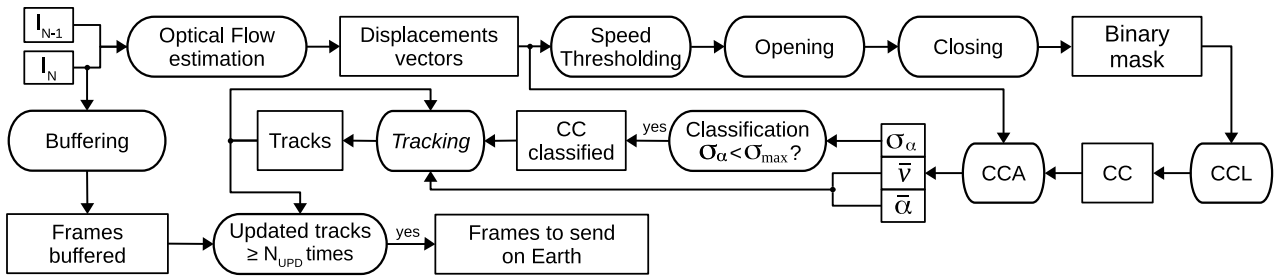

Figure 2 – CC = Connected Components, CCL = Connected Components Labeling, CCA = Connected Components Analysis, $\bar{v}$ = average speed, $\bar{\alpha}$ = mean angle, σ_α = angular standard deviation, $\sigma_{max} = 30\,\text{deg}$, $N_{MAJ} = 3$

The sixth step is a temporal tracking. This step has two goals. Firstly, the temporal dimension allows to confirm if a supposed meteor is a true meteor and not a false positive. For that, a same supposed meteor detected at least three times is considered as a true meteor. Secondly, to group the meteor images in a sequence.

The last step consists of sending meteors sequences on Earth. For meteor shower, the detection is limited to 20 meteors per day. In this case, the satellite will send the data of the first and last frame of the sequence with the regions of interest containing meteors. For sporadic meteor, we plan one meteor per day and all frames of it will be send.

A first port of these algorithms have been done on the CPU of Nvidia Jetson boards to estimate the processing time and the power consumption. For example, the best configuration of Horn & Schunck on Nvidia Jetson TX2 board consumes 22 ns/px and 133 nJ/px (Petreto et al., 2018). The latest CPUs should further improve these metrics.

4 Validation bench

A validation bench has been developed to qualify the proposed processing chain. For that, 150 videos from the ISS Meteor experiment were analyzed in which 50 meteors were found. A *ground truth* was built for each meteor, containing the date and the coordinates for appearance (x_0, y_0, t_0) and disappearance (x_1, y_1, t_1). These information allow the calculation of the meteor's path.

Each sequence containing at least one meteor is tested with the bench. A detection is considered as valid if there is a supposed meteor progressing on the ground truth trajectory and in the right direction. Finally, three scores are given.

(i) A binary score indicating if the meteor has been detected on at least 3 frames or not.

(ii) A ratio of the number of frames labelled as containing a meteor compared to the expected numbers of frames containing a meteor from the ground truth.

(iii) And the number of false positives in the sequence.

5 Results

For this first version 48 meteors of 50 are detected, which gives a detection probability of 96%. Moreover, 70% of images containing a meteor are labelled as such. The 30% remaining may come from human approximation in the ground truths (e.g. the time frame number of the beginning of the detection and/or the end of detection) or meteor undetected with or without extrapolation.

As a reminder, the camera is considered in motion pointing towards the Earth, not stationary on Earth pointing towards the sky and the processing chain has to deal with different types of scenes (see Figure 3) increasing the difficulty and so, requiring more complex algorithms. For this reason, these results can not be directly compare to those of the state of the art.

6 Conclusion

In this work, a new processing chain for meteor detection is proposed. It is designed to work on space observations in order to be embedded on the nano-satellite of the Meteorix mission. A validation bench was developed to qualify the processing chain with a dataset of meteors observed from space. The first results give a detection probability close to 96%.

Acknowledgements

ESEP (Exploration Spatiale des Environnements Planétaires), DIM ACAV+ and RFSI from Région Île-de-France, CNES Nanolab Academy, IDEX Sorbonne Universités for funding this research.

References

Arai T., Kobayashi M., Yamada M., Matsui T., and Cometss Project Team (2014). "Meteor Observation HDTV Camera Onboard the International Space Station". In *Lunar and Planetary Science Conference*, volume No. 1777. page 1610.

Arai T., Kobayashi M., Yamada M., Senshu H., Maeda K., Wada K., Ohno S., Ishibashi K., Ishimaru R., Matsui T., and Fortenberry M. (2018). "On-Going Status of METEOR Project Onboard the International Space Station". In *Lunar and Planetary Science Conference, volume 49 of Lunar and Planetary Inst. Technical Report*. page 2525.

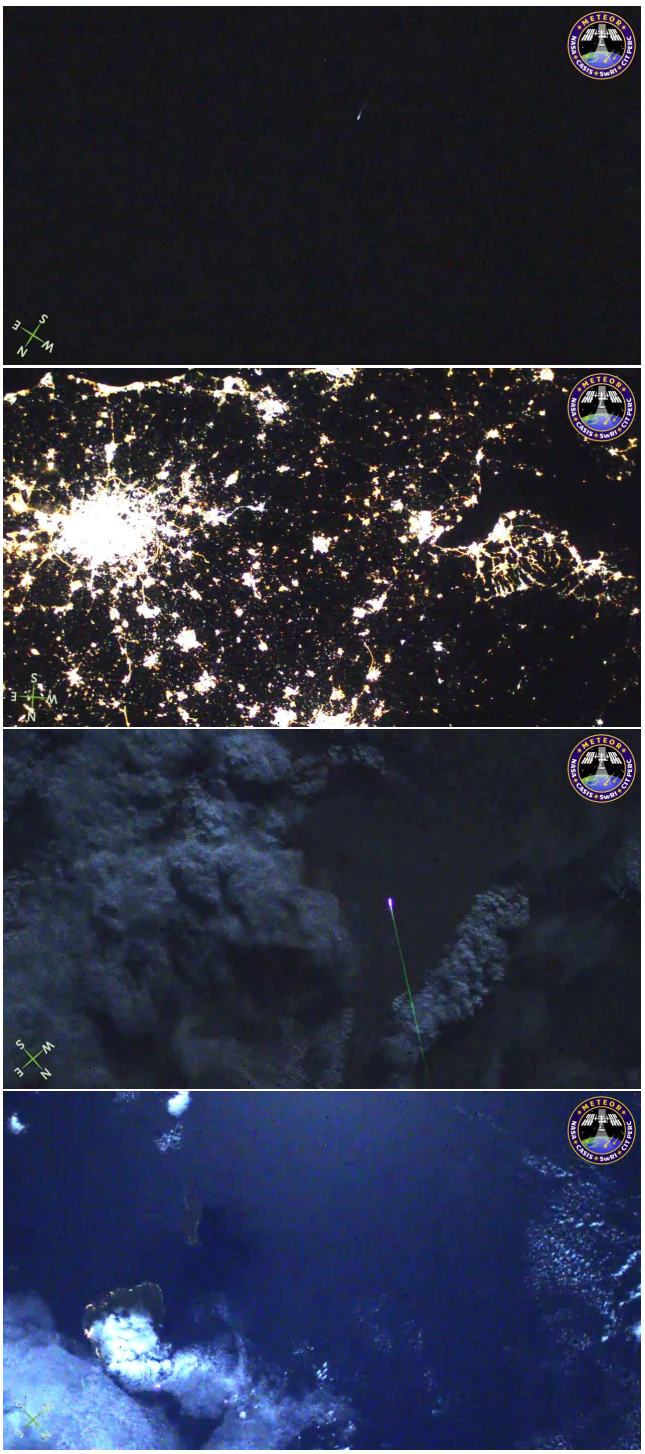

Figure 3 – The scene filmed by the camera can vary, from complete darkness to a cloudy or a moonlit scene. Each picture contains a meteor (from Chiba sequences).

Audureau Y., Marmo C., Bouley S., Kwon M.-K., Colas F., Vaubaillon J., Birlan M., Zanda B., Vernazza P., Caminade S., and Gattecceca J. (2014). "FreeTure: A Free software to capTure meteors for FRIPON". In *International Meteor Conference, 2014, Giron, France*. pages 39–41.

Cabaret L. and Lacassagne L. (2014). "What is the world's fastest Connected Component Labeling Algorithm?". In *IEEE International Workshop on Signal Processing Systems (SiPS)*. pages 97–102.

Cecil D. and Campbell-Brown M. (2020). "The application of convolutional neural networks to the automation of a meteor detection pipeline". *Planetary and Space Science*, **186**, 104920.

Colas F., Zanda B., Bouley S., Jeanne S., Malgoyre A., et al. (2020). "FRIPON: a worldwide network to track incoming meteoroids". *Astronomy and Astrophysics*, **644**, A53.

Fisher N. I. (1993). *Statistical Analysis of Circular Data*. Cambridge University Press.

Galindo Y. and Lorena A. C. (2018). "Deep transfer learning for meteor detection". In *Anais do XV Encontro Nacional de Inteligência Artificial e Computacional, 2018*. pages 528–537.

Gural P. (1997). "An operational autonomous meteor detector: Development issues and early results". *WGN, Journal of the International Meteor Organization*, **25**, 136–140.

Gural P. and Šegon D. (2009). "A new meteor detection processing approach for observations collected by the Croatian Meteor Network (CMN)". *WGN, Journal of the International Meteor Organization*, **37**, 28–32.

Horn B. K. and Schunck B. G. (1981). "Determining optical flow". *Artificial intelligence*, **17:(1-3)**, 185–203.

Lacassagne L. and Zavidovique B. (2009). "Light speed labeling for RISC architectures". In *International Conference on Image Processing (ICIP). IEEE, 2009*. pages 3245–3248.

Meinhardt-Llopis E., Sánchez J., and Kondermann D. (2013). "Horn-Schunck Optical Flow with a Multi-Scale Strategy". *Image Processing on line*, **20**, 151–172.

Molau S. (1999). "The meteor detection software MetRec". In *International Meteor Conference, 1998*.

Molau S. and Gural P. (2005). "A review of video meteor detection and analysis software". *WGN, Journal of the International Meteor Organization*, **33**, 15–20.

PERC (2016). "Chiba ISS Meteor website". `http://www.perc.it-chiba.ac.jp/project/meteor/gallery.html`.

Petreto A., Hennequin A., Koehler T., Romera T., Fargeaix Y., Gaillard B., Bouyer M., Meunier Q., and Lacassagne L. (2018). "Energy and execution time comparison of optical flow algorithms on SIMD and GPU architectures". In *Conference on Design and Architectures for Signal and Image Processing (DASIP). IEEE, 2018*. pages 25–30.

Rambaux N., Vaubaillon J., Derelle S., Jacquart M., Millet M., Lacassagne L., Petreto A., Simoneau P.,

Baillié K., Desmars J., Galako D., and Chotin R. (2021). "Meteorix camera tests for space-based meteor observations". *WGN, Journal of the International Meteor Organization*, **49**, 142–144.

Rambaux N., Vaubaillon J., Lacassagne L., Galayko D., Guignan G., Birlan M., Boisse P., Capderou M., Colas F., Deleflie F., Deshours F., Hauchecorne A., Keckhut P., Levasseurd-Regourd A., Rault J., Zanda B., and all students of the Meteorix team (2019). "Meteorix: A cubesat mission dedicated to the detection of meteors and space debris". In *ESA NEO and Debris Detection Conference- Exploiting Synergies -ESA/ESOC, Darmstadt, Germany*.

Vida D., Zubović D., Šegon D., Gural P., and Cupec R. (2016). "Open-source meteor detection software for low-cost single-board computers". In *International Meteor Conference, 2016, Egmond, The Netherlands*. pages 307–318.

Handling Editor: Javor Kac
This paper has been typeset from a LaTeX file prepared by the authors.

MALBEC: discrepancy between expected and observed number of meteors for stratospheric cameras

J. Vaubaillon[1], *A. Rietze*[2], *D. Zilkova*[3]

The MALBEC project aims to observe meteors from two stratospheric platforms. The theoretical demonstration of stratospheric double-station observation is performed, in terms of absolute and relative physical distance and direction between the two cameras. These simulations are performed for almost any weather condition that allows the flight. The reduced area for each camera field of view is computed thanks to the usual method. A comparison with real data from (Ocaña et al., 2019) shows that the theoretical figures under-estimate the real number of detected meteors by a factor of 5. Several studies are currently being conducted on this topic. Those on-going studies are needed to fully reconcile the here described numbers of detected meteors.

Received 2021 October 14

This work has been presented at the International Meteor Conference 2021 (held online).

1 The MALBEC project

Meteor observation are widely performed using optical cameras. When used in pairs of at least two, they allow the triangulation of the meteors, yielding to more scientific results (Vaubaillon et al., 2020). These are especially much needed to record meteor outburst, which, by nature, are unique, and quite rare for one given shower. Such outburst might last from a few dozen minutes to a few hours. The recording of unique event might be hampered by orbital geometry (e.g. radiant under the horizon) or cloud cover (Vaubaillon et al., 2015). In such a case mobile observations are required.

The Meteor Automated Light Balloon Experimental Camera (MALBEC) project aims to guarantee the successful observation of meteor showers by setting a double-station network of cameras in the stratosphere for a few hours. We focus here on the feasibility of such endeavour. Our previous work described the method used to compute the expected 3D-trajectory of a stratospheric nacelle (Zilkova & Vaubaillon, 2019). For a double-station observation, the physical distance between the two cameras should be in the [40; 120] km range. In the framework of the MALBEC project, knowing that the two nacelle will experience different weather conditions, we need to check if this condition holds true for the entire observation duration. In addition, the two cameras must point towards the same portion of atmosphere in order to record the same meteor. Zilkova and Vaubaillon (2019), and Vaubaillon et al. (2022) showed that even under non-anti-cyclonic conditions, and with a launch time shift of up to one minute, the physical distance between the nacelles is kept well within the [40; 120] km range. Similarly, the change of azimuth required to keep the two cameras pointing toward the same portion of atmosphere at the meteor altitude is fairly small.

However, in order to make the most of such observation, the overall orientation of the cameras must be optimized. Usually, one camera is oriented so that the azimuth points towards the other camera. However, introducing a shift for both cameras leads to a greater surveyed area at the altitude of the meteors. The ideal geometry and azimuth shift is a compromise between many factors, and must take into account the weather and change of apparent location of the radiant. The criterion to decide which geometry to choose is the number of expected recorded meteors, and the number of double-station meteors allowing the computation of reliable orbits. In this paper, we focus on the expected number of meteors recorded by the two cameras.

2 Expected number of recorded meteors

The method to compute the expected number of meteors recorded by a camera was developed by several authors, and what follows is a shortened version of the following papers: Bellot Rubio (1994); Koschack and Rendtel (1990); Gural and Jenniskens (2000); Koschny and Zender (2000); Ocana et al. (2011); Ocaña (2017).

The number of meteors recorded by naked eye is $HR_e = ZHR\ t\ sin(h)\ /\ r^{6.5-LM_e}$, with the zenithal hourly rate ZHR, the duration of the observation t, the height of the radiant above the horizon h, the shower population index r and the naked eye limiting magnitude LM. Under normal conditions, a human naked eye has a limiting magnitude of 6.5 and field of view considered as a circle of ~ 50 deg, which translates into a surveyed area of 37000 km^2 (Koschack & Rendtel, 1990). A video camera will present a different field of view, which is taken into account by computing a reduced of $A_{red} = \Sigma f_i\ A_{phy}$, with A_{phy} the physical surveyed area for a given pixel (or unit of 2D-angle) and f_i a correction factor. f_i takes into account the magnitude loss caused by the airmass, physical distance, and apparent velocity. It is worth mentioning that the latter depends on the geometry, and therefore differs from one camera to the other. The advantage of going stratospheric is that the atmospheric absorption is low and the pointed

[1]IMCCE, Observatoire de Paris, PSL Research University, CNRS, Sorbonne Universités, UPMC Univ. Paris 06, Univ. Lille., France.
Email: jeremie.vaubaillon@obspm.fr
[2]University of Oldenburg, Oldenburg, Germany.
Email: athleen.selma.rietze@uni-oldenburg.de
[3]Comenius University in Bratislava, Slovakia.
Email: danica.zilkova@fmph.uniba.sk

IMO bibcode WGN-496-vaubaillon-malbec
NASA-ADS bibcode 2021JIMO...49..186V

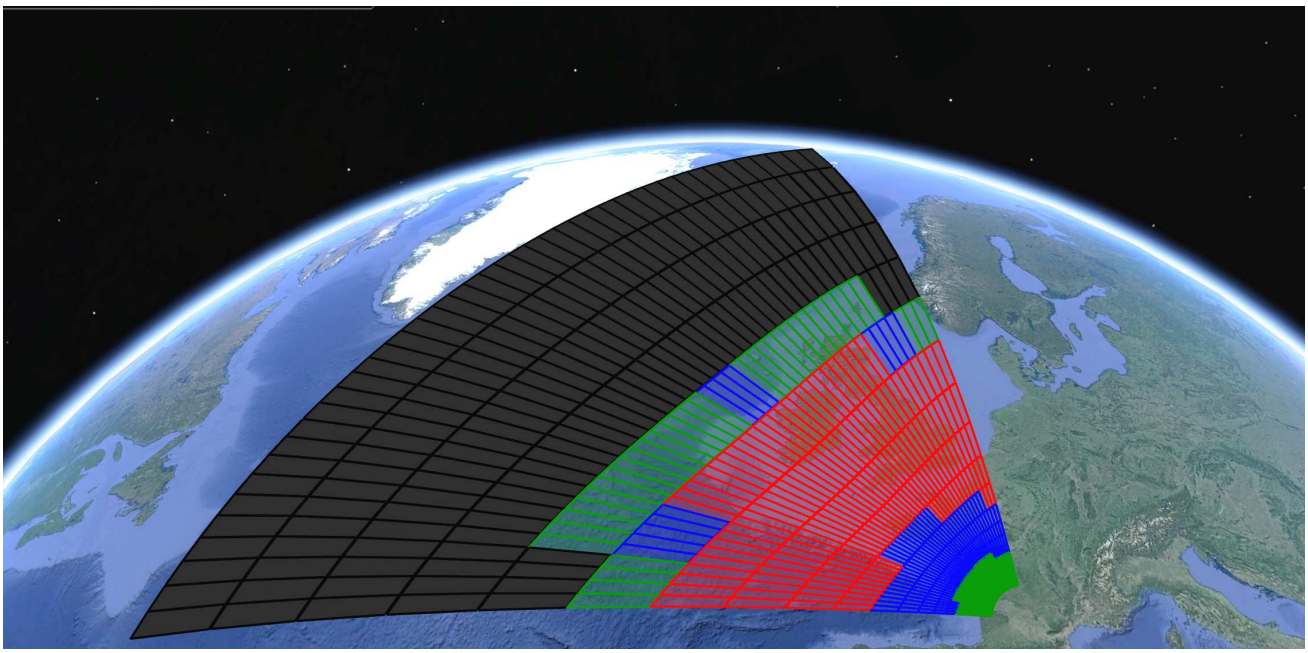

Figure 1 – Example of reduced area an the extreme case where the field of view partly intercepts the Earth surface (black cells). The color code indicates the relative value of the reduced area computed for each cell: green: low, blue: medium, red: high.

elevation might be slightly negative (up to a few degrees under the equivalent horizon for ground-based observations).

We have developed a software to compute the reduced area for each camera, given the features of the lens, nacelle altitude and pointing direction, by making an extensive use of SPICE (Acton et al., 2018) and astropy (Astropy Collaboration et al., 2018). Figure 1 shows an example of the result of such computation for an extreme but realistic case.

The program simulates the trajectory of the nacelles, computes the respective reduced areas for single and double-station observations, and provides the expected number of recorded meteors. In order to compare these simulations to reality, we consider real stratospheric observations of the 2016 GEM performed by Ocaña et al. (2019) and Ocaña (2017). Their videos are freely available (Sanchez de Miguel & Gomez, 2017). In particular, for records # 89-94 one can count up to $\sim$ 12 meteors for a video record of 1'45. In comparison, taking into account the camera LM and field of view, our software computed that 2.2 meteors should be detected in such a time duration.

3 Discussion

There is clearly a quite large discrepancy between the observed and the computed number of meteors from a stratospheric camera. Note that Molau et al. (2017a) deduced $ZHR \sim 350 hr^{-1}$ for ground-based camera observations, which is a factor of nearly 3 higher than from visual measurements. Molau et al. (2017) and Molau (2016) studies different factors that come in place for video detection of meteors. For example, the presence or absence of the Moon strongly influences the limiting magnitude. Rendtel and Koschack (2021) called for visual observations in order to better understand how it affects the estimated ZHR. Similarly, the population index strongly influences the number of detected meteors. Blaauw et al. (2016) did not find such large discrepancy for the Perseids. Recently, Richter (2021) questioned the assumption of constant r, or the naked eye limiting magnitude to be the same for stars and meteors. We leave it to more experienced observers to further study this topic. From this study, it appears, that there is clearly some much needed additional work to be performed in order to reconcile visual and video observations of meteors.

Acknowledgements

The MALBEC project is led and supported by IMCCE/Observatoire de Paris / PSL. This work is based on observations under a balloon operated by CNES, under the agreement between CNES and CNRS/INSU, within the MALBEC project. This work was supported by the Programme National de Planétologie (PNP) of CNRS-INSU co-funded by CNES. The weather data are made available via a research licence by MeteoFrance. We are especially grateful to CNES / Aire-sur-l'Adour stratospheric launch base facility staff.

This research made use of Astropy,[a] a community-developed core Python package for Astronomy (Astropy Collaboration et al., 2013; Astropy Collaboration et al., 2018). This work uses the following python3 librairies: spiceypy (Annex et al., 2020) and pygc (Wilcox, 2014).

This work made use of the SPICE toolkit developed by California Institute of Technology/Jet Propulsion Laboratory (Acton, 1996; Acton et al., 2018). We are especially grateful to Boris Semenov for his help in using the SPICE toolkit.

[a] `http://www.astropy.org`

References

Acton C., Bachman N., Semenov B., and Wright E. (2018). "A look towards the future in the handling of space science mission geometry". *Planetary and Space Science*, **150**, 9–12.

Acton C. H. (1996). "Ancillary data services of NASA's Navigation and Ancillary Information Facility". *Planetary and Space Science*, **44:1**, 65–70.

Annex et al. (2020). "SpiceyPy: a Pythonic Wrapper for the SPICE Toolkit.". *Journal of Open Source Software*, **5**. Online; accessed in 2020.

Astropy Collaboration, Price-Whelan A. M., SipHocz B. M., G"unther H. M., Lim P. L., Crawford S. M., Conseil S., Shupe D. L., Craig M. W., Dencheva N., Ginsburg A., Vand erPlas J. T., Bradley L. D., P'erez-Su'arez D., de Val-Borro M., Aldcroft T. L., Cruz K. L., Robitaille T. P., Tollerud E. J., Ardelean C., Babej T., Bach Y. P., Bachetti M., Bakanov A. V., Bamford S. P., Barentsen G., Barmby P., Baumbach A., Berry K. L., Biscani F., Boquien M., Bostroem K. A., Bouma L. G., Brammer G. B., Bray E. M., Breytenbach H., Buddelmeijer H., Burke D. J., Calderone G., Cano Rodr'iguez J. L., Cara M., Cardoso J. V. M., Cheedella S., Copin Y., Corrales L., Crichton D., D'Avella D., Deil C., Depagne E., Dietrich J. P., Donath A., Droettboom M., Earl N., Erben T., Fabbro S., Ferreira L. A., Finethy T., Fox R. T., Garrison L. H., Gibbons S. L. J., Goldstein D. A., Gommers R., Greco J. P., Greenfield P., Groener A. M., Grollier F., Hagen A., Hirst P., Homeier D., Horton A. J., Hosseinzadeh G., Hu L., Hunkeler J. S., Ivezić Ž., Jain A., Jenness T., Kanarek G., Kendrew S., Kern N. S., Kerzendorf W. E., Khvalko A., King J., Kirkby D., Kulkarni A. M., Kumar A., Lee A., Lenz D., Littlefair S. P., Ma Z., Macleod D. M., Mastropietro M., McCully C., Montagnac S., Morris B. M., Mueller M., Mumford S. J., Muna D., Murphy N. A., Nelson S., Nguyen G. H., Ninan J. P., N"othe M., Ogaz S., Oh S., Parejko J. K., Parley N., Pascual S., Patil R., Patil A. A., Plunkett A. L., Prochaska J. X., Rastogi T., Reddy Janga V., Sabater J., Sakurikar P., Seifert M., Sherbert L. E., Sherwood-Taylor H., Shih A. Y., Sick J., Silbiger M. T., Singanamalla S., Singer L. P., Sladen P. H., Sooley K. A., Sornarajah S., Streicher O., Teuben P., Thomas S. W., Tremblay G. R., Turner J. E. H., Terr'on V., van Kerkwijk M. H., de la Vega A., Watkins L. L., Weaver B. A., Whitmore J. B., Woillez J., Zabalza V., and Astropy Contributors (2018). "The Astropy Project: Building an Open-science Project and Status of the v2.0 Core Package". *The Astronomical Journal*, **156:3**, 123.

Astropy Collaboration, Robitaille T. P., Tollerud E. J., Greenfield P., Droettboom M., Bray E., Aldcroft T., Davis M., Ginsburg A., Price-Whelan A. M., Kerzendorf W. E., Conley A., Crighton N., Barbary K., Muna D., Ferguson H., Grollier F., Parikh M. M., Nair P. H., Unther H. M., Deil C., Woillez J., Conseil S., Kramer R., Turner J. E. H., Singer L., Fox R., Weaver B. A., Zabalza V., Edwards Z. I., Azalee Bostroem K., Burke D. J., Casey A. R., Crawford S. M., Dencheva N., Ely J., Jenness T., Labrie K., Lim P. L., Pierfederici F., Pontzen A., Ptak A., Refsdal B., Servillat M., and Streicher O. (2013). "Astropy: A community Python package for astronomy". *Astronomy and Astrophysics*, **558**, A33.

Bellot Rubio L. R. (1994). "Spatial number densities and errors from photographic meteor observations under very high activity.". *WGN, Journal of the International Meteor Organization*, **22:4**, 118–130.

Blaauw R. C., Campbell-Brown M., and Kingery A. (2016). "Optical meteor fluxes and application to the 2015 Perseids". *Monthly Notices of the Royal Astronomical Society*, **463:1**, 441–448.

Gural P. S. and Jenniskens P. (2000). "Leonid Storm Flux Analysis from One Leonid Mac Video AL50R". *Earth Moon and Planets*, **82**, 221–247.

Koschack R. and Rendtel J. (1990). "Determination of spatial number density and mass index from visual meteor observations (I).". *WGN, Journal of the International Meteor Organization*, **18:2**, 44–58.

Koschny D. and Zender J. (2000). "Comparing Meteor Number Fluxes from Ground-Based and Airplane-Based Video Observations". *Earth Moon and Planets*, **82**, 209–220.

Molau S. (2016). "Flux density, population index, perception coefficient, and the Moon". In Roggemans A. and Roggemans P., editors, *International Meteor Conference Egmond, the Netherlands, 2-5 June 2016*. page 185.

Molau S., Crivello S., Goncalves R., Saraiva C., Stomeo E., and Kac J. (2017a). "Results of the IMO Video Meteor Network - December 2016". *WGN, Journal of the International Meteor Organization*, **45:3**, 56–62.

Molau S., Crivello S., Goncalves R., Saraiva C., Stomeo E., and Kac J. (2017b). "Results of the IMO Video Meteor Network - May 2017, and flux density calculation". *WGN, Journal of the International Meteor Organization*, **45:6**, 144–148.

Ocaña F. (2017). *Techniques For Near-Earth Interplanetary Matter Detection And Characterisation From Optical Ground-Based Observatories*. PhD thesis, Universidad Complutense de Madrid.

Ocaña F., Sánchez de Miguel A., ORISON team, and Project D. (2019). "Balloon-borne video observations of Geminids 2016". In Rudawska R., Rendtel J., Powell C., Lunsford R., Verbeeck C., and

Knofel A., editors, *International Meteor Conference, Pezinok-Modra, Slovakia, 2018 August 30 - September 2*. pages 64–66.

Ocana F., McAuliffe J., and Koschny D. (2011). "Meteoroid spatial number density and flux calculation with video meteor observation. I.". In *Proceedings of the International Meteor Conference, 29th IMC, Armagh, Northern Ireland, 2010*. pages 76–80.

Rendtel J. and Koschack R. (2021). "Calibration of visual meteor observations". *WGN, Journal of the International Meteor Organization*, **49:5**, 120–122.

Richter J. (2021). "Simultaneous estimation of ZHR and the limiting magnitude correction factor". *WGN, Journal of the International Meteor Organization*, **49**, 35–41.

Sanchez de Miguel A. and Gomez M. A. (2017). "Geminids 2016 (part 1)". `https://doi.org/10.5281/zenodo.579708`.

Vaubaillon J., Egal A., Kwon M.-K., Marmo C., Birlan M., Jeanne S., Rault J.-L., Blanpain C., Lecubin J., Malgoyre A., Colas F., Bouley S., Caminade S., Vernazza P., Gattacceca J., and Zanda B. (2020). "FRIPIPE: the FRIPON pipeline". In *Proceedings of the 2019 International Meteor Conference, Bollmansruh*. pages 151–154.

Vaubaillon J., Koten P., Margonis A., Toth J., Rudawska R., Gritsevich M., Zender J., McAuliffe J., Pautet P.-D., Jenniskens P., Koschny D., Colas F., Bouley S., Maquet L., Leroy A., Lecacheux J., Borovicka J., Watanabe J., and Oberst J. (2015). "The 2011 Draconids: The First European Airborne Meteor Observation Campaign". *Earth Moon and Planets*, **114:3-4**, 137–157.

Vaubaillon J., Rietze A., and Zilkova D. (2021). "MALBEC: fine-tuning of the pointing direction of cameras for stratospheric double-station observation of meteor showers". *Monthly Notices of the Royal Astronomical Society*, **508:3**, 3897–3909.

Wilcox K. (2014). "pygc". `https://github.com/axiom-data-science/pygc`.

Zilkova D. and Vaubaillon J. (2019). "Estimating the flight path of a stratospheric balloon for meteor observations ". In *Meteoroids 2019 conference, poster # 17*.

Handling Editors: Francisco Ocaña González and Javor Kac
This paper has been typeset from a LaTeX file prepared by the authors.

Collection of micrometeorites in the stratosphere

Justína Nováková[1], *Michal Valíček*[2], *Andrej Buček*[3], *and Dušan Velič*[1,3]

A stratospheric balloon was launched to collect micrometeorites in the atmosphere up to 32 km. For this mission, a collector module with an aerodynamic funnel was specially designed. Adhesiveness of samples to two surfaces was tested – the rough side of a silicon wafer and the carbon tape. The collected particles were analysed using several techniques, such as SEM, SIMS, and EDX. Similarities with carbonaceous chondrites and previously reported interplanetary dust particles were evaluated. Overall, three micrometeorite candidates were found in this mission and confirmed by the analysis. Future missions with emphasis on evasion of contaminants during ascent in the lower stratosphere are prepared.

Received 2021 October 26

This work has been presented at the International Meteor Conference 2021 (held online).

1 Introduction

Micrometeorites (MMs) are dust particles with sizes ranging from 30 µm to 1000 µm accreted by Earth's atmosphere. Their chemical composition is usually very similar to carbonaceous chondrites (CCs) (Genge et al., 1997). However, MMs differing in composition from any known meteorites, enriched in particular with volatile elements can also be found (Rietmeijer, 2001). Morphologically, MMs can be divided into three groups - melted (cosmic spherules), partially melted (scoriaceous), and unmelted (aggregates) (Genge et al., 2008). Analysis of morphology is the first to be addressed when identifying MMs, however it is seldom unambiguous. In particular, cosmic spherules can be easily mistaken for anthropogenic dust particles from industrial factories. For this reason, a petrological or chemical study has to follow for correct identification of MMs.

The largest stratospheric collections were made by NASA in 1960 to 1982. These missions were performed using large aircrafts with aerosol traps, through which a large volume of air was pumped for several hours. However, in the last few decades, targeted surface collections of micrometeorites are more usual, such as deep-sea sediments filtration (Brownlee, 1985), melting of Antarctic ice and snow (Maurette et al., 1991), and filtration of loose sediments from Transantarctic mountain. More recently, collections from large area rooftops were carried out by Genge et al. (2017). Depending on the surrounding conditions, different samples are collected. Collections from deep-sea sediments served as first building-blocks for a systematic study of micrometeorites by Brownlee et al. (1994). These samples are usually heavily weathered due to the presence of salt water, which is why cosmic spherules enriched in Fe are usually found. On the other hand, samples from polar regions experiences little to no weathering. These collections consist of large numbers of cosmic spherules, as well as unmelted MMs.

The origin of our balloon project started a few years ago by the idea of Juraj Tóth (private communication). He suggested to try in-situ sampling of meteoritic particles over Slovakia, where AMOS network is monitoring meteor activity. Stratospheric sampling of specific meteor showers or bright fireballs would be the ultimate goal of the project. On 13th September 2020, we attempted a stratospheric collection of dust particles (flight of KVÚ I.), with a subsequent morphological and chemical analysis. In this report, we describe the collecting apparatus, which we designed, and the analytical steps, which led us to identifying three possible micrometeorite samples. The emphasis for the first design lay on the low-cost of manufacturing.

2 Materials and methods

A stratospheric balloon for a 1200 g load was used. Underneath the balloon, the collection module, the electronics, and the collection module were suspended.

2.1 Collection module

The collection module is a 150 × 150 × 150 mm^3 cube, printed on the 3D printer Prusa i3MK2S MMU1 3D from PETG material. The 3D model of the module is shown in Figure 1. At the edges, dural tubes hold the construction together. Carbon tubes are inserted into the device's top cover, and onto them, an aluminium plated PET foil is fastened. The top and bottom covers have a spiral ventral opening, to ensure good air flow in and out of the device.

Inside the module, a silicon wafer is fastened onto a round holder. Half of the silicon wafer is covered with carbon tapes, the other half is the bare rough side of the silicon wafer, to test the adhesiveness of dust particles to different surfaces. On one side of the holder, a hole is drilled for magnet placement, to enhance collection of magnetic dust particles.

2.2 Electronics

Communication with the balloon during flight is ensured by the radio-probe. The radio-probe is controlled by the Arduino microcomputer, which is responsible for communication with different components, such as U-blox GPS, digital thermometer, SD card, and APRS

[1]Faculty of Natural Sciences, Comenius University in Bratislava, Ilkovičova 6, 84208 Bratislava, Slovakia.
Email: justina.novakova@trojsten.sk
[2]Faculty of informatics and information technologies, Slovak University of Technology, Ilkovičova 2, 84216 Bratislava, Slovakia.
[3]International laser centre of SCSTI, Ilkovičova 3, 84104 Bratislava, Slovakia.

IMO bibcode WGN-496-novakova-micrometeorites
NASA-ADS bibcode 2021JIMO...49..190N

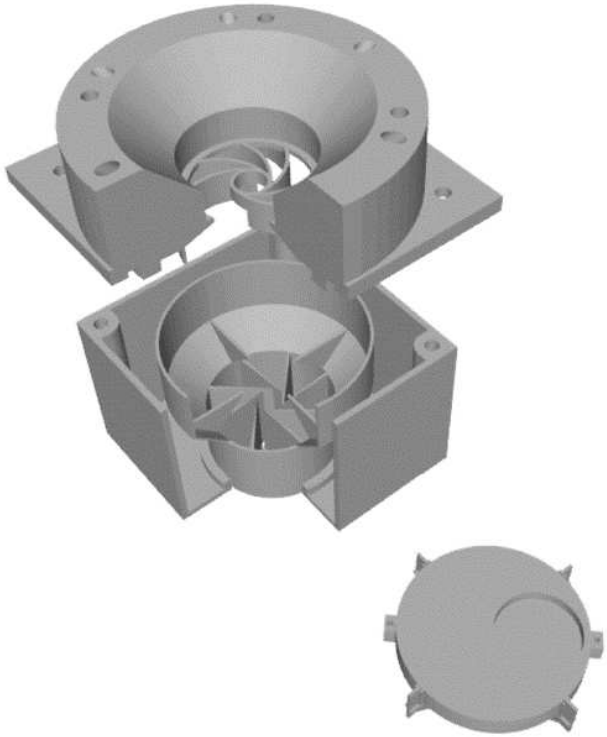

Figure 1 – 3D model of the collection module KVÚ I.

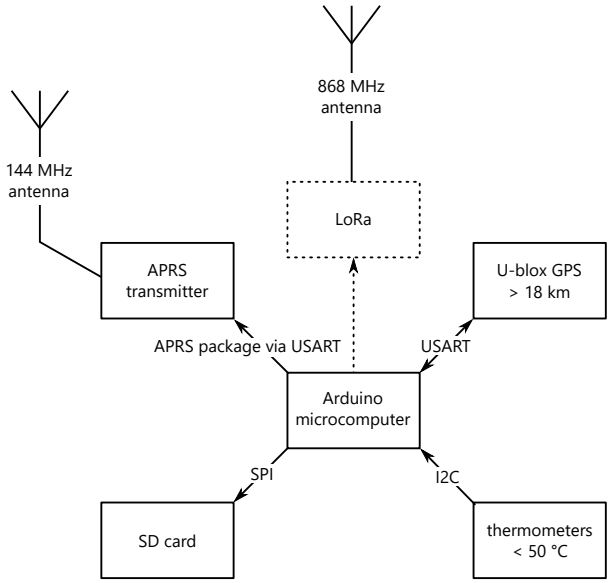

Figure 2 – Schematic view of the radio-probe of KVÚ I. All information (GPS location, temperature) is sent into the Arduino microcomputer. The Arduino saves this information on the SD card, and generates an APRS data package, which is then sent via the APRS transmitter every two minutes at 144.8 MHz.

transmitter. The radio-probe is also responsible for saving all data on the memory card. It is charged by a Li-Ion battery with suitable discharge characteristic in low temperatures. A schematic view of the radio-probe is shown in Figure 2.

The U-blox GPS sends information about the balloon's location periodically into the microcomputer via USART. U-blox GPS modules provide different operating regimes including flight modes working even above 18 km (still following the boundaries by limiting the output by maximum speed). The digital thermometer with a temperature range of ±50°C sends information to Arduino by I2C.

The microcomputer generates an APRS data package from all the received information. This package is then sent into the APRS transmitter, connected to a laminate antenna, used for its low weight. A new data package is transmitted every two minutes at 144.8 MHz and received by the network of APRS digipeaters and internet gates operated by radio amateurs. However, it gets deformed during the flight, which may result in transmission errors. To avoid information loss, the microcomputer saves simultaneously all information on the SD card, which is a back-up for all files going through the microcomputer. All electronic components are enclosed in a polystyrene box to keep them in the range of operating temperatures.

2.3 Flight

On 13th September 2020, the stratospheric mission KVÚ I. took off from Partizánske airport (central Slovakia, +48.61949° N, 18.33024° E). A small balloon filled with 3.6 m^3 of helium was used. Due to changing pressure, the balloon extended from 2 m at the ground level to 10 m at 32 km altitude, where it burst. During the flight, the radio-probe was recording telemetric data (altitude, velocity, inside and outside temperature, GPS). These data are depicted in Figure 3.

The solid gray line represents the changing altitude, the dotted black line represents the almost constant velocity during ascension (from 2 $m\,s^{-1}$ to 5 $m\,s^{-1}$). After the bursting of the balloon, the module fell with a velocity of ≈ 42 $m\,s^{-1}$. When it reached the troposphere, (≈ 18 km) the higher air density slowed the fall velocity to 10 $m\,s^{-1}$ to 5 $m\,s^{-1}$. The outside temperature, represented by the dashed gray line, decreased under the thermometer range of −50°C. The inside temperature, represented by the dash-dotted gray line, did not decrease below −16°C. Therefore, the polystyrene box

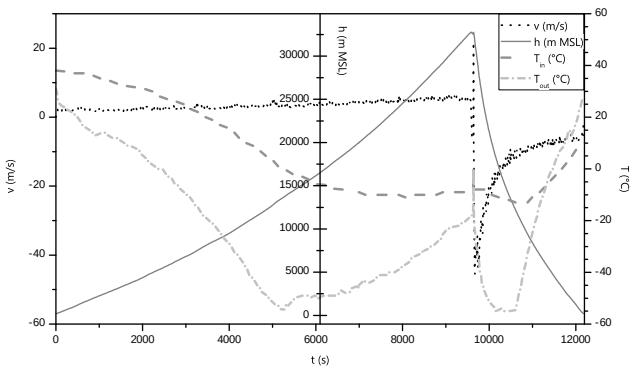

Figure 3 – Data on the altitude (gray solid line), outside and electronics temperature (dot-dashed and dashed gray lines), and module velocity (black dotted line). The outside temperature exceeded the thermometer's temperature range, therefore the data after cca 12 500 m altitude do not correspond to real temperatures.

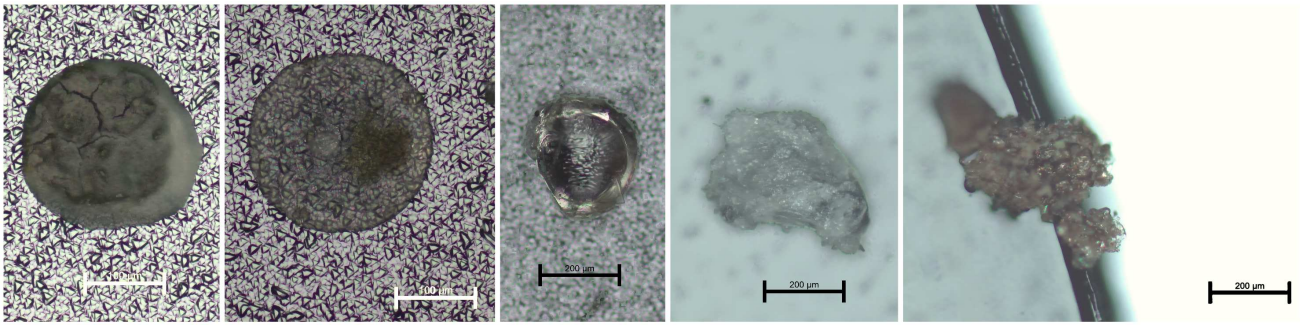

Figure 4 – Photographs of the five samples selected for further analysis after the morphological study under optical microscope.

proved to be useful in protecting the electronics. The last radio-probe signal was sent from 224^{m}AMSL.

The collection module was found near the town Beša (South of Slovakia, 48.14433° N, 18.40363° E). The module was disassembled on site, and the silicon wafer holder with samples was placed into a desiccator to avoid further contamination.

3 Identification of micrometeorites

Three different analytical techniques were used to isolate samples from contaminants. First, a morphological study was performed, using an optical microscope Axiocam 20B color (Zeiss). Based on their morphology five samples were selected for further analysis – three spherules with glossy surface (samples 01–03), and two irregularly shaped particles (samples 04 and 05). The samples are depicted in Figure 4.

Sample 01 bears thin cracks on the surface, very similar to known cosmic spherules. Samples 02 and 03 are semi-transparent. Sample 02 has a small inclusion on top. Sample 03 has only a transparent shell, with a darker nuclei visible beneath. Sample 04 is a relatively large particle, around 400×400 µm^2, with very glossy surface. Sample 05 is an aggregate of many smaller particles, which appear to be yellow-brownish minerals. This particle is about 400 µm long and 200 µm wide.

Following the morphological study, two techniques were used for sample characterization – Secondary Ion Mass Spectrometry (SIMS) and Energy Dispersive X-ray Spectroscopy (EDX) equipped with Scanning Electron Microprobe (SEM).

3.1 SIMS analysis

The SIMS analysis is qualitative, i.e. it does not provide information on the quantity of the identified elements and molecules. However, it is a tool with high mass resolution, up to $m/\Delta m = 1000$. With SIMS, it is possible to identify elements in the range of 0 u to 10000 u. Although the quantity of elements is not preserved, the relative ratio of any element's isotopes is conserved.

After the characterization by SIMS, sample 04 was removed from further analysis by EDX spectroscopy. It was concluded, that this sample is heavily contaminated, and contains mostly organic compounds uncommon for micrometeorite samples, with very little mineral components.

In the last few years, we established a Convolutional Neural Network (CNN) (Novakova et al., 2020), which works with data from SIMS. Specifically, data from six different carbonaceous chondrites (CCs) were learned by this CNN, and compared with data from the five possible micrometeorite samples. Results of this analysis can be seen in Table 1.

As can be seen from Table 1, spectra of samples 02 and 03 are in good agreement with the spectra of two of the CCs. Sample 01 spectra are slightly similar to two of the CCs. Likewise, spectra of sample 05 show some similarity with one of the CCs. However, these are not conclusive and the samples need to be further characterized.

3.2 SEM-EDX analysis

The SEM-EDX is a high-precision analysis for quantification of elemental composition. Moreover, the electron microprobe can be used for a better understanding of the surface structure of the sample.

First, additional information about the structure of sample 01 was evaluated. It showed a flaky composition on the SEM, as shown in Figure 5. Therefore, it was removed from the possible micrometeorite candidates.

Table 1 – Evaluation of similarity between the positive polarity spectra of six carbonaceous chondrites and four potential micrometeorite samples.

	similarity evaluation / %					
sample	Moss	NWA6604	NWA7184	NWA8038	NWA8040	Sue003
01	0.00	**56.95**	0.00	**42.49**	0.55	0.00
02	0.02	**88.87**	0.00	10.51	0.34	0.00
03	0.06	0.79	0.63	**93.60**	0.85	3.11
05	0.65	18.25	2.46	**55.36**	8.71	1.95

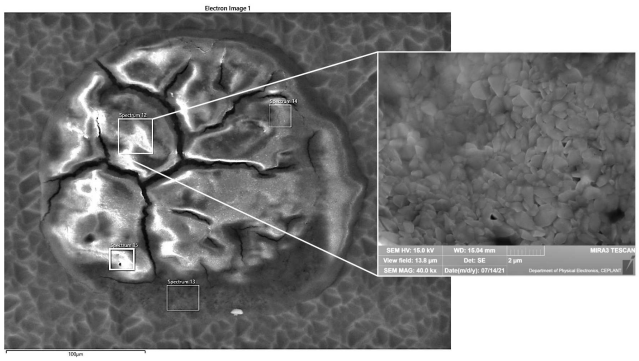

Figure 5 – SEM photograph of sample 01, where the flaky structure of the sample surface is visible.

The data from the EDX analysis for the three samples (02, 03, 05) were compared with the Standard Abundance Distribution (SAD) of the Solar System. The data of the possible micrometeorite candidates should be consistent with the SAD within a factor of three. For samples 02 and 05, these values were consistent, but not for all the elements. For sample 03, it was impossible to perform the SEM-EDX, because of the charging of the sample. We attempted to coat this sample in Au-Pd (80/20). However, during this procedure, the sample surface reacted with the coating, and it was impossible to evaluate the data.

To have conclusive evidence about the origin of the sample 05, we tried to search through literature for data of already verified micrometeorites or Interplanetary Dust Particles (IDPs). Thomas et al. (1992) reported on the bulk composition of six IDPs from NASA/JSC cosmic dust catalogues. The bulk composition of the sample 05 is similar of one of the particles, L2005R7, as seen in Table 2.

There is a large discrepancy of the amount of carbon, as well as calcium in our sample compared to the L2005R7 particle. The high carbon content can be explained by the presence of carbon tapes on the silicon wafer, as the sample 05 was found on one of the carbon tape's edges. The high calcium content is most probably due to the contamination from atmospheric aerosols.

4 Conclusion and future research

The collection module we designed and launched proved capable of collecting dust particles in the stratosphere. We reported the recovery of three possible micrometeorite candidates, which were thoroughly characterized by optical microscopy, SIMS analysis, and SEM-EDX analysis. The data acquired from SIMS were compared with six carbonaceous chondrites from different CC groups. The comparison was performed within a CNN. Further analysis from SEM-EDX confirmed the results from our CNN.

Table 2 – Comparison of compositions of the sample 05 and the IDP L2005R7, as reported by Thomas et al. (1992). Elemental ratios are given relative to the silicon abundance.

ratio	C/Si	Mg/Si	S/Si	Ca/Si	Fe/Si	Ni/Si
L2005R7	1.1	0.7	0.1	0.01	0.5	0.02
S05	25.37	0.20	0.11	0.31	0.33	0.02

One of the issues we came across is the contamination by carbon tape. Although not all samples were found on the taped half of the silicon wafer, it was impossible to evaluate the carbon peaks in any of the samples, as each sample probably came into contact with the carbon tape. Therefore, the question of using the carbon tape has to be addressed before each flight, depending on the analytical technique to be used when identifying samples after the collection. In the case of using SIMS coupled with CNN, this issue was not a problem, as it is possible to ignore the carbon isotope peaks in every spectrum (trained, as well as compared), and evaluate only the other elemental features. This treatment is possible as a part of data preprocessing, if there is a suspicion, that the network is malfunctioning due to carbon peak bias.

The vital part of a stratospheric dust collection mission is the analytical procedure after the flight. We conclude, that access to at least two independent analytical techniques is necessary for unbiased conclusions, because the data from one analysis may not necessarily by unambiguous, as was the case with samples 03 and 05.

The main struggle of the first KVÚ mission was the optical microscopy analysis. It proved to be more time-consuming than expected, mainly due to a large number of objects captured on the silicon wafer, most of which are contaminants from troposphere and lower stratosphere. To avoid most of these objects, a shutter was designed and printed for the KVÚ II. mission. The shutter should open automatically at 25 km, which should allow us to evade most of these 'junk' objects. A fisheye camera should be mounted above the collection module to monitor the correct opening and closing of the shutter.

For the KVÚ I. and KVÚ II. designs, the collection only during the ascension of the balloon is expected. The first reason is that there is not enough space for a double sided wafer, and a design in which the whole module with funnel should flip is too challenging. Moreover, after the bursting of the balloon, a large amount of dust will be released and will surround the module. Therefore, to avoid contaminants as much as possible, only an ascending collection is considered. A possibility to collect during ascent as well as during descent is one of the possible arrangements for a KVÚ III. mission.

5 Acknowledgments

This work was supported by the Comenius University grant G-21-122-00. The authors would also like to thank the colleagues from the International laser center, Monika Jerigová, Miroslav Michalka, and Jaroslav Bruncko, as well as the colleagues from CEPLANT at Masaryk University, Jana Jurmanová and Michael Kroker for allowing access to the analytical tools. Last but not least, our thanks belong to Juraj Tóth and Dušan Lorenc for the article revision and useful critique and comments.

References

Brownlee D. E. (1985). "Cosmic dust: Collection and research". *Annual Reviews of Earth and Planetary Sciences*, **13**, 147–173.

Brownlee D. E., Bates B. A., and Schramm L. S. (1994). "The elemental composition of stony cosmic spherules". *Meteoritics and Planetary Science*, **32**, 157–175.

Genge M. J., Engrand C., Gounelle M., and Taylor S. (2008). "The classification of micrometeorites". *Meteoritics and Planetary Science*, **43:3**, 497–515.

Genge M. J., Grady M. M., and Hutchison R. (1997). "The textures and compositions of fine-grained antarctic micrometeorites – implications for comparisons with meteorites". *Geochimica et Cosmochimica Acta*, **61**, 5149–5162.

Genge M. J., Larsen J., Van Ginneken M., and Suttle M. D. (2017). "An urban collection of modern-day large micrometeorites: Evidence for variations in the extraterrestrial dust flux through the quaternary". *The Geological Society of America*, **45:2**, 119–122.

Maurette M., Olinger C., Michel-Levy M. C., Kurat G., Pourchet M., Brandstatter F., and Bourot-Denise M. (1991). "A collection of diverse micrometeorites recoveref from 100 tonnes of antarctic blue ice". *Nature*, **351**, 44–47.

Novakova J., Jerigova M., Jane E., Szoecs V., and Velic D. (2020). "Secondary ion mass spectrometry as an advanced tool for meteorite classification". *Planetary and Space Science*, **192**, 105012.

Rietmeijer F. J. M. (2001). "Interplanetary dust particles". In Papike J. J., editor, *Planetary Materials*, volume 36.

Thomas K. L., Keller L., Flynn G., Sutton S. R., Takatori K., and McKay D. S. (1992). "Bulk compositions, mineralogy, and trace element abundances of six interplanetary dust particles". In *23rd Lunar and Planetary Science Conference*.

Handling Editors: Francisco Ocaña González and Javor Kac
This paper has been typeset from a LaTeX file prepared by the authors.

Reconstructing meteoroid trajectories using BRAMS data

Hervé Lamy[1]*, Joachim Balis, Michel Anciaux*

This paper summarizes our recent efforts in retrieving meteoroid trajectories using data from the forward scatter radio system BRAMS. Two methods are presented, one based only on the knowledge of time delays measured between meteor echoes observed at various receiving stations, and one including information from a radio interferometer in addition to the time delays measurements. For comparison about the quality of trajectory reconstruction, data from the optical CAMS-BeNeLux network are used. A third method is briefly presented assuming the total range traveled by the radio wave is known at all receiving stations. This work contains only preliminary results available at the end of summer 2021. Discussions about improvements are provided at the end of the paper.

Received 2022 January 10

This work has been presented at the International Meteor Conference 2021 (held online).

1 Introduction

The BRAMS (Belgian RAdio Meteor Stations) network is a Belgian project using forward scatter of radio waves to detect and characterize meteoroids. It comprises a dedicated transmitter located in the South-West of Belgium and 38 receiving stations spread all over the Belgian territory and neighbouring countries (see Figure 1 for status in September 2021).

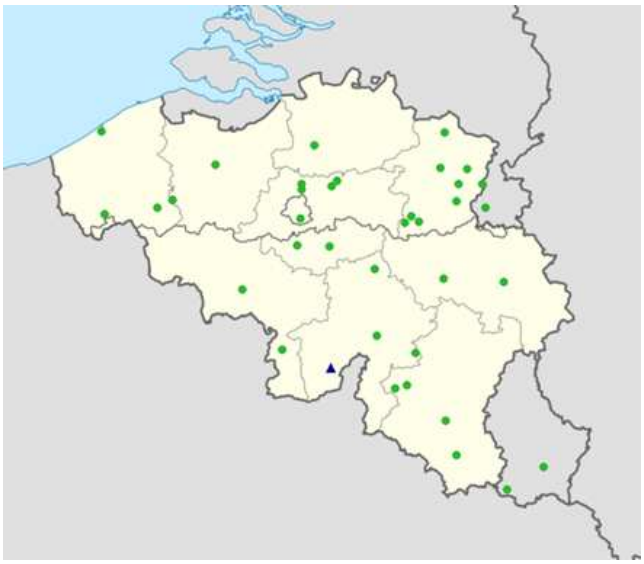

Figure 1 – Map of the BRAMS network in September 2021. The blue triangle is the transmitter located in Dourbes while the green dots are the 38 active receiving stations at the time.

The transmitter emits a circularly polarized continuous radio wave with no modulation at a frequency of 49.97 MHz with a power of 130 watts. All the receiving stations are using a 3-element Yagi antenna set-up vertically and trained in azimuth on the transmitter. In September 2021, approximately half of the receiving stations were using analog ICOM-R75 receivers, an external sound card to sample the signal coming from the receiver, and were controlled by the freeware program Spectrum Lab running on a Windows PC (see e.g. Lamy et al., 2015). The other half uses digital SDR-RSP2 receivers controlled by a Linux system running on a Raspberry Pi (Anciaux et al., 2020). All stations are equipped with a Garmin GPS that provides timestamps to the BRAMS data and allows a time synchronization between the receiving stations. Additional features of the receiving stations are not described here and we refer the reader to previous publications in the Proceedings of the IMC. A paper is also in preparation to describe the BRAMS network and data in full detail.

One of the difficulties with forward scatter systems is the determination of individual meteoroid trajectory and speed as the geometry is more complex than in the case of backscatter systems. In the specific case of BRAMS, the absence of modulation in the CW transmitted signal does not allow to estimate the total range traveled by the radio wave between the transmitter (Tx), the reflection point and the receiver (Rx), and therefore makes the problem even more complex. We present here an attempt to retrieve meteoroid trajectories using BRAMS data. Two methods are considered: one based only on measurements of time delays between meteor echoes recorded at different receiving stations, and one using the same data but complemented with data from the radio interferometer located in the Humain station which provides the direction of one specular reflection point. A (currently) hypothetical method is also presented assuming that the total range traveled by the radio wave is known for all receiving stations. In order to assess the quality of the reconstruction, a comparison with data from the CAMS-BeNeLux network is provided.

2 Two methods to determine meteoroid trajectory and speed

The first method (hereafter called Method 1) is based purely on geometrical considerations and relies on the specularity condition of the reflection of the radio wave. The specular reflection point is the point along the meteoroid path for which the total distance traveled by the radio wave is minimum, which means that the total distance $S_i = R_{Ti} + R_{Ri}$ must be minimum for each receiving station i. Because the geometry Tx-

[1]Royal Belgian Institute for Space Aeronomy, Brussels, Belgium. Email: herve.lamy@aeronomie.be

IMO bibcode WGN-496-lamy-trajectories
NASA-ADS bibcode 2021JIMO...49..195L

Trajectory number	Date	T_{beg} hh:mm:ss	V_∞ km/s	X_{Hum} km	Y_{Hum} km	Z_{Hum} km
79	29/07/2020	23:14:00	41.96	45.24	57.95	95.37
105	29/07/2020	23:36:28	41.83	122.45	93.60	99.97
149	30/07/2020	00:17:18	26.45	−89.21	92.87	89.48
188	30/07/2020	00:51:27	29.95	−52.92	21.33	88.48
282	30/07/2020	01:44:28	40.59	−96.02	35.01	88.70
477	30/07/2020	22:07:58	61.36	−80.56	7.74	102.12
532	30/07/2020	22:56:54	36.90	39.56	50.58	92.07
536	30/07/2020	23:06:55	65.07	22.62	199.53	106.10
598	30/07/2020	23:43:54	70.46	6.91	158.72	103.19
654	31/07/2020	00:21:21	15.49	67.98	10.19	80.15
709	31/07/2020	00:48:40	63.70	−32.89	108.71	95.53
773	31/07/2020	01:25:38	65.68	−94.82	62.32	96.97

Table 1 – Selected CAMS trajectories used for comparison with the reconstructed trajectories using BRAMS data. T_{beg} is the begin time of the visual CAMS observation. V_∞ is the speed of the meteoroid at the top of the atmosphere. X_{Hum}, Y_{Hum}, and Z_{Hum} are the coordinates of the specular reflection point for the Humain station in a Cartesian referential centered on the Dourbes transmitter. X is directed East-West and counted positive towards East, Y is directed North-South and counted positive towards North.

Rx_i is different for each receiving station Rx_i, the corresponding reflection points will be located at various positions along the meteoroid path. This is illustrated in Figure 2 for a reference station Rx_0 and another station Rx_i. In this example, the specular reflection point P_0 for the reference station is created before the corresponding reflection point P_i. The distance between the two points depends on the speed of the meteoroid which is here assumed constant. As a consequence, the reference station will detect a meteor echo shortly before receiving station i, the time delay between meteor echoes depending on the meteoroid path and speed.

A meteoroid trajectory can be defined by the 3D Cartesian coordinates of one point (the one corresponding to a reference station) and the three components of the velocity which provides the direction (assuming again a constant speed). This gives a total of six unknowns (respectively called X_0, Y_0, Z_0, v_x, v_y and v_z) and therefore the need to have at least six equations. In Method 1, these equations are provided by the fact that the total derivative, dS_i/dt, must be equal to 0 for at least six stations $i = 1, \ldots, 6$. The mathematical details will be provided elsewhere. This leads to a set of ≥ 6 non-linear equations which contains the 6 unknowns and the time delays Δt_i between meteor echoes recorded at station i and the reference station. A non-linear solver must then be used to solve this set of equations and to take into account additional constraints on the unknowns, such as the height of all reflection points which must lie between e.g. 85 and 110 km altitude, or the speed of the meteoroid which must be larger than ~ 11 km/s.

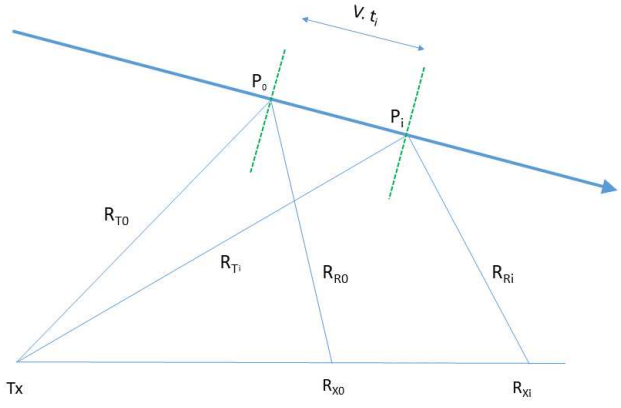

Figure 2 – Geometry of the problem for Method 1.

Note that a similar technique has been developed recently for CMOR (Mazur et al., 2020) but the authors use two additional assumptions that simplify the set of non-linear equations. The first is that the reference receiving site is a backscatter system, which leads to the condition $\vec{r_0}.\vec{v} = 0$ where $\vec{r_0}$ is the vector linking the transmitter to the reference reflection point. The second assumption is that the remote sites are rather close to the transmitter (distances $\leq$ 20 km). These two assumptions allow to simplify the set of non-linear equations into a set of linear equations for only the 3 components of the velocity. Unfortunately, neither of these assumptions are valid for the BRAMS network and we have therefore to solve the complete set of non-linear equations.

The second method (hereafter called Method 2) is using the same assumptions as Method 1 but includes data from our interferometric radio station located in Humain. Unlike the other receiving stations, it uses 5 antennas in the so-called Jones configuration (Jones et al., 1998; Lamy et al., 2018) and allows to determine the direction of arrival of the meteor echo to within approximately 1°. The interferometer provides two more equations for the azimuth and elevation of the specular reflection point but does not provide its exact position. With these additional equations, we only need time delays measured between 3 additional stations and a reference station in order to get at least 6 equations.

3 Validation procedure

To validate the reconstruction of the trajectory using BRAMS data and Method 1 or 2, optical data com-

ing from the CAMS BeNeLux network are used (Jenniskens et al., 2011; Roggemans et al., 2016). BIRA-IASB is a member of this network and provides daily data from 4 cameras. Data were provided for 2 clear consecutive nights from 29 to 31 July 2020, in a period without any strong activity from meteor showers. Among the 948 available trajectories, a selection was made based on the following criteria : (i) most of the trajectories are not located above Belgium and therefore not geometrically suitable to be detected by our BRAMS receiving stations, (ii) each trajectory must be detected by at least 6 stations, otherwise we reject it, (iii) because we want to compare Methods 1 & 2, one of these stations must be the interferometer in Humain, and (iv) we restrict ourselves as much as possible to underdense meteor echoes in order to ensure that the specularity condition is valid. The application of these criteria resulted in a selection of 12 suitable CAMS trajectories. The parameters of these trajectories are summarized in Table 1.

The three coordinates of the reflection point for the reference station in Humain are computed knowing the trajectory (e.g. Lamy et al., 2016). Together with the 3 velocity components (projections of V_∞ along the trajectory, from CAMS data, onto the reference frame centered on Dourbes), they constitute our six unknowns to retrieve the meteoroid trajectory and speed.

4 Determination of time delays

In the frame of the BRAMS network, the only measurements available are the time delays measured between the start of a meteor echo at various receiving stations and that at the reference station. The start of the meteor echo is chosen as the time when it rises to half the peak power. This should indeed correspond to the instant at which the specular reflection occurs. This process is done using only underdense meteor echoes, which therefore avoids using a possible additional larger maximum later on in the case of an overdense meteor echo.

Meteor echoes are first identified in the BRAMS spectrograms based on their approximate expected time of appearances which correspond to the passage of the meteoroid at the reflection points. These times are computed based on the initial time and height of the CAMS trajectory, and on the speed of the meteoroid. A visual inspection was done for this study to avoid selecting another meteor echo randomly appearing at approximately the same time. An automatic procedure is planned for this task in the future. Once the meteor echoes have been identified in the spectrograms, their frequency range can be computed automatically (see top panel of Figure 3). If this frequency range contains the frequency of the direct signal coming from the transmitter, the latter is first reconstructed using a local (i.e. computed every 5 seconds) FFT and then subtracted from the raw data (see middle panel of Figure 3). A Blackman filter of high order is then used to remove the noise at frequencies where the meteor echo does not appear. After these two steps, an accurate determination of the start of the meteor echo can be computed on the power profile (see bottom panel of Figure 3).

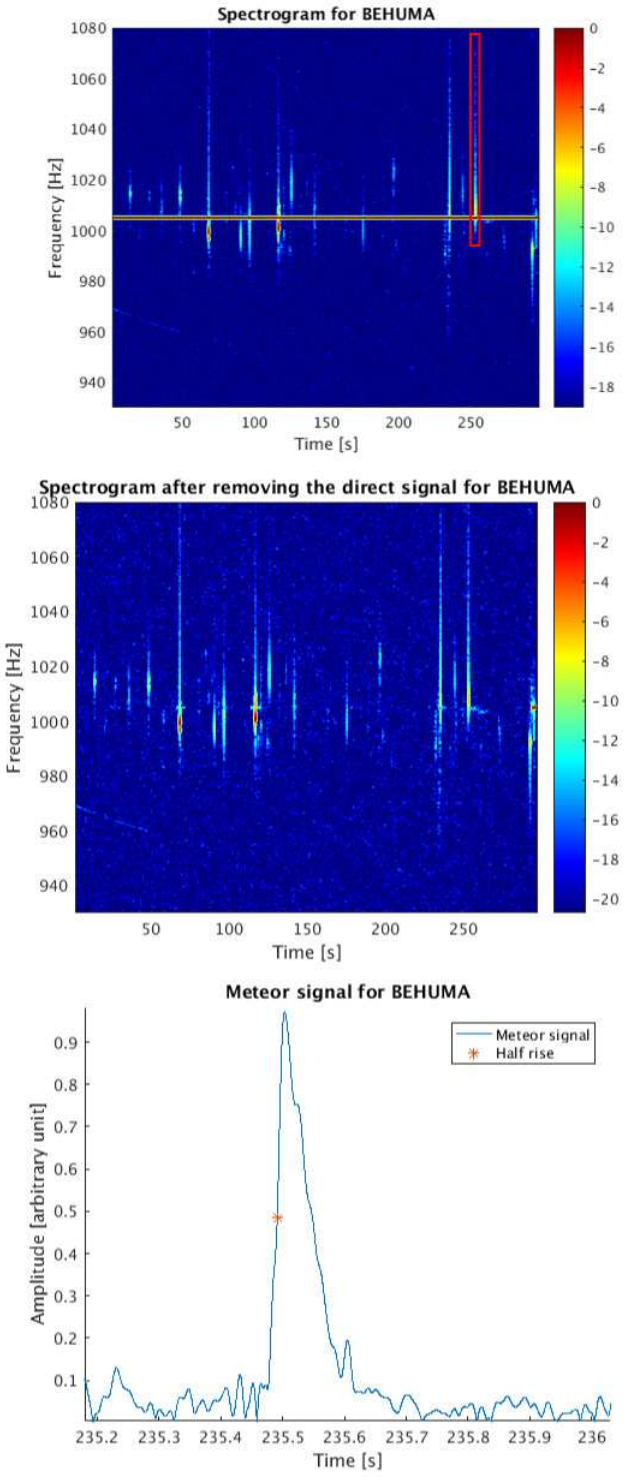

Figure 3 – Top Panel: Example of one meteor echo corresponding to CAMS trajectory 598 detected in the spectrogram of Humain (red rectangle). Middle Panel : same spectrogram obtained after subtracting the reconstructed direct signal coming from the transmitter from the raw data. Bottom panel : power profile of the meteor echo obtained after filtering all frequencies not included in the red rectangle. The time corresponding to half-peak power in the rising edge of the echo is marked.

5 Preliminary results

The results presented here were obtained during a master thesis organized at the University of Liège with supervision from the BRAMS team, and represent the work in progress on this topic at the time of the online International Meteor Conference organized in September 2021.

Codes were written in Matlab. The solver used to resolve the set of non-linear equations described in Section 2 was "lsqnonlin" which searches for the set of unknowns that minimizes the sum of the squares of the non-linear equations $dS_i/dt = 0$. This approach was not completely appropriate as this solver does not allow the application of constraints on some of the parameters (height of the specular reflection point and total speed of the meteoroid) in a simple way. Moreover, the target objective trying to minimize the total distances traveled by the radio waves proved to not be effective enough.

As a result, Method 1 using only time delays failed as illustrated on Figure 4 for trajectory 105. This figure presents the projected CAMS trajectory as well as the reconstructed one in the horizontal XY plane and in the vertical XZ plane, where coordinates X,Y, and Z are given in a local Cartesian frame centered on Dourbes. It can be seen that the position of the specular reflection point for the reference station in Humain is completely wrong. The direction of the trajectory (velocity vector) is also very inaccurate although closer to the correct one. This behavior was similar for all other trajectories listed in Table 1.

Figure 5 presents the results obtained for trajectory 105 in the same horizontal and vertical planes but using Method 2. Since the direction of the reflection point is constrained via equations including the interferometer data, it is now correctly retrieved and this helps greatly the reconstruction of the trajectory. The altitude of the reflection point is still not accurate enough with an error of a few kilometers. The speed direction is accurate to 1.5° and the magnitude (40.7 km/s) is close to the one measured by CAMS (41.8 km/s). Note that CAMS includes a deceleration model that is not taken into account here. However, the CAMS deceleration parameters were small for trajectory 105.

Although the results are not accurate enough yet, they are encouraging. The results obtained with Method 2 for all 12 trajectories considered for this study are presented in Figure 6. Trajectory 105 is on the right side of this figure. The conclusions for most of the trajectories are identical to those presented for trajectory 105: velocity magnitude and direction are rather close to the CAMS measurements. The altitude of the reconstructed reflection point is slightly different from the position calculated on the CAMS trajectory. This difference depends on the elevation of the specular reflection point.

6 Discussions and perspectives

Method 1 is very important since it is the only one that can be applied to all archived BRAMS data of the last 10 years. Improvements such as the use of a more appropriate solver, the use of a better target objective, etc, have been considered since the IMC2021 and will be presented in a forthcoming paper. Method 2 works already much better, even at this stage of development, but cannot be applied to a lot of data since it requests to have at least 3 stations detecting the same meteor as the interferometer located in Humain. The number of receiving stations close to Humain is rather low and priority will be given to searching new locations nearby to welcome future BRAMS stations. Another priority will be to install new receiving stations to create lo-

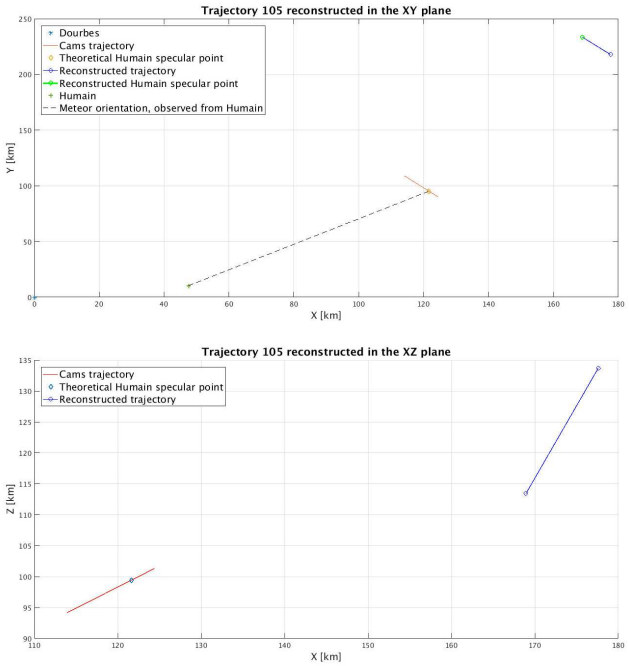

Figure 4 – Example of result obtained for CAMS trajectory 105 using Method 1.

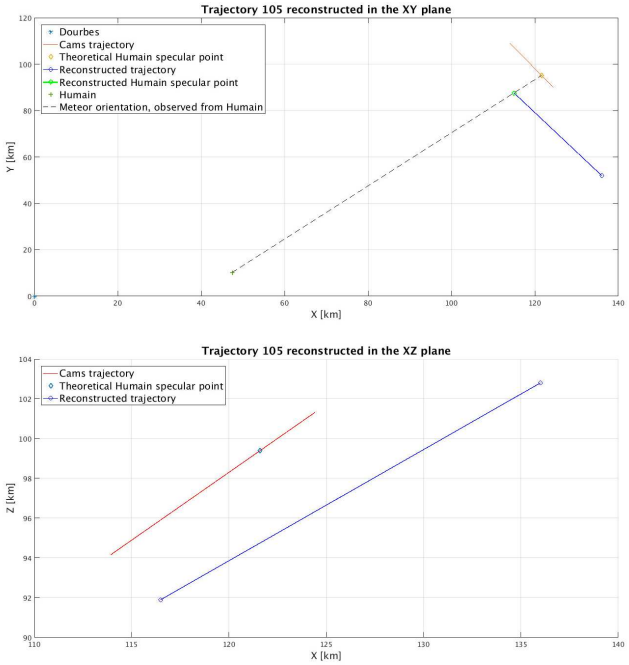

Figure 5 – Example of result obtained for CAMS trajectory 105 using Method 2.

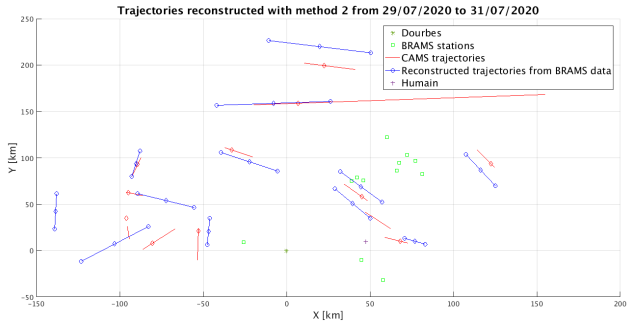

Figure 6 – Results obtained for the 12 selected CAMS trajectories using Method 2. The projections are shown in the horizontal XY plane. The position of the interferometer in Humain is indicated by the plus symbol.

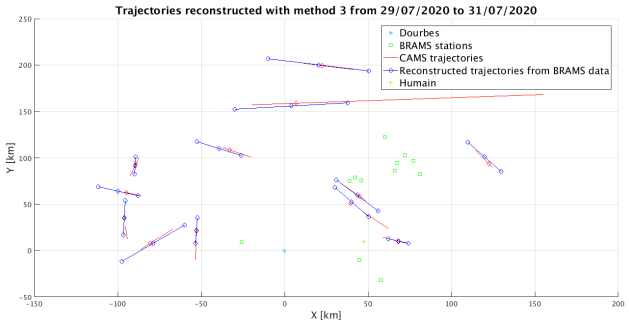

Figure 7 – Results obtained for the 12 selected CAMS trajectories using an hypothetical method where the range traveled by the radio waves would be available for each receiving station.

cal clusters of stations as we did in 2020 in the Limburg province (North-East of Belgium). Indeed, since Method 1 requires at least 6 stations but preferably more, we need stations located not too far away from each other (in order to detect the same meteors) but not too close either (otherwise the time delays become very small and of the order of the measurement uncertainty). A spatial separation of the order of 10–30 km is therefore adequate.

Finally, we have considered another possibility for the future: including some sort of phase-coding in the transmitted CW signal in order to be able to access the total range traveled by the radio wave (see e.g. Vierinen at al., 2016). It is out of the scope of this paper to discuss the feasibility and potential complications of implementing this technique in the BRAMS network but simulations have been conducted to see what would be the advantages for meteoroid trajectory reconstruction. In this case, one additional equation describing the total distance traveled by the radio wave would become available for each receiving station. Therefore, data from only 3 stations would be enough since we would have 6 equations for 6 unknowns with the 3 equations providing $dS_i/dt = 0$. This was tested for the 12 selected trajectories (using the same solver) and results are presented in Figure 7. The reconstructed trajectories are very close or sometimes overlap with the CAMS ones. The reconstructed speeds are also in very good agreement with the CAMS measurements.

In conclusion, implementing a method to obtain the total range (e.g. using a CW phase coding) would certainly be of great benefit in the future but the technical implementation and subsequent data analysis is not trivial. Nevertheless, a lot of effort and development are currently made on methods 1 and 2 since they can be applied to a lot of current and archived BRAMS data. The results will be presented in another publication. Further development, improvement and extension of the BRAMS network are also constantly envisaged.

7 Acknowledgement

The authors would like to warmly thank Mr. Mathias Van den Bossche who worked on this topic with great motivation during his Master Thesis at the University of Liège. The BRAMS network is funded partly by the Solar-Terrestrial Center of Excellence (STCE). The BRAMS project is an active Pro-Am collaboration. We would like to thank all operators hosting the receiving stations.

References

Anciaux M., Lamy H., Martinez Picar A., Ranvier S., Calders S., Calegaro A., and Verbeeck C. (2020). "The BRAMS receiving station v2.0". In Pajer U., Rendtel J., Gyssens M., and Verbeeck C., editors, *Proceedings of the International Meteor Conference, Bollmannsruh, Germany, 03-06 October 2019*. International Meteor Organization, pages 39–42. ISBN 978-2-87355-033-2.

Jenniskens P., Gural P., Grigsby B. J., Newman K. E., Borden M., Koop M., and Holman D. (2011). "CAMS : Cameras for allsky meteor surveillance to establish minor meteor showers". *Icarus*, **216**, 40–61. doi: 10.1016/j.icarus.2011.08.012.

Jones J., Webster R., and Hocking W. (1998). "An improved interferometer design for use with meteor radar". *Radio Science*, **33**, 55–65. doi: 10.1029/97RS03050.

Lamy H., Anciaux M., Ranvier S., Calders S., Gamby E., Martinez Picar A., and Verbeeck C. (2015). "Recent advances in the BRAMS network". In Rault J.-L. and Roggemans P., editors, *Proceedings of the International Meteor Conference, Mistelbach, Austria, 27-30 August 2015*. International Meteor Organization, pages 171–175. ISBN 978-2-87355-029-5.

Lamy H. and Tétard C. (2016). "Retrieving meteoroids trajectories using BRAMS data : preliminary simulations". In Roggemans A. and Roggemans P., editors, *Proceedings of the International Meteor Conference, Egmond, the Netherlands, 2-5 June 2016*. pages 143–147. ISBN 978-2-87355-030-1.

Lamy H., Tétard C., Anciaux M., Ranvier S., Martinez Picar A., Calders S., and Verbeeck C. (2018). "First observations with the BRAMS radio interferometer". In Gyssens M. and Rault J.-L., editors, *Proceedings of the International Meteor Conference, Petnica, Serbia, 21-24 September, 2017.*

International Meteor Organization, pages 132–137. ISBN 978-2-87355-031-6.

Mazur M., Pokorny P., Brown P., Weryk R., Vida D., Schult C., Stober G., and Agrawal A. (2020). "Precision measurements of radar transverse scattering speeds from meteor phase characteristics". *Radio science*, **55**, 1–32. doi: 10.1029/2019RS006987.

Roggemans P., Johannink C., and Breukers M. (2016). "Status of the CAMS-BeNeLux network". In Roggemans A. and Roggemans P., editors, *Proceedings of the International Meteor Conference, Egmond, the Netherlands, 2-5 June 2016*. IMO, pages 254–260.

Vierinen J., Chau J., Pfeffer N., Clahsen M., and Stober G. (2016). "Coded continuous wave meteor radar". *Atmospheric Measurement Techniques*, **9**, 829–839.

Handling Editor: Javor Kac
This paper has been typeset from a LaTeX file prepared by the authors.

Spectral Calibration of Meteors: An Elevation-Dependent Atmospheric Correction

Salvatore Vicinanza[1,2], *Detlef Koschny*[2], *Regina Rudawska*[2,3], *Daphne Stam*[1], *Wouter van der Wal*[1], *Joe Zender*[2]

By analysing the spectra of meteors ablating in the Earth's atmosphere, one can acquire valuable information about the composition of their parent bodies (asteroids and comets). A challenge to the accurate composition inference from meteor spectra comes from the correction for the atmospheric extinction; its dependence on the elevation of the meteor is particularly challenging, though often not considered in the calibration chains. The main novelty of this research is the development of an elevation-dependent approach for the atmospheric extinction correction of meteor spectra and the assessment of its significance for the accuracy of meteoroid composition inference.

The procedure developed for the spectral calibration corrects meteor spectra for the different extinction during a meteor's path in the atmosphere. The spectra are corrected for the direction of the incoming radiation and the scattering of gas molecules and aerosols, using an atmospheric correction vector. This vector depends on the meteor's elevation (both angle above horizon and elevation above ground) at the time of the frame observation and a different correction vector is estimated for each frame observed. This elevation-dependent procedure differs from the state-of-the-art practice of applying the same correction over all frames of the observed meteor spectrum.

An improvement results on the analyses of meteor spectra if the elevation-dependent atmospheric correction is applied. Using a case study, we show that the intensity of spectral features below 400 nm can differ by more than 20% when the elevation dependence of the extinction is considered as part of the spectral calibration pipeline. The use of this atmospheric correction has significance for the accuracy of meteoroid composition inference, especially for elements emitting at lower wavelengths. We show that the estimation of the Fe and Ca abundance in the case-study meteoroid increase by 10% after the application of this new spectral calibration procedure.

Received 2021 November 5

This work has been presented at the International Meteor Conference 2021 (held online).

1 Introduction

1.1 Background and Research Overview

Meteor spectroscopy is based on remote observations of ablating meteoroids in the atmosphere. For this reason, although meteor spectra observed by on-ground cameras primarily reflect the internal composition of meteoroids, they are also inherently affected by the type of meteoroid-atmosphere interaction taking place during each event. The Earth's atmosphere influences the amount of light transmitted from the meteor to the observing camera. Consequently, it modifies the intensities of meteor spectra features observed from ground. To accurately infer the composition of meteoroids in space, it is thus important to correct for the effects of optical atmospheric extinction.

Atmospheric extinction depends on the optical paths, and hence on the elevation of the meteoroid in its passage through the atmosphere. Specifically, the extinction varies with the elevation angular term (angle above horizon) and linear term (elevation above ground). Therefore, a precise calibration pipeline should provide a correction based on the meteor's elevation change along its path in the atmosphere. Instead, in meteor spectroscopy research, generally the same atmospheric correction is applied over all the frames observed for a meteor event, using a "standard curve" of the atmospheric extinction (Dubs & Maeda, 2016); calibrations with these standard curves do not account for the variation in atmospheric extinction along the meteor's path. To the best of our knowledge, no research in literature has yet investigated in detail the effects on the accuracy of the meteoroid inference, resulting from the application of an elevation-dependent approach for atmospheric calibration.

This research was conducted within the framework of ESA's Meteor Research Group (MRG) and builds upon the already-available MRG data reduction and calibration pipelines (Zender et al., 2014; Rudawska et al., 2020). The MRG operates the Canary Island Long-Baseline Observatory (CILBO). From CILBO, first-order spectra of meteors are collected on the spectral camera, i.e. ICC8 (Koschny et al., 2013). Previous research within the MRG, including Rudawska et al. (2020) and Löhle et al. (2021), analysed the 400–800 nm features for a set of meteor spectra collected by CILBO, in the order of 50 events. Features outside the 400–800 nm range were neglected, due to the limited instrument sensitivity at these wavelengths, which was originally obtained from on-site laboratory calibration. Moreover, the original MRG calibration pipeline did not include any type of atmospheric correction, not

[1]Faculty of Aerospace Engineering, Delft University of Technology, Delft, The Netherlands.
Salvatorevicinanza@gmail.com
[2]European Space Agency, ESA/ESTEC, Noordwijk, The Netherlands.
[3]RHEA Systems, Noordwijk, The Netherlands.

IMO bibcode WGN-496-vicinanza-calibration
NASA-ADS bibcode 2021JIMO...49..201V

even the "standard curve" correction mentioned in the previous paragraph.

In the present research, a larger set of data from CILBO was analysed, with more than 350 new events inspected. From this larger set, it was noted that the intensity of features outside the 400–800 nm range was significant for some events, especially for the features at the lowest wavelengths. Thus, we decided to enlarge the wavelength range of interest for spectral analysis outside the original 400–800 nm range; this led to the characterisation of an instrument response curve in the range 350 nm–840 nm. Moreover, it was observed that spectral features change depending on the elevation of the meteor. Hence, we investigated how the atmospheric extinction variation with meteor's elevation influence meteor spectra features.

To gain a better understanding about the effects which the variation of atmospheric extinction with the meteor's elevation has on meteor spectra, an elevation-dependent procedure for atmospheric calibration was developed and validated within this research. The main objective of this paper is to discuss this procedure and present results from a case study, showing how this calibration pipeline can improve the accuracy of the meteoroid composition inference obtained during meteor spectral analysis. This is addressed in the following sections of the paper.

Section 1.2 introduces the experimental setup used in this research, i.e. CILBO. Section 2 explores the newly developed spectral calibration pipeline. In particular, section 2.1 describes the methodology and validation of the procedure for elevation-dependent atmospheric calibration, while section 2.2 presents the characterisation of the instrument spectral sensitivity curve in the range 350–840 nm. Section 3 presents the results from the case study considered: the meteor event observed on 2012 June 01 at $22^h51^m00^s$, local time (Canary Islands, Spain)[a]. Finally, section 4 gives the conclusions for the paper.

1.2 Our experimental setup: CILBO

CILBO is located in the Canary Islands, Spain. It has a double-station setup of intensified CCD video cameras (ICC). The video cameras are Toshiba Teli CS8310Bi, delivering phase-alternating line (PAL) video streams (Koschny et al., 2013). Three image-intensified cameras are mounted in two different locations: ICC8 and ICC7 mounted in Tenerife (CILBO-T station) and ICC9 in La Palma (CILBO-L station); all CILBO cameras monitor the same portion of sky, as sketched in Figure 1. Data from ICC8 and ICC7 represent the primary source for this study. ICC7 records the zeroth order of meteors. ICC8 is equipped with a Zeiss transmission grating in front of its lens (see Figure 2). The grating is mounted at an angle to optimize the acquisition of the first-order spectra. Both ICC8 and ICC7 have a frame rate of 25 frames per second (time resolution of 0.04^s), an image resolution of 768×576 px and 8 bit dynamic accuracy.

ICC7 and ICC8 run on the same local computer, with ICC7 continuously recording images of the night sky and ICC8 waiting in standby. When the MetRec software (Molau & Gural, 2005) detects a meteor in ICC7's field of view, it triggers the acquisition of the frames from ICC8. Then, both ICC8 and ICC7 frames with detected meteors are saved as BMP files.

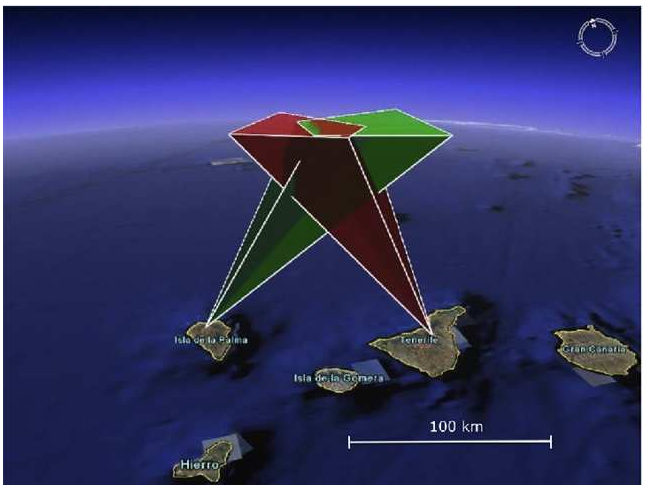

Figure 1 – Sketch of CILBO's double station camera set-up (Koschny et al., 2013).

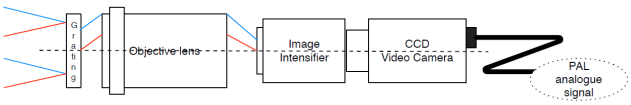

Figure 2 – CILBO's ICC8 block diagram (Zender et al., 2014).

2 Spectral Calibration of Meteors

2.1 Atmospheric Calibration

The atmospheric calibration corrects meteor spectra for the wavelength-specific extinction of the whole atmosphere between the meteor and ICC8. Atmospheric extinction varies with the meteor elevation's angular term, i.e. angle above the horizon, and the elevation's linear term, i.e. meteor's elevation above ground. However, the elevation-dependent nature of the atmospheric correction is not discussed in the calibration chains described in literature (Dubs & Maeda, 2016; Jenniskens, 2007; Borovička et al., 2005).

Atmospheric extinction also slightly depends on the meteor azimuth. However, since CILBO cameras monitor a fixed sky volume of less than 100 km width, the azimuth variability in atmospheric conditions is to first order negligible for observations taken at the same elevation, i.e. in the same atmospheric layer. Consequently, the azimuth dependence of atmospheric extinction can be neglected once the effects of meteor elevation are considered. Finally, astrometric calibration corrects for the difference in light dispersion that camera distortions induce on meteors observed at different azimuth locations in the field of view.

The atmospheric calibration pipeline developed in this research associates a different correction to each

[a]All times are expressed in the time zone of the Canary Islands, Spain (UTC±00:00), where the meteor observations of this research were made.

elevation in the meteor's path, calculating as many correction vectors as there are frames. In doing so, this atmospheric calibration returns the spectral information of the meteoroid at the point in sky where the ICC8 observation occurs. Section 2.1.1 describes the methodology of this atmospheric calibration pipeline. Then, section 2.1.2 presents the validation of the pipeline, performed via a software for atmospheric transmission calculation called TAPAS.

2.1.1 Methodology: Elevation-dependent approach

To correct each meteor spectrum observed by ICC8 for the atmospheric extinction which affects the light transmission from the meteor to ground, the pipeline associates a correction vector to each observed spectrum. The vector provides, for each spectral feature of the observed meteor spectrum, a scaling factor to return the feature's appearance in the absence of atmospheric extinction. Atmospheric correction vectors are calculated following the extinction law in Appenzeller (2012):

$$\textbf{Correction vector} = \frac{\mathbf{F_{0,met}}}{\mathbf{F_{met}}} = \frac{1}{\exp\left(\frac{-\mathbf{b_{met}}}{\cos(\theta_{met})}\right)} \quad (1)$$

Here, $\mathbf{F_{met}}$ represents the intensity of each feature of the observed meteor spectrum, $\mathbf{F_{0,met}}$ the intensities of the true (atmospheric-corrected) spectrum, θ_{met} the Zenith angle of the observed meteor relative to ICC8, and $\mathbf{b_{met}}$ the atmospheric optical thickness; $\mathbf{b_{met}}$ is a vector specifying the attenuation of light through the atmosphere in function of the wavelength. In this study, only the aerosols' extinction and gas molecules scattering were considered for the estimation of the optical thickness. These have the greatest contribution on the atmospheric extinction affecting visible meteor spectra and to first order allow for a good-quality atmospheric correction.

For the gas molecules' scattering-only extinction, the optical thickness ($\mathbf{b_{gas}}$) is obtained as shown below:

$$\mathbf{b_{gas}} = N_{gas} \cdot \boldsymbol{\sigma_{sca}} \quad (2)$$

with N_{gas} the column number density of gas molecules (number of particles per m^2) and $\boldsymbol{\sigma_{sca}}$ the scattering cross section of gas molecules (in m^2). N_{gas} and $\boldsymbol{\sigma_{sca}}$ are obtained using Equation 3 and 4 below, considering a condition of hydrostatic equilibrium.

$$N_{gas} = \frac{p_{bottom} - p_{top}}{m_{gas} \cdot g} \quad (3)$$

$$\sigma_{sca}(\lambda) = \frac{24\pi^3}{N_L^2}\frac{(n^2-1)^2}{(n^2+2)^2}\frac{(6+3\delta)}{(6-7\delta)}\frac{1}{\lambda^4} \approx \frac{C}{\lambda^4} \quad (4)$$

m_{gas} and g are the mass of a gas molecule (obtained for dry air conditions, molar mass of 28.96 g/mol) and the gravitational acceleration (9.806 m/s^2); p_{bottom} and p_{top} are the atmospheric pressures at the observer and target location, respectively ICC8 and the meteor. In Equation 4, n is the gas refractive index (assumed constant), λ the wavelength, N_L the Loschmidt's number ($2.54743 \cdot 10^{25}\,m^{-3}$) and δ the gas depolarization constant (0.03 for terrestrial air, ignoring the λ-dependence).

In Equation 3, g and m_{gas} are approximated as constants between the troposphere (where the ICC8 is located) and thermosphere (where the meteor observation occurs), while p_{top} and p_{bottom} are obtained considering a U.S. 1975 Standard atmosphere. These are calculated as defined below:

$$p = p_0 \cdot \left(1 - \frac{L \cdot h}{T_0}\right)^{\left(\frac{g \cdot M}{L \cdot R_0}\right)} \quad (5)$$

where p_0 is the sea level (s.l.) standard pressure (101 325 Pa), L the temperature lapse rate (9.76 K/km, dry air), T_0 the s.l. standard temperature (288.16 K), M the molar mass (0.029 kg/mol, dry air), R_0 the universal gas constant (8.314 J/(mol·K)), and h the height above sea level. The pressure at the height of ICC8 (p_{bottom}) is fixed for each meteor event, as the camera stays fixed in time ($h = 2367\,m$). By contrast, the pressure at the meteor's location (p_{top}) varies along the meteor's path. Thus, a different estimation is made for each frame.

Concerning the contribution of aerosols, the aerosol optical thickness is taken from NASA's AERONET database[b]. The data was recorded by an AERONET sun-photometer in Izaña, Tenerife, located at around 1.17 km ground distance from our ICC8 camera. The data is provided at discrete, irregular intervals from 340 nm to 870 nm.

The overall optical thickness at the meteor's location ($\mathbf{b_{met}}$) is obtained combining the Rayleigh optical thickness of gas molecules ($\mathbf{b_{gas}}$) with the aerosol optical thickness (**AOT**) values obtained from the AERONET database, following the relation below:

$$\mathbf{b_{met}} = \mathbf{b_{gas}} + \mathbf{AOT} \quad (6)$$

Before performing the step above, the aerosol optical thickness was interpolated to the wavelengths of the Rayleigh optical thickness, spaced at half the spectral resolution of ICC8 camera (≈1 nm/px).

Figure 3 shows the parameters considered as part of the newly implemented atmospheric calibration. Two atmospheric layers are considered in our procedure. The first layer is fixed at ICC8' height from ground (2395 m). This has pressure equal to p_1 and optical thickness $\mathbf{b_1}$; p_0 is the pressure at sea level. The location of the second layer, instead, varies depending on the meteor's location at the time of the meteor frame acquisition. It has pressure p_2 and optical thickness $\mathbf{b_2}$. In our case, $\mathbf{b_2}$ is the value of $\mathbf{b_{met}}$ used in Equation 1 and varies depending on the elevation of the meteor along its path.

Overall, three major assumptions were used for the development of this atmospheric calibration routine.

[b]NASA's AERONET database is found at `https://aeronet.gsfc.nasa.gov/new\_web/aerosols.html`. The file which contained the data used was named "Aerosol Optical Depth (AOD) with Precipitable Water and Angstrom Parameter".

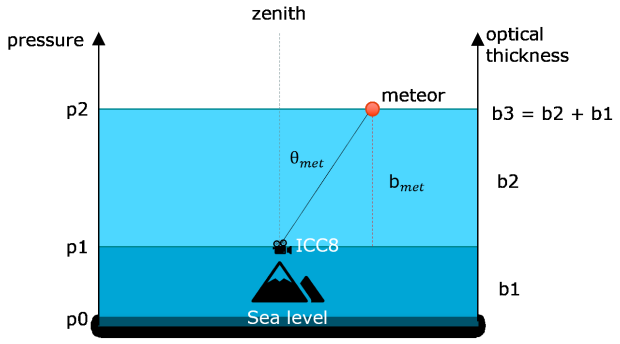

Figure 3 – Sketch showing the role of optical thickness ($\mathbf{b_{met}}$), Zenith angle of observed meteor (θ_{met}) and atmospheric pressure (p), which are used in the formulation of the atmospheric calibration of ICC8 observations of meteors (Equation 1 and 3).

First, a double-layer standard atmosphere (U.S. 1975 Standard Atmosphere) was considered. Second, a condition of dry air was assumed for calculating gas molecules' mass and air pressures. Third, it was assumed that the atmospheric extinction was only affected by aerosols and gas molecules' scattering; absorption and reflection from water vapour, ozone or other agents were not considered. To first order, these assumptions do not significantly bias the results' accuracy, since the neglected effects would only influence the extinction intensity to the hundredths or lower orders; in particular, the extinction by water vapour, ozone and oxygen is significantly lower than the combination of gas molecules and aerosol extinction across the visible spectrum (Patat et al., 2011). Meanwhile, these assumptions allow to reduce the complexity of the atmospheric extinction mathematical modelling, since the neglected effects would require additional terms and higher order polynomials (than Equation 4) for their accurate estimation.

The newly implemented atmospheric calibration improved the MRG calibration pipeline, which originally lacked any type of correction for the atmospheric extinction. The case study results discussed in section 3.1 show the significance of the improvement. The elevation-dependent approach represents the key feature of this new pipeline. Depending on the meteor's elevation (both angle above horizon and elevation from ground) at the time when the spectrum is observed, the correction vector changes. Consequently, the atmospheric calibration outputs one correction vector per ICC8 frame recorded. By correcting for the different extinctions taking place while the meteor travels through different elevations in the atmosphere, the line intensity estimations can be improved by more than 20% for low-wavelength features, as discussed in section 3.2.

2.1.2 Validation: TAPAS

The routine developed for the atmospheric correction was validated using TAPAS[c]. TAPAS is a web-based software which allows users to compute the atmospheric transmission in the line-of-sight to a target with known sky coordinates (Bertaux et al., 2014). Having provided the celestial coordinates of the target body and the observation date, TAPAS computes the atmospheric transmittance from the body in space to the observatory specified. This can be compared to the inverse of the term "Correction vector" in Equation 1, for the same event and observational setup.

Vega was selected as the validating target. This A0Va star has an apparent magnitude of +0.026 and its spectrum is visible in several ICC8 frames. Four test events, showing good visibility of Vega spectrum in ICC8, were considered for the validation; these were also used for the sensitivity curve calculation (explained in section 2.2).

Results from two of the events chosen for the validation are shown in Figure 4. Their behaviour exemplifies the behaviour of all other test events used for the validation. From Figure 4, it is possible to see that the atmospheric transmittance computed by TAPAS (*orange*) agrees to great extent with the results of the atmospheric calibration process developed (*blue*). The dips in the TAPAS results are mostly caused by the absorption from particles in the atmosphere, not considered in our atmospheric calibration pipeline. The smoother dip at around 600 nm is linked to the contribution of ozone absorption; the profound dips around 750–780 nm are linked to oxygen absorption; other dips are linked to water vapour, which has significant day-to-day variation. Differently than gas molecules' scattering, the contributions of ozone, oxygen and water vapour absorption have large time variability; they are difficult to approximate through mathematical modelling and were not included in this study, as already discussed in Section 2.1.1.

The computation of the atmospheric transmission by TAPAS takes significantly more time compared to the atmospheric calibration routine developed in this research. TAPAS requests users to provide the input information necessary for the atmospheric transmission calculation (date, observer location, target celestial coordinates) via a form; then, TAPAS performs the requested simulation. At the end of each simulation, TAPAS sends the results via email. The entire process takes $\approx 10^{m}$. By contrast, results for the same events are obtained with our atmospheric calibration in $\approx 10^{s}$. Also, TAPAS does not account for the dependence of atmospheric extinction with height. In fact, TAPAS only considers the right ascension and declination of the target body. Thus, TAPAS is good for star observations, where the body is outside of the atmosphere, but less accurate when a body moves within the atmosphere.

2.2 Spectral Sensitivity Characterisation

The last process of the spectral calibration pipeline developed is the spectral sensitivity calibration. This process adjusts the intensity of the individual spectral lines based on the ICC8 spectral sensitivity curve, which displays the instrument's efficiency to record signals at specific wavelengths. In the original MRG calibration pipeline, the ICC8 spectral sensitivity curve was calibrated in the laboratory, using on-ground observations

[c]TAPAS web-based service is accessible through this link: `http://cds-espri.ipsl.fr/tapas/data?methodName=viewForm`

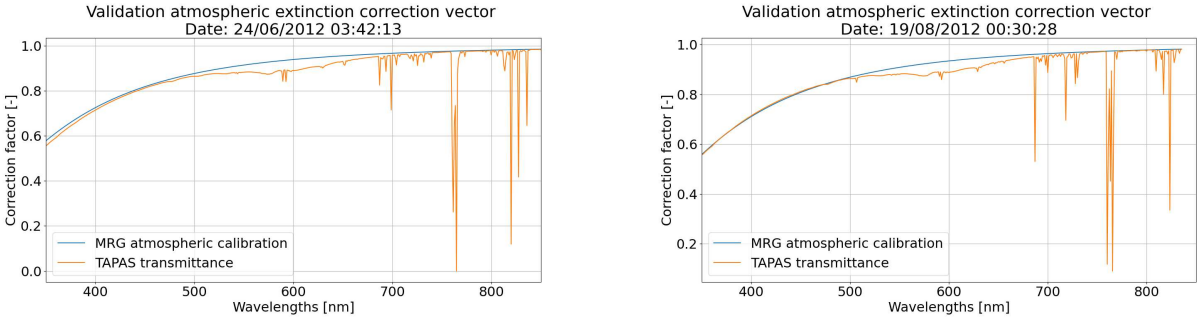

Figure 4 – Atmospheric transmission in function of wavelength, for two of the events used for the atmospheric calibration validation. Comparison between TAPAS results (*orange*) and results obtained using atmospheric calibration process developed (*blue*).

of lamps with known emission spectra. The estimated curve was limited to wavelengths in the range 400–800 nm as it was assumed that ICC8 could not record signals outside this range. However, an inspection of the new spectra analysed within this research revealed that a large set of the meteor events observed by ICC8 contained features of interest outside the 400–800 nm range. For this reason, within this study we performed a new characterisation of ICC8 sensitivity over a larger wavelength range: 350–840 nm[d].

As the experimental equipment in Tenerife has not been physically reachable for the duration of this research, the new spectral response could not be obtained in a laboratory. The characterisation of ICC8 spectral sensitivity curve resulted from the processing of the ICC8 observations of star Vega (α-Lyrae), using the methodology described in section 2.2.1. The validation of the spectral sensitivity curve was performed using spectra of well-known bright stars observed by ICC8: Deneb, Elnath and Castor. This is described in section 2.2.2.

2.2.1 Methodology: Vega observations from CILBO

The process of spectral sensitivity calibration corrects spectra observed by ICC8 for the instrument sensitivity curve, according to the following relation:

$$\text{Calibrated spectrum} = \frac{\text{Spectrum observed by ICC8}}{\textit{ICC8 sensitivity curve}} \tag{7}$$

The *ICC8 sensitivity curve* obtained from this research results from the comparison between the true spectrum of Vega ("reference" in Figure 6), obtained by the Space Telescope Imaging Spectrograph (STIS) on board of the Hubble Space Telescope, and ICC8 observations of Vega ("observed" in Figure 6): the difference in intensity between features at the same wavelength in the reference and observed spectrum gives the ICC8 sensitivity at

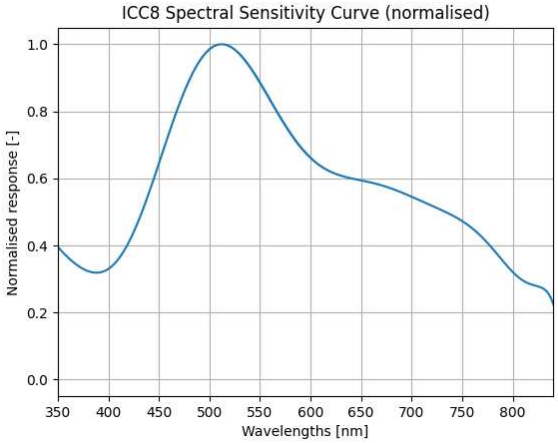

Figure 5 – ICC8 spectral sensitivity curve, normalised and limited to a wavelength range from 350 nm to 840 nm. This calibration curve was obtained by measuring spectra of Vega star.

that wavelength. The reference spectrum of Vega is taken from the CALSPEC catalogue[e].

According to Buil (2019), the spectrum of a target observed by the same instrument varies across the different dates of observation, even though the target's true spectrum stays approximately constant. In this study, this was noted for Vega's spectrum, which showed differences in the spectral intensity among the different observations of the star. These changes depend on several factors, among which the variability in the background luminosity and atmospheric conditions. For this reason, the observed spectrum to compare with the reference spectrum was the result of a median over four good-quality observations of Vega, i.e. four observations in which the first-order spectrum of Vega star was within the ICC8's field of view and had high signal to noise ratio. By taking the median of different spectral observations, the changes in intensity are balanced and hence the result is a more representative spectrum. The median was preferred over an arithmetic mean as the former is less affected by outliers, which is what we want to correct for. The dates of the observations used are: i. 2012 June 24, $03^h42^m13^s$ (elevation angle 61 °1); ii. 2012 August 19, $00^h30^m28^s$ (elevation angle 55 °6); iii.

[d]The wavelength boundaries used for the characterisation of the new ICC8 spectral sensitivity curve were chosen based on the absence of significant features outside the 350–840 nm range and the lower accuracy of the atmospheric correction – the analytical formula used for atmospheric extinction modelling introduces higher errors when trying to estimate the extinction below 350 nm, due to the higher complexity of the phenomena in the UV.

[e]CALSPEC Archive: `https://archive.stsci.edu/hlsps/reference-atlases/cdbs/calspec/`.

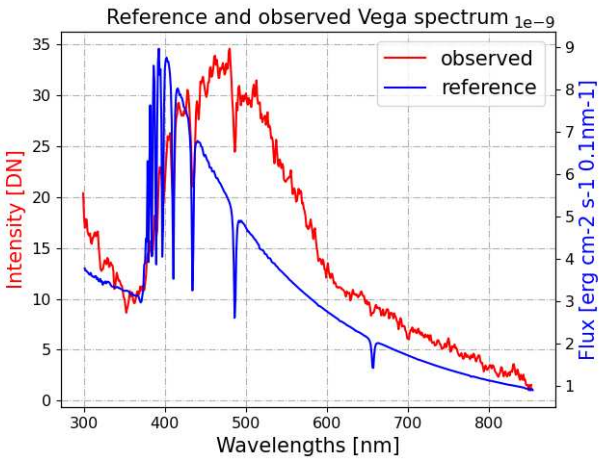

Figure 6 – Reference Vega spectrum, obtained by the STIS instrument on board of the Hubble Space Telescope (*blue*), and Vega spectrum observed from ICC8 (*red*). The relation between the two spectra is used for the ICC8 sensitivity curve estimation.

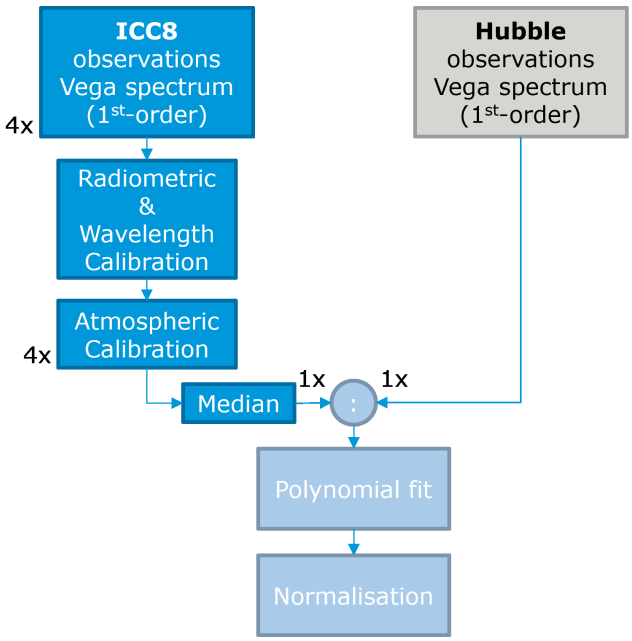

Figure 7 – Schematic of the steps followed in estimation of ICC8 spectral sensitivity curve.

2012 September 19, $22^h16^m46^s$ (elevation angle 57.°1); iv. 2013 July 05, $03^h35^m39^s$ (elevation angle 54.°2).

The procedure used for ICC8 spectral sensitivity curve estimation is schematised in Figure 7. This is divided in three parts: (I) processing of ICC8 observed spectra, (II) comparison of the reference and observed spectrum, and (III) final adjustment of the sensitivity curve.

(I) The first part of the processing of ICC8 observed spectra involves the flat-field and dark current correction of each frame, and the wavelength calibration of the four ICC8 observations of Vega spectrum, following the pipeline discussed in Zender et al. (2014). Next, the spectra are corrected for atmospheric extinction, using the methodology explained in section 2.2.1. The final observed spectrum is the median of the four calibrated spectra.

(II) In the second part of the estimation scheme, the final observed spectrum is divided by the reference spectrum obtained by STIS. The comparison between the two spectra is visualised in Figure 6.

(III) In the third step of the processing of ICC8 observed spectra, the outcome of this ratio is adjusted to a smoothed and normalised, unit-less curve. To smoothen the response curve, averaging out the noise and absorption peaks in both spectra, the curve resulting from step (II) was fitted with a least-squares polynomial of order twelve. The final instrument response curve is the fitted spectrum after normalisation, which was executed using the min-max technique (Patro & Sahu, 2015).

The ICC8 sensitivity curve resulting from this procedure is shown in Figure 5.

2.2.2 Validation: Use of bright stars

To validate the ICC8 sensitivity curve (visualised in Figure 5), the spectra of bright stars observed by ICC8 were compared to their corresponding reference spectra. The observed spectra were first sensitivity calibrated, following Equation 7, before being compared to their reference. The bright stars used for the validation are Deneb, Elnath and Castor, whose reference spectra were obtained from the HyperLeda catalogue[f].

The results of this validation are shown in Figure 8 and 9. For all the cases considered, the calibrated spectra of the bright stars observed from ICC8 resemble the behaviour of the corresponding reference spectra (observed outside of the atmosphere), reported in the HyperLeda catalogue. Since in this research we were only interested in the relative analysis of the spectral features, the spectra observed from ICC8 were not converted to physical flow units ($\mathrm{erg\,cm^{-2}\,s^{-1}\,0.1\,nm^{-1}}$, unit of reference spectra provided by the catalogue) but were left in digital units (ICC8 pixel values). As a consequence, the observed and reference spectra show different units and hence the comparison between the two can only be done by comparing their shapes. The scales of the reference and observed spectrum are chosen to range from the point of lowest signal to the highest, with the boundaries in the plots taken at 10% distance from the highest point.

All the spectra used for the validation were observed at different dates and times. The agreement between reference and calibrated observed spectra for all these different events verified that the sensitivity calibration is not dependent on the specific conditions of the observation date (e.g. background or atmospheric conditions).

Altogether, these results confirm the validity of the estimated ICC8 sensitivity curve for the sensitivity calibration of celestial bodies observed from ICC8.

3 Results

To show the improvements on the accuracy of meteoroid composition inference which derive from the application of the newly developed spectral calibration pipeline, this section analyses the results from a case

[f]HyperLeda catalogue: `http://leda.univ-lyon1.fr/`.

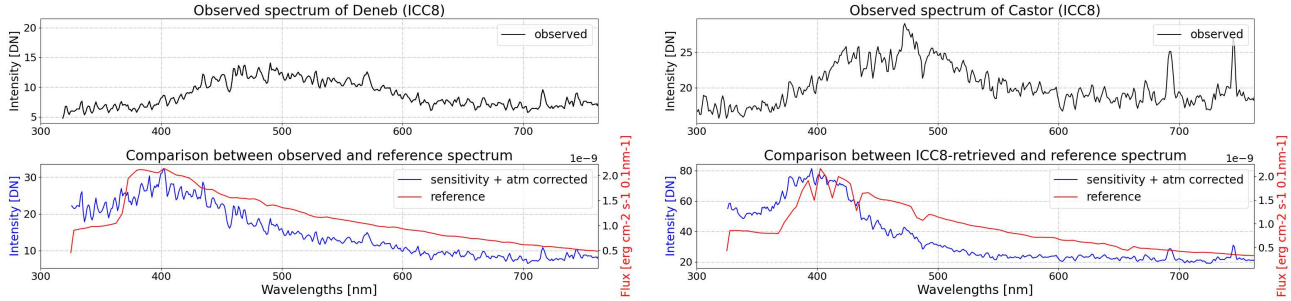

Figure 8 – Spectra of bright stars Deneb (*left*) and Castor (*right*), observed from ICC8 on 2013 March 10, $00^h39^m51^s$ and 2013 March 28, $22^h49^m38^s$. *Black*: Observed spectrum before sensitivity calibration. *Blue*: Spectrum after the complete spectral calibration (instrument sensitivity and atmospheric extinction). In *red*, the reference spectrum of the bright stars (Hyper Leda catalogue).

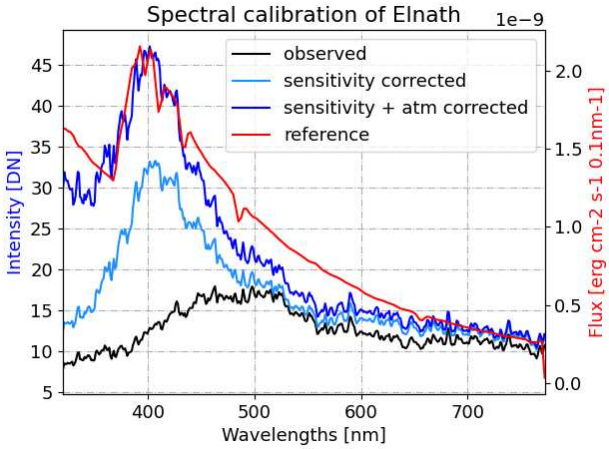

Figure 9 – Evolution of the spectrum of Elnath star during the application of the spectral calibration. *Black*: Spectrum of Elnath as observed from ICC8 on 2012 February 23, $23^h15^m33^s$. *Light blue*: Elnath spectrum observed by ICC8, after sensitivity calibration, with no correction for atmospheric extinction. *Blue*: Elnath spectrum observed by ICC8, after spectral calibration (sensitivity and atmospheric correction). *Red*: Reference spectrum of Elnath obtained by STIS outside of atmosphere.

Figure 10 – Event 2012 June 01, $22^h51^m00^s$. Zeroth-order (*left*) and first-order spectrum (*right*) seen from ICC8.

study. The meteor event considered for case study is the one recorded on 2012 June 01 at $22^h51^m00^s$, whose first-order spectrum recorded by ICC8 is shown in Figure 10. The meteor generated from the Antihelion source, has a brightness of −1.5 and a speed of 30 km/s. The meteor evolution was recorded over 37 frames, for each of which a tailored spectral calibration was performed. The observations record a path of more than 21 km in the atmosphere.

The original MRG calibration pipeline did not include any type of correction for the effects of atmospheric extinction on meteor spectra (Rudawska et al., 2020). The study presented in section 3.1 aims to show the importance of applying an atmospheric calibration, especially for the accurate estimation of elements' emissions at low wavelengths. In that section, the elements' abundances obtained using the atmospheric calibration pipeline developed in this research are compared to the abundances obtained in case of no atmospheric correction. Then, section 3.2 focuses on the importance of considering the elevation dependence of the atmospheric extinction. Using the case study, we show how the application of an elevation-dependent correction can significantly change the line intensity estimation of meteor spectra, compared to the more common practice of applying the same correction over all frames. The effects of the elevation dependence of atmospheric correction are isolated.

3.1 Effects of the atmospheric calibration on spectral analysis and meteoroid composition inference

To show the improvements which the atmospheric calibration pipeline developed can have on spectral analysis, first we decided to present the case of Elnath, a bright star with a known spectrum. Figure 9 compares the reference spectrum of Elnath recorded by the Space Telescope Imaging Spectrograph (STIS) on board the Hubble Space Telescope (*red*), with the spectrum of Elnath star observed by ICC8, before and after atmospheric calibration. One can appreciate how the application of the atmospheric calibration increases the intensity of spectral features, especially towards the lower wavelengths, thus resulting in better agreement between the reference and observed Elnath spectra. The reason behind the difference in unit between the reference and

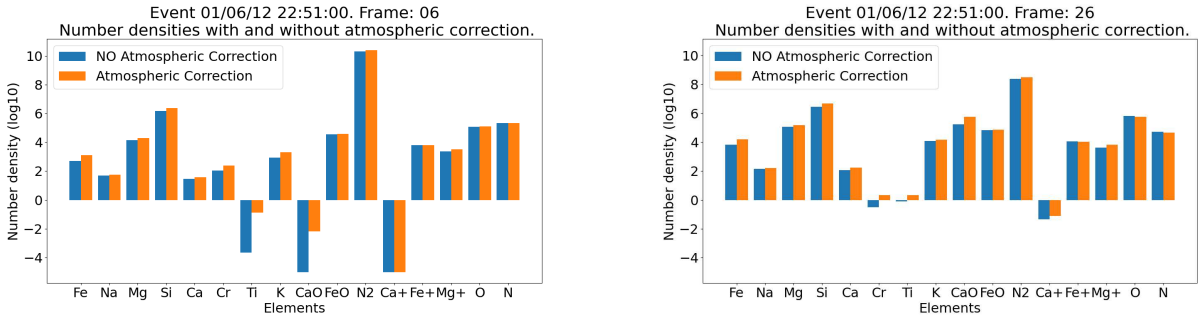

Figure 11 – Elements' number density for frame 06 (*left*) and 26 (*right*) for the meteor event recorded on 2012 June 01 at $22^{h}51^{m}00^{s}$. *Blue*: No atmospheric correction applied on the spectrum. *Orange*: Atmospheric correction applied.

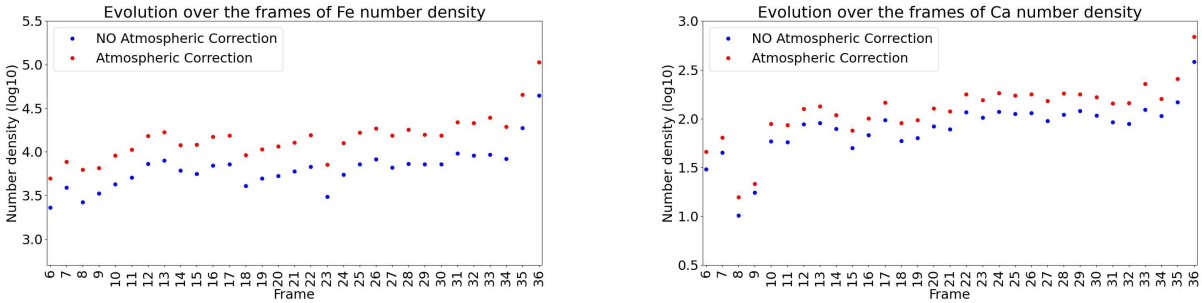

Figure 12 – Evolution of Fe (*left*) and Ca (*right*) number density along the meteor's path, for the meteor event recorded on 2012 June 01 at $22^{h}51^{m}00^{s}$. *Blue*: No atmospheric correction applied on the spectrum. *Orange*: Atmospheric correction applied. For this event, the meteor was firstly detected in frame 06 and lastly in frame 36.

observed spectra, and the choice of their scale are the same as already discussed in section 2.2.2.

Considering the 2012 June 01, $22^{h}51^{m}00^{s}$ case study, it is concluded that the application of the atmospheric calibration produces significant changes in the estimation of the elements' number densities. Figure 11 visualises the effects of applying the atmospheric calibration on the elements' number density estimations for two frames of the case study: frame 06 and 26. The two frames are separated by 1^{s} in time and more than 15 km in height. For both, the estimations after the application of the new procedure developed in this project are shown in *orange*; in *blue* are the estimations obtained using the original MRG pipeline. Looking at elements emitting at low wavelengths, like Fe and Ca which have the multiplet 2 emitted at 375 nm and 422 nm respectively, the application of the atmospheric calibration determined a significant increase: on average, Fe and Ca number densities were subject to an average increase greater than 10% over each frame, compared to the estimations done without atmospheric correction. This increase is consistent along the entire meteor's path, as observed from Figure 12.

The significance of this increase suggests that the application of the atmospheric calibration can affect the accuracy of the estimations of elements' abundance obtained from past research where the atmospheric extinction was not corrected for, like Rudawska et al. (2020). This change is not expected to substantially alter the validity of this study, focused on measuring the relative elements' abundance in meteoroids: meteor spectra were classified based on the intensities of magnesium, sodium and iron relative to the Mg I line intensity (at 518.2 nm). In fact, as shown by Figure 11, the changes induced on the intensity of spectral features are coherent for different elements. However, while these changes would not substantially alter conclusions on *relative* composition classification, they significantly affect the accuracy of *absolute* elements' abundance estimations.

3.2 Importance of the elevation-dependent approach

We investigated the significance of using an elevation-dependent spectral calibration on the accuracy of meteor spectral analyses and respective meteoroid composition inference. The case study here demonstrates the importance of using such an elevation-dependent approach for the accuracy of the results. Figure 13 shows the meteor spectrum of frame 34 recorded by ICC8 for date 2012 June 01 at $22^{h}51^{m}00^{s}$. The plot compares the line intensities of the meteor spectrum with and without the application of the elevation-dependent calibration approach. In particular, the *orange* line shows the spectrum after the correction for the specific elevation at which the meteor was observed in frame 34. The *blue* line shows the spectrum if the same correction was applied over all the frames and hence the atmospheric extinction variation with elevation was not considered.

The results show that the elevation-dependent correction changes the line intensity estimation by an average of 20% for spectral features below 400 nm. Considering for example the Fe I (2) emission at around

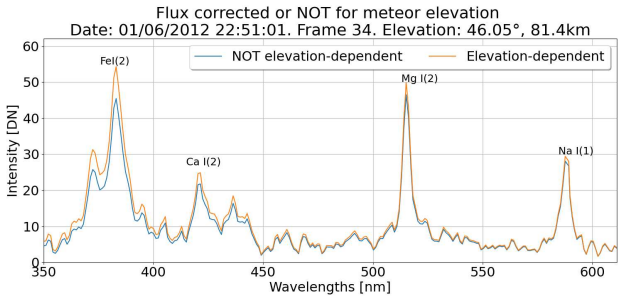

Figure 13 – Meteor spectrum with and without the application of the elevation-dependent approach for the atmospheric calibration. *Orange*: Spectrum corrected for the elevation dependence of the atmospheric extinction. *Blue*: No elevation-dependent correction applied. Meteor event recorded by ICC8 on 2012 June 01 at $22^{h}51^{m}00^{s}$.

375.5 nm, the features experience an increase in line intensity of about 30%. As the line intensities in meteor spectra are used to estimate the elements' abundance in the meteoroid, these changes improve the accuracy of the compositional inference, compared to cases in which the elevation dependence of the atmospheric correction is not considered. The significance of the changes, reaching also peaks of 30%, shows the importance of using an elevation-dependent approach, which considers the variation in atmospheric extinction as the meteoroid moves through the atmosphere.

4 Conclusions

This research focused on the spectral calibration of meteors and investigated the influence of the atmospheric extinction on the appearance and study of meteor spectra. An automatic procedure for the elevation-dependent atmospheric calibration was developed and validated. With elevation dependence is meant the dependence of the atmospheric correction on both the elevation angular term, i.e. angle above horizon, and its linear term, i.e. elevation from ground. The output of the atmospheric calibration pipeline developed are correction vectors, which correct the observed spectra for the atmospheric extinction. A correction vector is generated for each video frame recorded by ICC8; by doing so, this atmospheric correction follows the meteoroid's path in the atmosphere and allows to correct the meteor spectra for the variation in atmospheric extinction as the meteoroids travel within the atmosphere. The elevation dependence of the atmospheric extinction was previously not investigated in studies of meteor spectra. Thus, its consideration represents a novelty to the body of knowledge.

This research showed that the influence of the elevation dependence of the atmospheric extinction on the accuracy of meteoroid composition inference is significant. From the analysis of a case study meteor event observed on 2012 June 01, $22^{h}51^{m}00^{s}$, we showed that the use of an elevation-dependent approach for atmospheric correction can improve the line intensity estimation by more than 20% for features below 400 nm. This suggests that applying an elevation-dependent atmospheric calibration is preferable, in terms of accuracy of meteoroid composition inference, over the widely used standard atmospheric correction, which does not account for the extinction variation at the different times of meteor observation.

Furthermore, we showed how the application of the atmospheric calibration improves the pipelines of meteor spectral calibration and analysis, as for the case of the MRG pipeline which originally did not include corrections for atmospheric extinction. Considering the case study meteor event, elements with emissions at low wavelengths, like Fe and Ca, were subject to an average increase in number density greater than 10% over each frame, compared to the estimations done without atmospheric correction. The results from this research imply that the low-wavelength features calibrated with the original MRG pipeline were underestimated during past spectral analysis; low-wavelength features in visible spectra were the most affected, since atmospheric extinction corrections are most significant at near-UV wavelengths. Nevertheless, these changes are not expected to disprove the validity of earlier research on meteor spectroscopic observations like Rudawska et al. (2020).

Lastly, during this study the ICC8 spectral sensitivity curve was calculated over the wider wavelength range of 350–840 nm, compared to the original sensitivity curve obtained by previous MRG research, limited to 400–800 nm. This new curve was based on the comparison between first-order observations of Vega from CILBO and the reference Vega spectrum obtained from space (STIS observation, on board the Hubble Space Telescope).

The re-definition of ICC8 spectral sensitivity curve brings an improvement to the spectral calibration pipeline and is advantageous in view of future work in the Meteor Research Group: the wider sensitivity curve will allow to analyse features in the meteor spectra which were previously cut off; particularly, Si, Cr, Fe and Mg have significant features in the 350–400 nm range, and O and N for wavelengths above 800 nm. Including these additional features will result in more complete and hence higher accuracy inference of meteoroids' compositions from the analysis of CILBO spectral observations.

References

Appenzeller I. (2012). *Introduction to Astronomical Spectroscopy*. Cambridge Observing Handbooks for Research Astronomers. Cambridge University Press.

Bertaux J. L., Lallement R., Ferron S., Boonne C., and Bodichon R. (2014). "TAPAS, a web-based service of atmospheric transmission computation for astronomy". *Astronomy & Astrophysics*, **564**, A46.

Borovička J., Koten P., Spurný P., Boček J., and Štork R. (2005). "A survey of meteor spectra and orbits: evidence for three populations of Na-free meteoroids". *Icarus*, **174:1**, 15 – 30.

Buil C. (2019). "How to calculate the spectral response of a spectrograph [online]". `http://www.astroimage.info/spectra/NewInstrumentResponseProcessing18May19.pdf`. Last visited: 02 May 2021.

Dubs M. and Maeda K. (2016). "Calibration of meteor spectra". In Roggemans A. and Roggemans P., editors, *International Meteor Conference Egmond, the Netherlands, 2-5 June 2016*. page 65.

Jenniskens P. (2007). "Quantitative meteor spectroscopy: Elemental abundances". *Advances in Space Research*, **39:4**, 491 – 512.

Koschny D., Bettonvil F., Licandro J., Luijt C. v. d., Mc Auliffe J., Smit H., Svedhem H., de Wit F., Witasse O., and Zender J. (2013). "A double-station meteor camera set-up in the Canary Islands – CILBO". *Geoscientific Instrumentation, Methods and Data Systems*, **2:2**, 339–348.

Löhle S., Eberhart M., Zander F., Meindl A., Rudawska R., Koschny D., and Zender J. (2021). "Extension of the Plasma Radiation Database PARADE for the Analysis of Meteor Spectra". *Meteoritics & Planetary Science*, **56:2**, 352–361.

Molau S. and Gural P. S. (2005). "A review of video meteor detection and analysis software". *WGN, Journal of the International Meteor Organization*, **33:1**, 15–20.

Patat F., Moehler S., O´Brien K., Pompei E., Bensby T., Carraro G., de Ugarte Postigo A., Fox A., Gavignaud I., James G., Korhonen H., Ledoux C., Randall S., Sana H., Smoker J., Stefl S., and Szeifert T. (2011). "Optical atmospheric extinction over Cerro Paranal". *Astronomy & Astrophysics*, **527**, A91.

Patro S. G. K. and Sahu K. K. (2015). "Normalization: A preprocessing stage". *IARJSET*, **abs/1503.06462**.

Rudawska R., Zender J., Koschny D., Smit H., Löhle S., Zander F., Eberhart M., Meindl A., and Uriarte Latorre I. (2020). ""a spectroscopy pipeline for the canary island long baseline observatory meteor detection system"". *Planetary and Space Science*, **180**, 104773.

Zender J., Koschny D., and Ravensberg K. (2014). "Calibration of spectral video observations in the visual: theoretical overview of the ViDAS calibration pipeline". In Gyssens M., Roggemans P., and Zoladek P., editors, *Proceedings of the International Meteor Conference, Poznan, Poland, 22-25 August 2013*. pages 126–129.

Handling Editor: Javor Kac
This paper has been typeset from a LaTeX file prepared by the authors.

What just happened? Facilitating Cooperation Between Fireball Networks

Jim Rowe[1]

The UK has six fireball or meteor networks using five different camera systems. Similar overlaps occur in Germany[a], France[b], Morocco[c], and the United States[d]. We report here on two innovations which help overlapping or neighbouring networks compare observations and exchange data. These are:

1. The Global Fireball Exchange format. This is how a meteor network can represent a detailed single-station observation of a fireball event. This enables each network to swap observations with its neighbours, so that each can run their own trajectory and dark flight models using a mix of their own data and data from other networks.

This solution arose from detailed work presented to Europlanet Science Congress in 2020, in which eight existing single-station fireball data formats were compared and evaluated, and the format used by the Australian Desert Fireball Network was found to be the most useful for this purpose[e]. The Global Fireball Exchange (GFE) Format has been (or is being) implemented by five different networks. It was used to exchange data during the early stages of response to the Winchcombe meteorite fall.

2. The Event Log format. This is how a meteor network can disclose the timing and approximate observing location of each meteor that it has detected, to enable the other network to check for matching meteor observations. Unlike the Global Fireball Exchange format, which allows exchange of details of the observation after careful analysis, the Event Log Format just allows immediate confirmation that a fireball was seen by a particular camera at a particular time.

This solution arose from a 13-way email discussion[f] initiated by Luboš Neslušan[g] following the Europlanet Virtual Fireballs Conference in June 2021. After much discussion about existing meteor databases and communication protocols, Mike Hankey of the American Meteor Society (AMS) proposed an elegant, peer to peer solution that is easy to implement. This solution is described in this paper.

These tools allow neighbouring networks to quickly determine whether they both captured the same event of interest, then to exchange detailed observations of that event. This should lead to quicker recovery of meteorites and better initial strewn field calculations.

Received 2021 November 4

This work has been presented at the International Meteor Conference 2021 (held online).

1 The Global Fireball Exchange format

The fall of a meteorite may be caught by several fireball networks. Sometimes each network will have only one or two observations, which is not enough to be sure of the trajectory. Sharing data between networks allows better initial trajectory solutions to be established. Using a standard format for sharing allows a rapid exchange of data, facilitating a rapid recovery of the meteorite.

The Global Fireball Exchange (GFE) format was devised in 2020 and now has been implemented by several networks. Amateur astronomers may also know it as the ".ecsv" format, which is how it is described by participants in the Global Meteor Network[h]. This section describes its origin, use, maintenance, and implementation.

1.1 GFE and the Winchcombe meteorite

Use of the GFE format allowed sharing of data from three of five camera systems that caught the fall of the Winchcombe meteoroid/meteorite (see Figure 1), resulting in quick revision of the trajectory calculations

[1]Organiser, the UK Fireball Alliance.
Email: jim.rowe@scamp.org.uk

IMO bibcode WGN-496-rowe-cooperation
NASA-ADS bibcode 2021JIMO...49..211R

[a]In Germany, there is overlap between the FRIPON network (i.e., the Fireball Recovery and InterPlanetary Observation Network) and the AllSky7 network.

[b]In France, the FRIPON network overlaps with the BOAM (Base des Observateurs Amateurs de Météores) network and with the AllSky7 network.

[c]In Morocco, FRIPON has cameras in some coastal locations while Desert Fireball Network has cameras in inland dark-sky locations.

[d]In the US there are overlaps between the AllSkyCams (AMS) network, NASA's All Sky Fireball Network and the CAMS (Cameras for All-Sky Meteor Surveillance) network.

[e]The Europlanet Science Congress 2020 talk was called "Using incompatible fireball camera systems to find meteorites – towards a data exchange standard" and can be accessed at https://vimeo.com/458077336. The corresponding paper is unpublished but can be accessed in draft form at https://github.com/UKFAll/standard.

[f]The e-mail discussion was initiated by Luboš Neslušan on 21 June 2021 and involved Detlef Koschny, Damir Šegon, Denis Vida, François Colas, Jiří Borovička, Mike Hankey, Paul Roggemans, Sirko Molau, Vincent Perlerin, Gerhard Drolshagen, Regina Rudawska and Jim Rowe.

[g]Luboš Neslušan is Senior Researcher - Astronomer, Astronomical Institute, Slovak Academy of Sciences.

[h]The Global Meteor Network is based in Canada, and its homepage is https://globalmeteornetwork.org/.

Figure 1 – The Winchcombe meteoroid/meteorite arriving at 21:54 UTC on 28th February 2021. It was captured on five incompatible meteor or fireball camera systems.

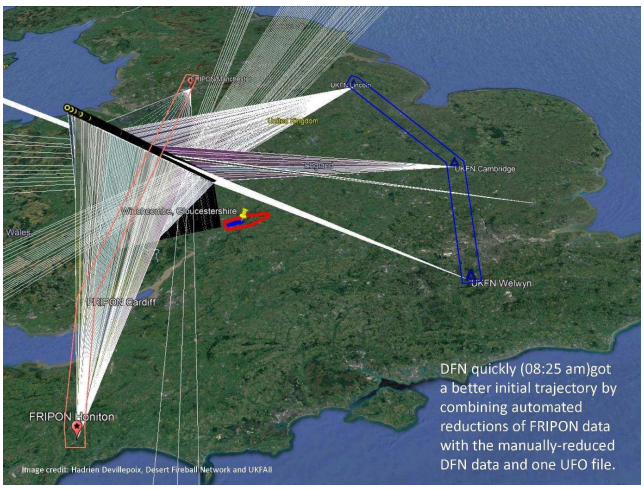

Figure 3 – The trajectory of the Winchcombe object, using data from three UKFN/DFN cameras, three SCAMP/FRIPON cameras and one UFOCapture system in the Nemetode network. Credit – Hadrien Devillepoix, Curtin University and DFN.

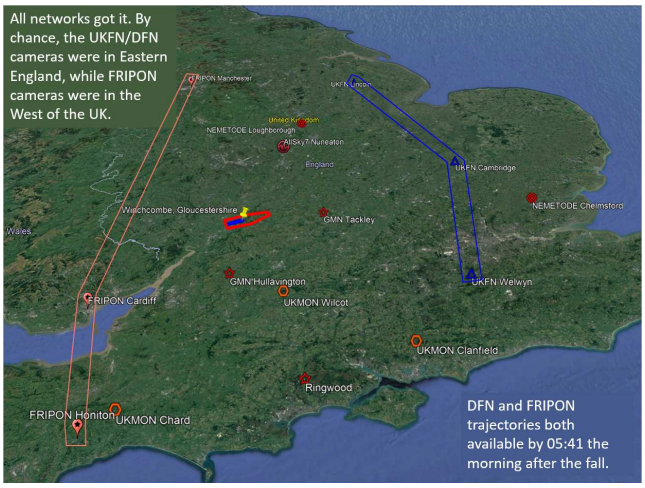

Figure 2 – Fifteen UK-based meteor or fireball cameras recorded the Winchcombe fall. This included three FRIPON[i] cameras (pink outline at left) and three DFN (Desert Fireball Network) cameras (blue outline at right). The main mass was found where the yellow pin is shown, while the small blue shape near the main mass shows the final strewn field, and the red shape surrounding the main mass is the "alert" area issued to the press the morning after the fall.

and so allowing a validated fall zone to be issued in a press release early on the morning after the fall.

Two of the six UK networks (i.e., SCAMP[j]/FRIPON and UK Fireball Network[k]/DFN) produced trajectory calculations nearly immediately. These were both available by 05:41 the morning after the fall, but the two trajectories were slightly different. This is because the three SCAMP/FRIPON cameras (shown in Figure 2) were under or behind the fall, while the three UKFN cameras (also shown in Figure 2) were in front of the fall and had a slightly foreshortened view.

UKFAll[l] immediately sent the data from each network to the other networks in GFE format. By 08:25, DFN had calculated a combined trajectory incorporating the DFN data, the FRIPON data and one observation from Nick James of the Nemetode[m] network in Chelmsford. This combined trajectory is shown in Figure 3. The corresponding orbit now looked like that of a main belt asteroid rather than that of a comet.

1.2 Parallel processing, resilience, and speed

The traditional way of calculating a trajectory from multiple camera systems is for one expert to collate all of the original image data from the various systems (or from dashcams or security camera footage) and to analyse each different image system consistently and accurately. This capability is not widespread, and if that expert is on holiday, away, busy or disinclined then no progress can be made.

There is nothing wrong with this, and the best results may indeed be obtained by patient and consistent plate solving on the image and picking out of the trajectory against the background. However, results obtained this way may not be available for days or weeks after the fall.

By contrast, the sharing of single-station observations in a standard format allows the experts in each system to reduce the data from their own system, then contribute it in a standard format for analysis and validation by the operators of other systems. Outliers will

[i]FRIPON is the Fireball Recovery and InterPlanetary Observation Network, a network of all-sky fireball detection cameras based mainly in France. Its homepage is at `https://www.fripon.org/`.

[j]SCAMP is the System for Capture of Asteroid and Meteoroid Paths and is the UK component of the FRIPON network.

[k]The UK Fireball Network (UKFN) is the UK part of the Global Fireball Observatory and deploys equipment developed by and for the Desert Fireball Network in Australia. UKFN is run mainly from Imperial College London and the University of Glasgow, while the Desert Fireball Network is a collaboration focussed on Curtin University in Western Australia.

[l]UKFAll is the UK Fireball Alliance, `https://www.ukfall.org.uk/`.

[m]Nemetode is the Network for Meteor Triangulation and Orbit Determination, `http://www.nemetode.org/`.

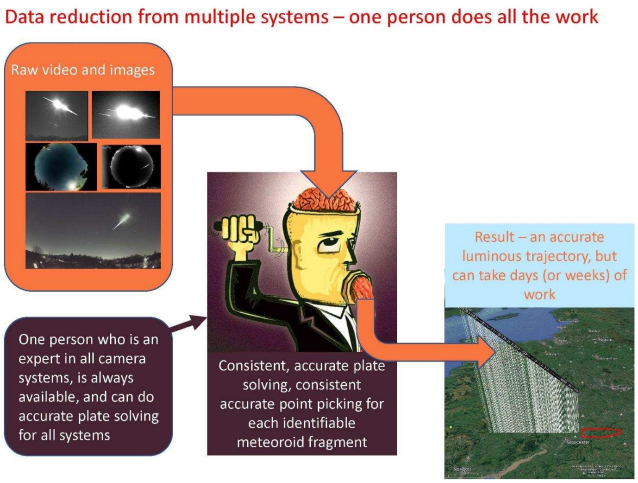

Figure 4 – A schematic illustration of one person processing original image data from multiple sources.

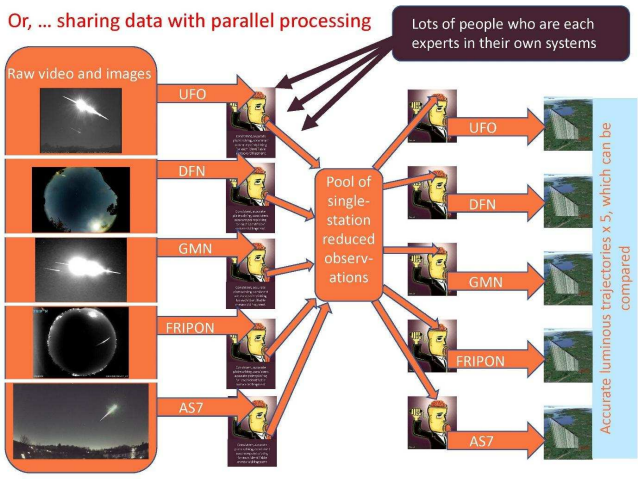

Figure 5 – Each system will always have one or more expert users who can extract good-quality data from the system that they are very familiar with. This data can then be pooled in GFE format, allowing parallel processing of data from multiple sources using system-specific expertise and reducing reliance upon any one individual.

usually become apparent quickly and can be re-analysed or can be excluded from the data pool. Individual specialisms (such as analysis of dashcam videos) can make their contribution. This is shown schematically in Figure 5.

An additional benefit of "pooled" data is that each network can perform trajectory and strewn field calculations on the data set, and mistakes at this second stage of the analysis can be identified rapidly. If several strewn field calculations which use the same luminous path information then produce dissimilar results, this can be investigated and resolved. It is far better to find a mistake before you go hunting for a meteorite, rather than after a week of looking in the wrong place!

1.3 Implementation of GFE

The GFE format was designed in order to solve a problem of data sharing within UKFAll in the UK, and so unsurprisingly its initial adoption has been mainly by networks operating in the UK. The following diagram

Global Fireball Exchange format - Implementation update

Network	Can read GFE?	Can write GFE?	Status
Desert Fireball Network	Yes	Compatible but not yet identical	Will be fully implemented as native format by y/e 2021
Global Meteor Network	Yes	Yes	Done. The "ECSV" file is now the GMN fireball format
FRIPON	Not yet	Not yet	Will implement (TBC). Jupyter converter used now
AllSkyCams	Yes	Planned	Implementation planned before the end of 2021
MetRec	N/A	Yes	Writing competed. MetRec does not read fireball data.
UFO	No	No	Not yet approached. Jupyter converter used
CAMS	No	No	Will implement if standard structure with read and write "C" functions provided
NASA, Czech, Polish, Finnish, Spanish networks			Not yet approached

Figure 6 – Implementation status as of September 2021. Please note that AllSkyCams and AllSky7 are the same system; MetRec (the Meteor Recognizer) is a central European system with a very long heritage, UFO refers to UFOCapture and UFOAnalyzer produced by SonotaCo and Cams is the Cameras for All-Sky Surveillance system. Note – In December 2021, SonotaCo decided to add GFE write-only functionality to UFOAnalyzer.

(Figure 6) was presented to GMC 2021 to summarise implementation.

1.4 Origins and formalisation of GFE

During 2020 there was a widespread consultation between networks and other interested parties to determine whether a standard format for exchange of single-station data was useful, and if so, what format should be used. Eight existing formats were examined, of which four were found to be suitable. Of those four, the best was found to be that used by the Desert Fireball Network, which was an Extended CSV format (i.e., "ecsv") native to AstroPy but which could also be edited with a text editor or spreadsheet program. The GFE format is therefore based very closely upon the Desert Fireball format. Details of this analysis can be found in the 2020 Europlanet Science Congress paper (Rowe et al., 2020) and presentation referenced in footnote [e].

In January 2021, Jim Rowe, Denis Vida and Hadrien Devillepoix formally defined the standard, and made it available to all for implementation.

An example of the GFE format is shown in the diagram in Figure 9. Further examples can be found online here: `https://github.com/UKFAll/standard`.

The GFE standard, sample data and read/write routines are available to everyone on Github, as described in Figure 10.

The standard is maintained by a committee, made up of UKFAll and a representative of each fireball network that has implemented the GFE standard. At the moment, the committee is made up of Jim Rowe of UKFAll, Denis Vida of the Global Meteor Network, Hadrien Devillepoix of DFN and Sirko Molau of MetRec and AllSky7. The standard is therefore owned and controlled by the networks that have implemented it. New networks are invited to join the committee once they implement the GFE standard.

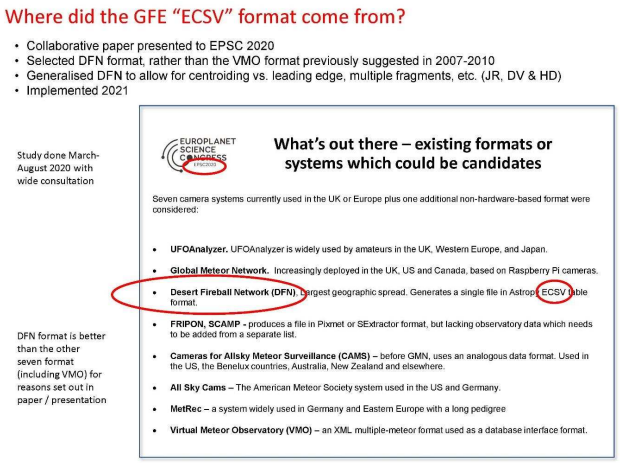

Figure 7 – The eight existing formats evaluated in the 2020 EPSC (Europlanet Science Congress) paper.

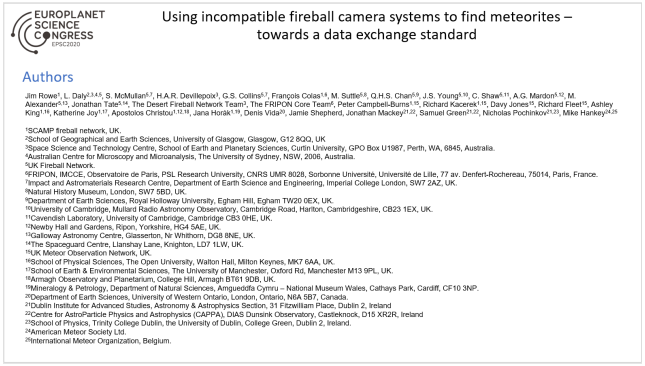

Figure 8 – The author list for the 2020 EPSC paper gives a good guide to the extent of the consultation that occurred between March and August 2020.

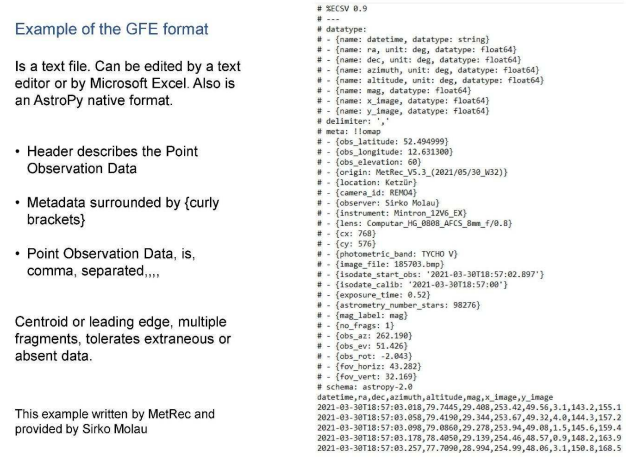

Figure 9 – An example of the GFE format. The first 13 lines are headers, then there is a list of metadata which describes the camera location and orientation. Finally, there is a comma-separated table of data relating to each observed point in the meteor path. In the example above, only five points were observed.

The process for proposing and/or approving any changes to the GFE standard is very conservative, to avoid making changes that render old data unusable. This change process is set out in the standard.

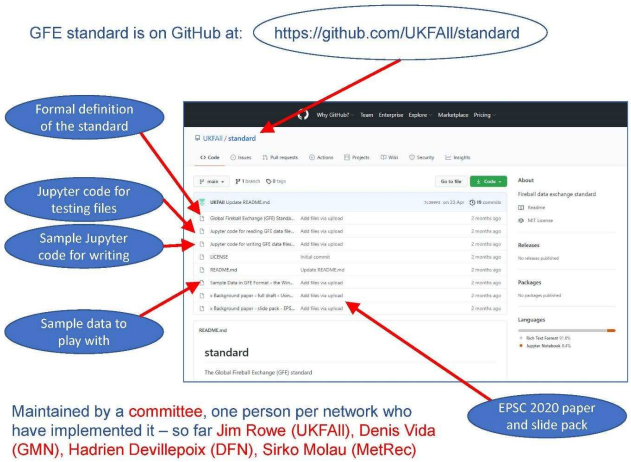

Figure 10 – The documents available at `https://github.com/UKFAll/standard`. Since then, a data converter (written as a Jupyter script) and a user guide for the script have been added and are freely available.

2 The Event Log format

Exchanging data between networks is not usually automated, because each network has a substantial investment in equipment and infrastructure, and so it is not sensible to automatically make all data immediately available to anyone who wants them.

However, most networks are happy to confirm whether or not they saw a particular event. That confirmation can then lead to a more detailed discussion about sharing data relating to that event.

2.1 Origin of the Event Log Format

Following the May 2021 Europlanet fireballs conference, an e-mail discussion about event sharing and event, trajectory and orbit databases was initiated by Luboš Neslušan of the Astronomical Institute of the Slovak Academy of Sciences. Initially the discussion focussed on whether multiple networks could or should report events and related data to a central server, and which server that should be. Multiple possibilities were discussed with the consensus being that it would not be possible to implement the type of solution illustrated Figure 11.

The discussion then turned to peer-to-peer solutions, and Mike Hankey of the AMS proposed an elegant and simple solution that was compatible with the computer security issues faced by institutions and involved minimal computing overhead and efficient use of communications infrastructure.

Shown schematically in Figure 12, the peer-to-peer system allowed multiple databases to query each network for events, and for the networks to query each other.

As shown in Figure 13, each network would host two text files on its public-facing server. These two files are:

The "Camera Location File", which just lists the approximate location of each camera on the network and so is very rarely updated. The "Event Log" file, which is updated every time the network makes a detection

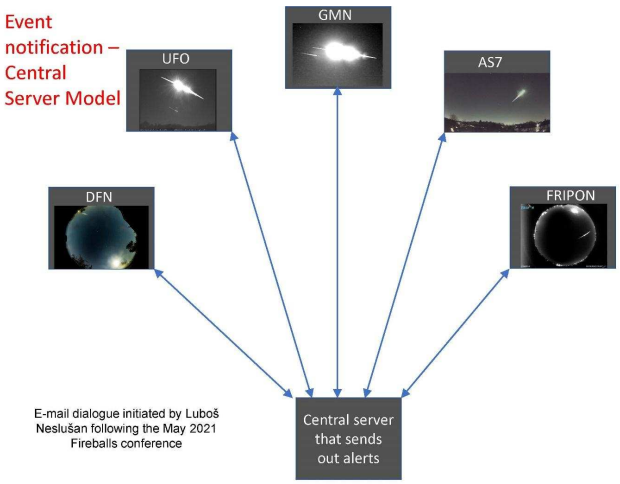

Figure 11 – A schematic representation of a server-based solution. A central database talks to each network, collates observation, then sends out alerts when a match is found between data from the various network. There was no agreement on which central server was the best to use and concerns were expressed on implementation cost, network security and the volume of data exchange required.

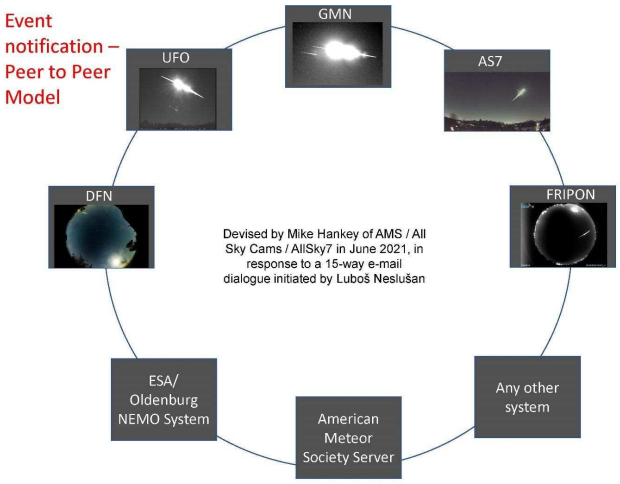

Figure 12 – A schematic representation of a peer-to-peer solution. Each meteor network or database that records a fireball event can then query neighbouring networks to determine whether there is a matching event in the neighbouring network.

and records the exact time of each detection by each camera over the previous 72 hours.

Taken together, these files allow a third-party network to check whether this network saw an event within a particular time period, and if it did, to look up the location of the camera to help determine whether that observation could be relevant or useful.

Again, this format is available for anyone to read and can be found on GitHub at `https://github.com/UKFAll/event_log`, along with examples, as shown in Figure 14.

2.2 Implementation of the Event Log Format

Unlike the Global Fireball Exchange format, the Event Log format has not yet been widely implemented. It was implemented by the UK Meteor Network in July 2021 but, in the absence of implementation by any other network, has not been maintained.

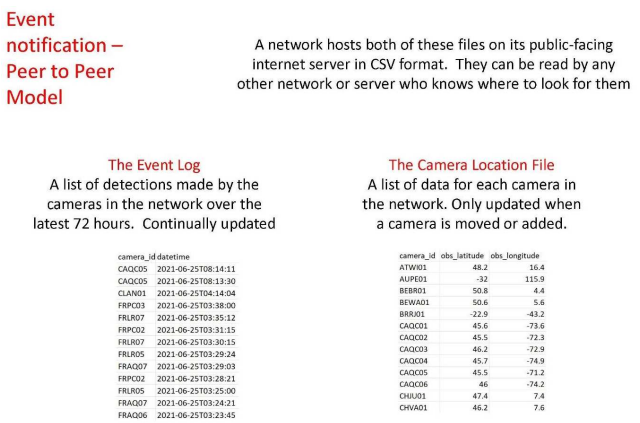

Figure 13 – Examples of the Camera Location File and the Event Log file. These examples correspond to the FRIPON network, which is an all-sky network. For a network of narrow-field cameras (such as the Global Meteor Network or CAMS), the Camera Location File can also contain information describing the field of view of each camera.

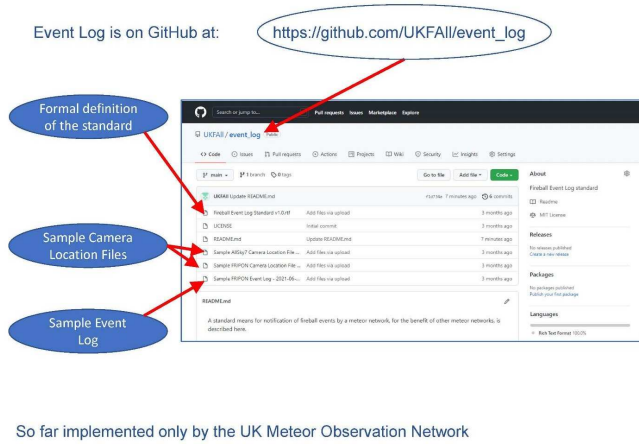

Figure 14 – A formal definition of the Event Log format is available at `https://github.com/UKFAll/event_log`. This includes examples from the FRIPON and AllSky7 networks.

3 Summary

This paper has described two forms of data interchange between networks, both designed to answer the question "what just happened?". The "Event Log" format immediately records that an event has been seen by a particular camera within a particular network, while the Global Fireball Exchange format allows exchange of detailed single-station fireball observations once reliable data is available.

The Global Fireball Exchange format (GFE format or ECSV format) was devised in 2020 based on the single-station data format used by the Desert Fireball Network, and in 2021 has been implemented (or is being implemented) by several fireball networks. It is a formally-defined standard with a committee structure maintaining and supporting it.

The Event Log format is also formally defined, but as yet has not been widely adopted and has no such underlying committee or support structure.

Together, these two standards (particularly the GFE standard) can facilitate more reliable early recovery of meteorites that have been seen by more than one fireball network by facilitating rapid validation of trajectory and strewn field calculations.

References

Rowe J., Daly L., McMullan S., Devillepoix H., Collins G., Suttle M., Chan Q., Young J., Shaw C., Mardon A., and others (2020). "Using incompatible fireball camera systems to find meteorites - towards a data exchange standard". In *European Planetary Science Congress*. pages EPSC2020–856.

Handling Editors: Theresa Ott and Javor Kac

The International Meteor Organization

www.imo.net

Follow us on Facebook InternationalMeteorOrganization

Follow us on Twitter @IMOMeteors

Council

President: Cis Verbeeck,
Bogaertsheide 5, 2560 Kessel, Belgium.
e-mail: cis.verbeeck@scarlet.be

Vice-President: Juraj Tóth,
Fac. Math., Phys. & Inf., Comenius Univ.,
Mlynska dolina, 84248 Bratislava, Slovakia.
e-mail: toth@fmph.uniba.sk

Secretary-General: Robert Lunsford,
14884 Quail Valley Way, El Cajon,
CA 92021-2227, USA. tel. +1 619 755 7791
e-mail: lunro.imo.usa@cox.net

Treasurer: Marc Gyssens, Heerbaan 74,
B-2530 Boechout, Belgium.
e-mail: marc.gyssens@uhasselt.be
BIC: GEBABEBB
IBAN: BE30 0014 7327 5911
Bank transfer costs are always at your expense.

Other Council members:
Javor Kac (see details under WGN)
Detlef Koschny, Zeestraat 46,
NL-2211 XH Noordwijkerhout, Netherlands.
e-mail: detlef.koschny@esa.int
Sirko Molau, Abenstalstraße 13b, D-84072
Seysdorf, Germany. e-mail: sirko@molau.de
Francisco Ocaña Gonzalez, C/ Arquitectura, 7.
28005 Madrid, Spain.
e-mail: francisco.ocana.gonzalez@gmail.com
Vincent Perlerin, 16, rue Georges Bernanos,
51100 Reims, France.
e-mail: vperlerin@gmail.com
Jürgen Rendtel, Eschenweg 16, D-14476
Marquardt, Germany. e-mail: jrendtel@aip.de

Commission Directors

Visual Commission: Jürgen Rendtel
Generic e-mail address: visual@imo.net
Electronic visual report form:
http://www.imo.net/visual/report/electronic
Video Commission: Sirko Molau (video@imo.net)
Photographic Commission: Bill Ward
(bill_meteor@yahoo.com)
Generic e-mail address: photo@imo.net
Radio Commission: Chris Steyaert
(radio@imo.net)
Fireballs: Online fireball reports:
http://fireballs.imo.net

Webmaster

Karl Antier, e-mail: webmaster@imo.net

WGN

Editor-in-chief: Javor Kac
Na Ajdov hrib 24, SI-2310 Slovenska Bistrica,
Slovenia. e-mail: wgn@imo.net;
include METEOR in the e-mail subject line

Editorial board: Ž. Andreić, M. Argo, D.J. Asher,
F. Bettonvil, J. Correira, M. Gyssens,
C. Hergenrother, T. Heywood, J.-L. Rault,
J. Rendtel, C. Verbeeck, S. de Vet, D. Vida.

IMO Sales

Available from the Treasurer or the Electronic Shop on the IMO Website	€	$
IMO membership, including subscription to WGN Vol. 49 (2021)		
Surface mail	26	32
Air Mail (outside Europe only)	49	60
Electronic subscription only	21	25
Proceedings of the International Meteor Conference on paper		
1990, 1991, 1993, 1995, 1996, 1999, 2000, 2002, 2003, per year	9	12
2007, 2010, 2011, per year	15	20
2012, 2013, 2014, 2015 per year	25	34
Proceedings of the Meteor Orbit Determination Workshop 2006	15	20
Radio Meteor School Proceedings 2005	15	20
Handbook for Meteor Observers	15	20
Meteor Shower Workbook	12	16
Electronic media		
Meteor Beliefs Project ZIP archive	6	8

C/2021 A1 (Leonard), Messier 3 and a meteor

In this image taken on the early morning of 2021 December 3, 4:31 AM MT, at Grand Mesa Observatory, Comet C/2021 A1 (Leonard) is seen moving past Globular Cluster M3 in our night sky when a meteor streaked across this scene. Single 120 second combined with 40% mix for noise reduction from a 90×120 second stack. Camera: QHY367 Pro C Full Frame One Shot Color CMOS. Optics: Takahashi E-180 Astrograph. Captured and processed by Tom Masterson and Terry Hancock.